Turbulence-Induced Vibrations Prediction

Through Use of an Anisotropic Pressure Fluctuation Model

Nout van den Bos

TU Delft

Turbulence-Induced Vibrations Prediction

Through Use of an Anisotropic Pressure Fluctuation Model

by

Nout van den Bos

to obtain the degree of Master of Science
at the Delft University of Technology,
to be defended publicly on Monday April 25, 2022 at 14:00 PM.

Student number:	4551206	
Project duration:	August 9, 2021 – April 25, 2022	
Thesis committee:	Dr.ir. M.I. Gerritsma,	TU Delft, chair
	Dr.ir. M.J.B.M. Pourquie,	TU Delft, examiner
	ir. K. Zwijsen,	NRG, supervisor
	Dr. ir. A.H. Van Zuijlen,	TU Delft, supervisor

This thesis is confidential and cannot be made public until April 25, 2024.

TU Delft NRG

Preface

This thesis started roughly one year ago, but the inspiration came long before that. During the summer of 2020, I found an ad for a thesis opportunity at NRG. This broadened my horizon to fields outside of aerospace that rely on fluid dynamics, which often have very different challenges. I was immediately excited and this sparked my interest to write a thesis about a topic in this different but adjacent world of fluid dynamics. The safety and reliability of nuclear reactors starts at the understanding and the ability to be able to model all the complex phenomena that occur in a reactor. With my thesis, I hope to have contributed towards this. This work could not have been completed without the support I received during my thesis, and I would like to express my thanks to all the people that have been involved.

I want to start by thanking my supervisors Alexander van Zuijlen and Kevin Zwijsen. Thank you, Sander, for your calm and supportive stance, and your clear and helpful insights that you shared during our meetings. These insights have often pushed me in the right direction to find the root cause of a problem. My sincere thanks to Kevin, for all the relaxed, open, and fruitful discussions we had, and the support you lend me. I also wish to show my appreciation for Nuclear Research & Consultancy Group for the opportunity to work on such an interesting topic, and for supporting me with the necessary tools and environment for the thesis. It has been a pleasure.

My sincere thanks also goes out to all my colleagues at NRG. But in particular, thank you Ferry, Edo, Daniele, Muaaz & Sina, for all your support. I greatly appreciated your help with FSI, preCICE and OpenFOAM related problems, as well as helping me find bugs in my code, and lastly by asking the right questions that I did not think of myself.

Finishing the thesis certainly has not been easy, but I could always rely on the support of my friends. Thank you for the necessary distractions outside of my thesis, and for being a part of my university experience. I would also like to thank my family for their continuous support during my studies, and for always encouraging me to pursue my education. Finally, I would like to give thanks to my girlfriend. Your motivation and ambitions are contagious, and they make me want to push myself to grow as a person. Your support is indescribable, and so is the happiness that you give me. I thank you all, sincerely.

Nout van den Bos
Alkmaar, April 2022

Abstract

In nuclear engineering, safety is always considered as the highest priority. Due to the complicated design of nuclear reactors, many complex phenomena can cause points of failure. In the case of nuclear fuel rods, the axial flow that cools the rods can induce a vibration due to the turbulent nature of the flow. The turbulence-induced vibrations create small but significant vibration amplitudes, which in turn can cause structural effects such as fatigue problems, fretting wear, and stress corrosion cracking. For this reason, turbulence-induced vibrations have been the subject of many studies. While earlier studies have focussed on analytical models, it became clear that effort must be put in for the development of computational methods, so called Fluid-Structure Interaction (FSI) simulations.

While DNS and LES can predict pressure fluctuations, these simulations are typically too expensive for industrial applications in FSI. Instead, a URANS approach coupled with a pressure fluctuation model can be used, to reduce the computational cost. This approach has been used previously, and showed promising initial results, but it generally showed an underestimation of the vibration amplitude. For this reason, a new pressure fluctuation model, called AniPFM (Anisotropic Pressure Fluctuation Model), was developed in the thesis. First, it models velocity fluctuations, which was based on existing methods. In turn, these velocity fluctuations are used to solve for the pressure fluctuations.

The AniPFM aims to improve the prediction of the pressure fluctuations in several ways. Most notably, whereas previous iterations could only represent the turbulence as isotropic, in the current model anisotropic Reynolds stresses can be reconstructed. Furthermore, only the resolved scales are represented by the velocity fluctuations. Finally, several time correlation methods based on the transport of turbulence have been introduced, next to several other smaller improvements.

The AniPFM has been tested out on several testcases, namely two purely CFD test cases, and one FSI case. From simulating decaying homogeneous isotropic turbulence, it was found that the modelling of the temporal decay of the turbulence was vastly improved. Furthermore, it showed excellent agreement with both experimental and DNS data in terms of the pressure-wavenumber spectrum, and the root-mean-squared pressure fluctuations. From turbulent channel flow simulations, it was found that for anisotropic turbulence, the pressure fluctuations are overestimated, but still within a respectable range of 9% compared to DNS data. Finally, the fluid-structure interaction of a brass beam in turbulent water is simulated, which showed the ability of the AniPFM to predict turbulence-induced vibrations. The AniPFM showed errors w.r.t. the replicated experiment that were in the similar range as LES calculations, while using less computational resources. The AniPFM simulations gave an error range of 15-60% w.r.t. experimental data over the full range of simulated flow velocities, whereas a previously used pressure fluctuation model underestimated the RMS amplitude by a factor of six. While further improvements can certainly be made to the AniPFM, it has already showcased its potential for lower cost simulations of turbulence-induced vibrations in nuclear applications.

Contents

List of Figures

List of Acronyms

ALE Arbitrary Lagrangian-Eulerian.

AniPFM Anisotropic Pressure Fluctuation Model.

BWR Boiling Water Reactor.

C&EC Convection & Exponential Correlation.

CAA Computational Aero-Acoustics.

CFD Computational Fluid Dynamics.

CSM Computational Structural Mechanics.

DNS Direct Numerical Simulation.

EARSM Explicit Algebraic Reynolds Stress Model.

FSI Fluid-Structure Interaction.

HIT Homogeneous Isotropic Turbulence.

IQN-ILS Interface Quasi Newton Inverse Least Squares.

LES Large Eddy Simulation.

MOR Mechanical Reduced Order Model.

NRG Nuclear Research & Consultancy Group.

NS Navier-Stokes.

PDE Partial Differential Equation.

PFM Pressure Fluctuation Model.

PWR Pressurised Water Reactor.

RANS Reynolds-Averaged Navier-Stokes.

RC&EC Rescaled Convection & Exponential Correlation.

RSM Reynolds Stress Model.

RST Reynolds Stress Tensor.

SEM Synthetic Eddy Method.

ST Synthetic Turbulence.

TCF Turbulent Channel Flow.

TIV Turbulence Induced Vibrations.

URANS Unsteady Reynolds-Averaged Navier-Stokes.

1

Introduction

Nuclear energy has a short but very packed history, and it has become essential to generate the demand for energy of the modern world. It produces roughly 10% of the world's electricity, and nuclear energy is the second-largest generator of low-carbon energy [19]. While nuclear energy provides a large part of the world's clean energy, it is still often not perceived well by the general public. This is among others due to the nuclear waste that is produced by nuclear reactors, and its connotations with nuclear weapons. Next to this, preceding incidents regarding nuclear reactors, such as the incidents in Chernobyl and Fukushima, have given nuclear energy a bad name regarding safety.

Regardless of the public perception, studies have actually shown that the number of fatalities in nuclear energy is far less than for fossil fuels such as coal, oil and gas, and even fewer fatalities than green energy sources such as wind- and hydropower [20, 21]. However, it also showed that incidents are much more expensive for nuclear energy compared to other energy sources. Safety is inherent in the culture surrounding nuclear reactor operators, and there is a lot of research done by corporations, research institutes, and universities in order to further increase the safety of nuclear reactors.

A particularly important topic in the field of nuclear safety is fuel rods. Fuel rods are submerged in a coolant liquid, such as water or liquid metal. For maximal efficiency, the coolant liquid typically flows axially over the fuel rods. While the axial flow leads to efficient cooling of the fuel rods, it can also cause Turbulence-Induced Vibrations (TIV), causing the fuel rods to vibrate. This phenomenon plays a critical role in terms of nuclear safety, as it can cause structural effects such as fatigue problems, fretting wear, and stress corrosion cracking [22, 23].

The phenomenon has been studied since nuclear reactors started being developed in the 1950s, and it has been the root of several incidents [22, 24]. In the previous century, an emphasis was put on experiments in this field, as well as using semi-empirical relations to establish a relation between the amplitude of vibration and relevant flow parameters, such as the flow velocity and the density of the fluid, as well as structural parameters such as the diameter of the fuel rod, the natural frequency, and the damping ratio of the fuel rod [25–29]. From these studies, results showed quite large differences between theory and experiments, the semi-empirical relations gave a maximal order of accuracy of one order of magnitude. Furthermore, the studies were often limited to only one fuel rod, which gives uncertainty regarding extending the semi-empirical methods to bundles with multiple fuel rods.

More recently, due to the larger availability of computational resources, the use of Fluid-Structure Interaction (FSI) simulations applied to fuel rods has received more interest. Liu et al. [30–32] consider a simplified approach where the forces of the fluid on a fuel rod are computed by using Large Eddy Simulation (LES), and the fuel rods are approximated using one-dimensional beam models. Another approach was to simulate the fluid using LES while considering the rod as rigid, and then to apply the forces of the fluid on the rod in a subsequent Computational Structural Mechanics (CSM) code [33, 34].

While LES and Direct Numerical Simulations (DNS) are much more accurate than URANS simulations, these simulations are also much more costly, and it is currently not realistic for corporations to use these type of simulations for complex FSI simulations. This is why it is important to investigate the abilities of URANS in the application for FSI simulations of TIV on fuel rods. De Ridder et al. [16, 35] showed that the modal response of a fuel rod can be accurately calculated using URANS simulations. This was confirmed in further

studies, and extended to a bundle of multiple fuel rods [4]. While URANS simulations can accurately predict the modal response for the case of TIV on fuel rods, the amplitude of the vibrations is severely underpredicted. This is because URANS only calculates the ensemble average forces on the fuel rod, and it does not calculate the forces on the fuel rod due to instantaneous turbulent pressure fluctuations.

To remedy this, a Pressure Fluctuation Model (PFM) was proposed by Kottapalli [14], and it was incorporated into the numerical framework NRG-FSIFOAM, which is a framework for FSI simulations based on open-source solvers [4]. In this framework, the PFM is used to simulate the pressure fluctuations based on URANS data, these fluctuations are then together with the ensemble-average pressure imposed on the fuel rod as an external excitation for the CSM solver. This method was further investigated and from comparison to experimental data it was found that the current PFM shows amplitudes in the same order of magnitude, but it did not give the required accuracy yet [14, 36]. The goal of the current thesis is to develop an improved pressure fluctuation model, in order to increase the accuracy in the prediction of vibration amplitude through FSI-simulations for nuclear fuel rods subjected to axial flow. In order to run FSI-simulations, many different parts need to work together, and they need to exchange various types of data. In fig. 1.1, an overview is given of the interaction between the various solvers.

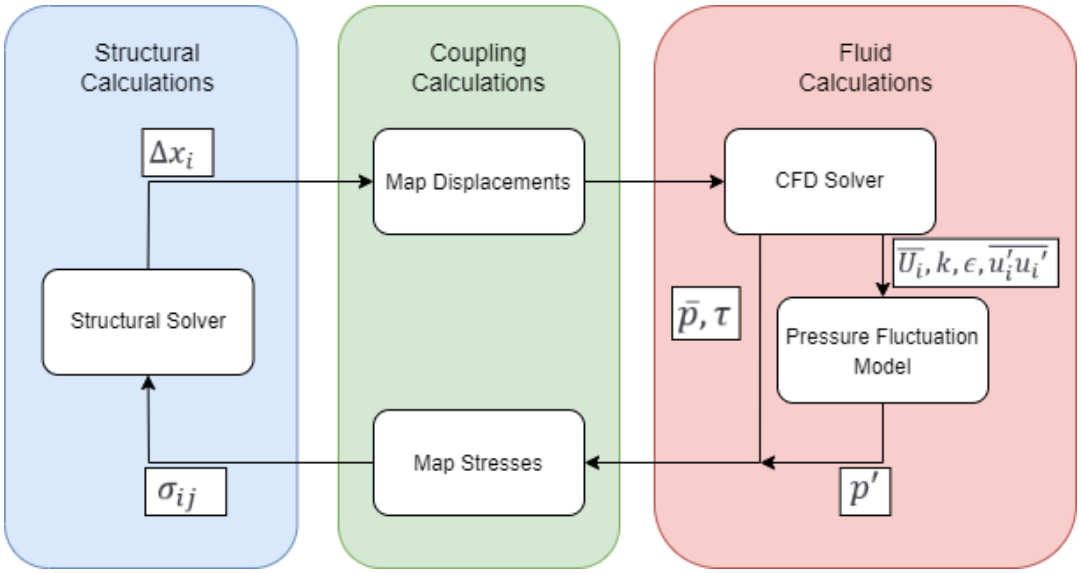

Figure 1.1: A flow-chart of the global interactions between the several numerical solvers.

In the coming sections of this chapter, first, an introduction to the workings of a nuclear reactor is given, then several types of fluid-induced vibrations are discussed. After this, the research objectives of this thesis are given, and finally, an overview of the thesis is given.

1.1. Nuclear Reactor

As the thesis will be centered around the application of a pressure fluctuation model to nuclear fuel rods, a review on the workings of nuclear reactors is called for. There are different generations of nuclear reactors, but the focus is put on generation three reactors, as these reactors are currently in commercial use. This generation of reactors can be divided into different categories, based on the method that is used for cooling. The current types are Fast Breeder Reactors, Pressurized Heavy Water Reactors, Gas Cooled Reactors, Boiling Water Reactors (BWR), and finally Pressurized Water Reactors (PWR). The latter is the most commonly used reactor. A sketch of this type of reactor is given in fig. 1.2, however, the containment structure varies for the different categories of reactors.

The fuel rods are shown in the reactor pressure vessel in fig. 1.2. In fig. 1.3, a more detailed sketch with the components of the reactor pressure vessel is shown. In the fuel rods that are part of the fuel assembly as shown in fig. 1.3, pellets of uranium are stacked together, and fission takes place. The surrounding water acts both as a coolant and as a means to moderate the velocity of the neutrons, such that the chain reaction is sustained. The heat created by the fission is transferred from the rods to the coolant, which is transported to the steam generator. The steam generates electricity through a turbine, and it is condensed again to go

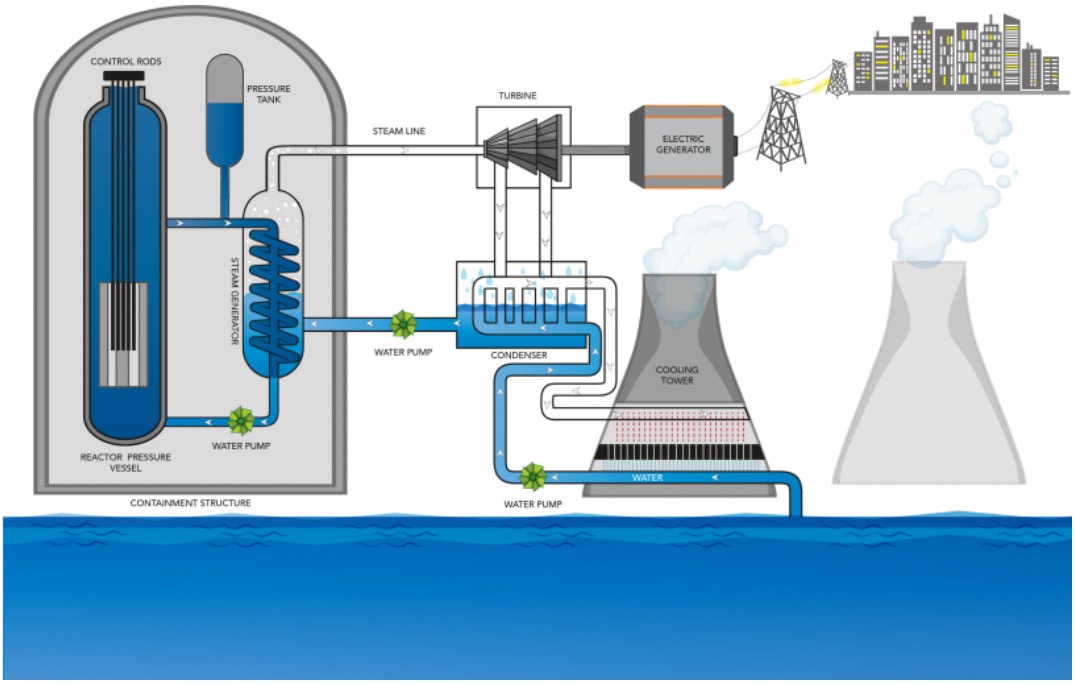

Figure 1.2: A sketch of the workings of a pressurized water reactor [1].

through the same loop. For the focus of the thesis, the reactor pressure vessel is of most interest, as the fuel rods are located here. Because they are submerged in a coolant, fluid-structure interaction phenomena can occur, which typically results in vibrations. Next to the fuel rods, excitation mechanisms are also found in the steam generator. A distinction can be made in the type of flows that characterize the different stages of a nuclear reactor. For steam generators, two-phase flow is typically considered. For the reactor pressure vessel, the flow can be fully single-phase as for PWRs, or also two-phase as for BWRs. As a new model for pressure fluctuations will be implemented during the thesis, only single-phase flows are considered, due to its more simplistic nature. Furthermore, only elements of the reactor pressure vessel or simplifications thereof are considered, such as the fuel rods. These elements are only considered in axial flow to limit the scope of the thesis.

1.2. Fluid Induced Vibrations

As mentioned in section 1.1, the coolant can induce vibrations to the fuel rods which are located in the reactor pressure vessel. The vibrations of the fuel rods typically have multiple causes, these excitation mechanisms have been classified such that they can be studied individually, and the underlying physical problem can be addressed. The different excitation mechanisms were classified and described by Pettigrew et al. [37], and they are shortly introduced below:

- *Fluid Elastic Instability:* These instabilities result from the absorption of energy of the structure from the fluid induced dynamic forces. When stable, the structure dissipates enough energy through damping, such that the dissipated energy is larger than the absorbed energy from the flow. For a high enough flow velocity, this damping dissipates not enough energy, and the coupling becomes unstable. This typically only happens in cross flow situations, and it is usually not a problem for components that are subjected to axial flow, such as fuel rods [37].
- *Periodic Vortex Shedding:* This phenomenon typically occurs when structures are subjected to cross flow, and it happens downstream closely to the structures. The periodic vortices in turn create periodic forces on the structure. Resonance can be induced if the vortex shedding frequency is near the eigenfrequency of the structure, causing large vibration amplitudes. This phenomenon typically happens at high-density fluid flows, due to the large induced periodic forces [37].
- *Acoustic Resonance:* This is closely related with periodic vortex shedding. It occurs when the vortex

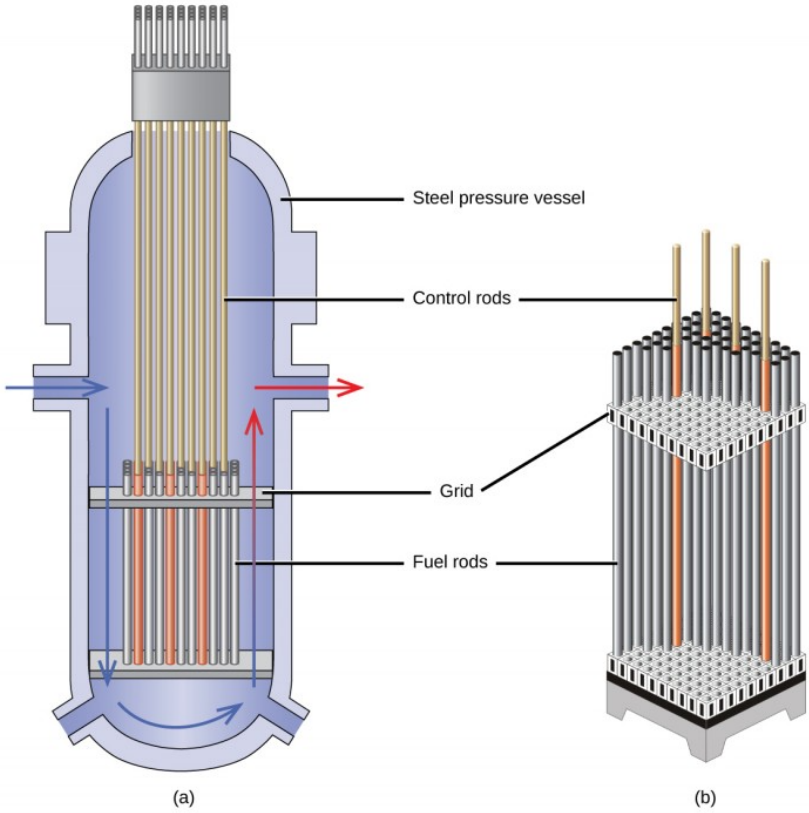

Figure 1.3: A more detailed sketch of the fuel rods in the reactor pressure vessel [2].

shedding frequency is equal to the natural frequency of acoustic cavities that are formed in tube bundle structures. Due to the acoustic resonance, intense noise is caused and this can give severe structural damage. It can also happen in axial flow, caused by periodic pressure pulsations from e.g. pumps, or by acoustic noise generated by other piping elements such as valves [37].

- *Turbulence-Induced Vibrations:* This phenomenon is the main excitation mechanism for structures subjected to axial flow. Turbulence can be introduced by upstream elements such as nozzles or elbows, or it can be introduced locally as it flows around the structure. The turbulence causes random pressure fluctuations on the surface of the structure, which forces the structure into vibration. It is also important for structures in cross-flow, as it can induce a large enough vibration to cause long-term fretting wear damage [37].

All the mentioned excitation mechanisms are still active research areas within nuclear engineering, and they are interesting to say the least. However, the objective of this thesis is to improve the pressure fluctuation model that is used to model turbulence-induced vibrations. Thus, TIV is the only considered excitation mechanism in this thesis. In particular, only nuclear fuel rods, similar elements, or simplifications thereof, subjected to single-phase axial flow are considered.

1.3. Research Objectives

As mentioned previously in the chapter introduction, the goal of the thesis is to develop an improved pressure fluctuation model, in order to increase the accuracy in the prediction of vibration amplitude through FSI-simulations for nuclear fuel rods subjected to axial flow. Here, this goal is separated into two main objectives, with a more detailed description:

To improve the current pressure fluctuation model, in particular the accuracy of the root-mean-squared pressure fluctuations and the pressure fluctuation wavenumber spectrum in

the near wall vicinity, by using more realistic assumptions regarding (an)isotropy, the energy spectrum and time correlation.

To improve the FSI modelling of nuclear fuel rods in axial flow using URANS, in particular the RMS amplitude and the amplitude frequency spectrum, by utilizing a more accurate pressure fluctuation model.

In order to achieve the first main objective, several sub-objectives must be met. These objectives are based on the desired capabilities of the new pressure fluctuation model, and achieving these sub-objectives results in an implemented pressure fluctuation model. These sub-objectives are shown below:

To implement a more accurate time correlation, by implementing an exponential relation and by modelling convection through the linearized momentum equation.

To model anisotropic energy spectra, by scaling and transforming an isotropic spectrum according to the Reynolds stress tensor.

To achieve the second main objective, several sub-goals must be achieved as well. In order to improve the FSI modelling, it is necessary to implement and validate FSI simulations. Furthermore, the appropriate URANS model must be selected that can accurately represent the near-wall flow around fuel rods. By achieving the following sub-goals, the second main objective can be achieved:

To evaluate the effect of the resolved Reynolds stress tensor on the pressure fluctuations, by using several URANS turbulence models on a simplified geometry.

To model the fluid-structure interaction physics of a fuel rod in axial flow, by using the NRG-FSIFOAM framework and a pressure fluctuation model.

To validate the results of FSI simulations of a fuel rod in axial flow, by comparing it to experimental data with the same set-up.

1.4. Overview of the Report

In this chapter, the motivation for the thesis topic was given, as well as an overview of the workings of nuclear reactors. In chapter 2, the theory of fluid-structure interaction is discussed, namely the governing physics for both domains and the interface, as well as the implementation of NRG-FSIFOAM and its verification. In chapter 3, an overview is given of available Computational Fluid Dynamics (CFD) methods and turbulence characteristics, and several URANS methods are discussed in more detail. In chapter 4, models for synthetic turbulence are discussed in detail, as well as the current implementation in NRG-FSIFOAM. The new pressure fluctuation model, called *aniPFM*, is explained in chapter 5. The verification & validation, as well as the motivation for certain modelling choices, is given in chapter 6. After this, the new pressure fluctuation model is applied to an FSI case, and the results are discussed in chapter 7. Finally, the main conclusions are wrapped up in chapter 8, and recommendations are given for future work on this topic.

2

Fluid-Structure Interaction

As mentioned in chapter 1, the thesis is focused on improving the prediction of the vibration amplitude of nuclear fuel rods in axial flow, using Fluid-Structure Interaction (FSI) simulations. To simulate fluid-structure interaction, a good review of the basics of FSI is necessary, such that the correct methodologies can be chosen and justified. In this chapter, the governing physics are discussed, as well as the boundary conditions between the interfaces. Then, a review is given of the current NRG-FSIFOAM framework, which is a numerical framework for FSI simulations that couples CFD solver OpenFOAM with the structural solver Deal.II through the coupling library preCICE. Along with this, validation of the current NRG-FSIFOAM framework is given.

2.1. Governing Physics

In this section, the governing physics of FSI problems are reviewed. There are two basic approaches to solve an FSI problem numerically. Namely, the monolithic approach and the partitioned approach [38]. With the monolithic approach, the governing equations of the fluid and structural domain get solved simultaneously. For this, a combined formulation of the governing equations of the fluid and structural domain is necessary. Since the formulation encaptures the full physics, there is no need to couple any sub-problems together. This formulation however, is problem specific and thus monolithic solvers can not directly be applied to other FSI problems than the one it was designed for.

A more general method is the partitioned approach. This approach separates the structural and the fluid domain and solves each domain independently. The domains are typically solved by independent solvers that can be seen as "black box" solvers. The two domains are coupled through a coupling algorithm, which feeds the necessary information and mapping to the two sub-problems. While this approach can be very generalized, it also introduces a coupling error, which depends on the coupling scheme that is used. As the partitioned approach makes use of "black box" solvers, it offers great flexibility in the choice of solvers. Due to its high flexibility, the partitioned approach is often preferred, and this approach will be the focus of this chapter. In this section, the governing equations are discussed, as well as the boundary conditions that are necessary such that the interfaces of the two domains comply.

2.1.1. Structural Dynamics

The structural dynamics are governed by Cauchy's equation of motion [39]. This equation assumes that the domain can be seen as a continuum, and it describes the non-relativistic momentum transport. The equation is given in eq. (2.1), where $\mathbf{u}$ denotes the displacement, σ_s is the Cauchy stress tensor, and $\mathbf{g}_s$ is the specific body force on the structure. The Lagrangian point of view is used for the derivation of this equation, as for the structural domain, this coincides with the ALE reference frame.

$$\rho \frac{\partial^2 \mathbf{u}}{\partial t^2} - \nabla \cdot \sigma_s = \rho \mathbf{g}_s \tag{2.1}$$

For linear elastic behaviour, the stress tensor is related to the strain tensor through Hooke's law [38]. This is a valid assumption as in structural mechanics, the strain is limited since large strains can cause material failure. Hooke's law is given in eq. (2.2) [40], where ϵ_{kl} is the strain tensor and C_{ijkl} is the stiffness tensor. To close the system of equations, a relation between the strain and the displacement is needed. This depends on

the reference frame that is used, in the case of a Lagrangian reference frame, eq. (2.3) is applicable. This is the Green-Lagrange strain tensor and it is valid for both large and small displacements [40]. In the case of small displacements, following infinitesimal strain theory, the strain tensor can be approximated with eq. (2.4). Here, the non-linear and second-order terms are neglected. This implicitly states that the Lagrangian and Eulerian formulation are approximately equal for small displacements. This approximation is valid for the case of $||\nabla \mathbf{u}|| << 1$.

$$\sigma_{ij} = C_{ijkl}\epsilon_{kl} \tag{2.2}$$

$$\epsilon = \frac{1}{2}[\nabla \mathbf{u} + (\nabla \mathbf{u})^T + (\nabla \mathbf{u})^T(\nabla \mathbf{u})] \tag{2.3}$$

$$\epsilon \approx \frac{1}{2}[\nabla \mathbf{u} + (\nabla \mathbf{u})^T] \tag{2.4}$$

2.1.2. Fluid Dynamics

The governing equations of fluid dynamics are the conservation of mass, also known as the continuity equation, the conservation of momentum, and the conservation of energy. To close the system, an equation of state is needed, which relates the density, pressure, and temperature of the fluid. The full conservation of mass and momentum equations are shown in eq. (2.5) and eq. (2.6), respectively. These equations together are called the Navier-Stokes (NS) equations, and they are derived in the Eulerian reference frame. In the equations, ρ is the density, u_i is the velocity in direction i, p is the pressure, τ_{ij} is the viscous stress tensor as defined in eq. (2.7), and f_i is the sum of body forces in direction i.

$$\frac{\partial \rho}{\partial t} + \frac{\partial \rho u_i}{\partial x_i} = 0 \tag{2.5}$$

$$\frac{\partial \rho u_j}{\partial t} + u_i \frac{\partial \rho u_j}{\partial x_i} = -\frac{\partial p}{\partial x_j} + \frac{\partial \tau_i j}{\partial x_i} + \rho f_j \tag{2.6}$$

$$\tau_{ij} = \mu\left(\frac{\partial u_i}{\partial x_j} + \frac{\partial u_j}{\partial x_i} - \frac{2}{3}\frac{\partial u_k}{\partial x_k}\right) \tag{2.7}$$

The conservation equations can be further simplified depending on the application. In the application of FSI calculations of cooling liquid in nuclear reactors, the fluid can be considered incompressible and of constant density. In this case, the Navier-Stokes equations can be rewritten as in eq. (2.8) and eq. (2.9). As can be seen, due to the assumption of incompressible and constant density flow, the conservation of mass is transformed to simply the divergence of the velocity field. As this equation is not time-dependent anymore, it is often referred to as the *divergence constraint*, since it acts as a constraint on the momentum equation for the velocity field. From the divergence constraint, it follows that the last term of eq. (2.7) also drops out. The incompressible flow assumption also decouples the energy equation from the momentum equation, thus, the energy equation can be omitted, if thermal properties are not of interest.

$$\frac{\partial u_i}{\partial x_i} = 0 \tag{2.8}$$

$$\frac{\partial u_j}{\partial t} + \frac{\partial u_i u_j}{\partial x_i} = -\frac{1}{\rho}\frac{\partial p}{\partial x_j} + \frac{1}{\rho}\frac{\partial \tau_{ij}}{\partial x_i} + f_j \tag{2.9}$$

The previously stated equations were derived in the Eulerian reference frame. However, an Arbitrary Lagrangian-Eulerian (ALE) reference frame is more suitable for FSI calculations. The advantage of this method is that the fluid and structural grid do not overlap, as the mesh motion is coupled at the fluid-structure interface. Because of this, the Lagrangian frame of reference is obtained for the structural domain. The Navier-Stokes equations in the ALE reference frame are shown in eq. (2.10) and eq. (2.11). Here c_i is the convective velocity, which is defined as $u_i - \hat{u}_i$, where u_i is the material velocity with respect to the spatial domain, and $\hat{u}_i$ is the mesh velocity with respect to the spatial domain.

$$\frac{\partial c_i}{\partial x_i} = 0 \tag{2.10}$$

$$\frac{\partial u_j}{\partial t} + \frac{\partial c_i u_j}{\partial x_i} = -\frac{1}{\rho}\frac{\partial p}{\partial x_j} + \frac{1}{\rho}\frac{\partial \tau_i j}{\partial x_i} + f_j \tag{2.11}$$

The Navier-Stokes equations govern the behaviour of fluid flows. As can be seen in eq. (2.11), the conservation of momentum contains a nonlinear differential term, namely $\frac{\partial u_i u_j}{\partial x_i}$. Due to this non-linearity, the NS equations are notoriously difficult to solve computationally, as they either require additional assumptions and modelling, or huge computational resources. In chapter 3, methods for solving the NS equations are elaborated upon.

2.1.3. Interface Conditions

The interface between the fluid domain Ω_F and the structural domain Ω_S must be well defined to have a well-posed problem. With fluid-structure interaction, the fluid exerts a force on the structure, whereas the movement of the structure changes the flow field in the fluid domain. This information is propagated through the interface of the two domains, Γ_{FS}, in the form of two interface conditions. An example of this is sketched in fig. 2.1.

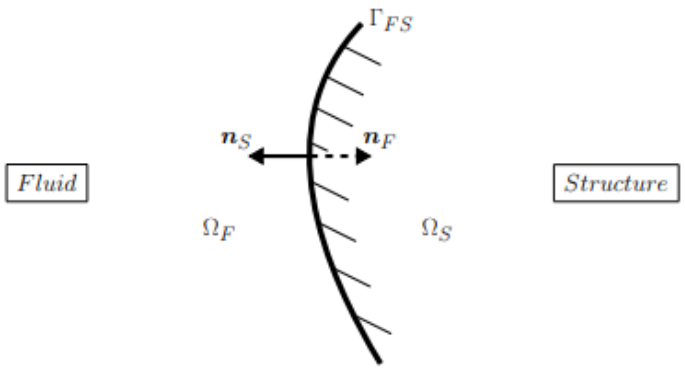

Figure 2.1: Schematic of the interface between the structural and fluid domains [3].

The first condition is the kinematic boundary condition. This condition imposes the no-slip condition at the interface, where the fluid molecules at the interface are attached to the structure, and thus they have the same velocity as the structure. The equality follows from the fact that the fluid grid and the structural grid are non-overlapping and that there are no holes or gaps at the interface. The kinematic boundary conditions at Γ_{FS} are defined in eq. (2.12) and eq. (2.13). Equation (2.12) states that the location of the grid point in the fluid domain at Γ_{FS} is equal to that of the structural domain. Equation (2.13) states that the velocity at the grid points in the fluid domain at Γ_{FS} is equal to that of the structural domain.

$$\mathbf{x}_F = \mathbf{u}_S \tag{2.12}$$

$$\mathbf{u}_F = \frac{\partial \mathbf{u}_S}{\partial t} \tag{2.13}$$

The second type of boundary condition at the interface is the dynamic boundary condition. This condition enforces the equilibrium of forces at the interface. Thus, the traction is equal at both sides, which is expressed by the point-wise surface stresses at the interface [3, 41]. The boundary condition is formulated as in eq. (2.14), where $\mathbf{n}_F$ and $\mathbf{n}_S$ are the outward pointing unit normal vectors of the fluid domain and the structural domain as shown in fig. 2.1, respectively.

$$\sigma_F \cdot \mathbf{n}_F = -\sigma_S \cdot \mathbf{n}_S \tag{2.14}$$

2.2. Application at NRG

In the previous sections, the underlying governing equations of fluid-structure interaction have been discussed, as well as the necessary interface conditions. At Nuclear Research & Consultancy Group (NRG), a framework for solving fluid-structure interaction problems has been set up, called the NRG-FSIFOAM framework. This framework has been mainly used to simulate nuclear fuel rods subjected to axial flow, but it has

also been validated for other cases. In this section, the specifications and validation of NRG-FSIFOAM are reviewed. The framework and its validation are described in more detail by De Santis & Shams [4].

2.2.1. Specifications of NRG-FSIFOAM

The NRG-FSIFOAM framework uses a partitioned approach to FSI, due to its lesser computational complexity and its flexibility. The governing equations of the fluid domain as stated in section 2.1.2 are used. They are solved by the finite volume solver Open-FOAM [42]. In particular, the discretised equations in space are solved by the PIMPLE algorithm, whereas the consistent second-order backward difference method is used to integrate the equations in time. This time method is suitable for FSI applications, as it was developed for moving grids. Radial basis function interpolation [43] is used to deform the fluid mesh. For turbulent flows, a URANS approach is used, where the two-equation $k-\omega$ SST model is used as the turbulence model. Next to this, there is also a Pressure Fluctuation Model (PFM) implemented in NRG-FSIFOAM. The PFM models the pressure fluctuations of the flow, which are then together with the average pressure imposed as excitation on the structure. This enables NRG-FSIFOAM to simulate the effect of pressure fluctuations without using high-fidelity simulations such as LES or DNS. The full PFM model that is implemented in NRG-FSIFOAM is discussed in more detail in section 4.2.

The governing equations of the structural domain as stated in section 2.1.1 are discretised and solved. For this, a finite element approach is used by Deal.II. The governing equations are semi-discretised in space by the linear finite element approximation, and in time, the θ-method is used. Typically, a value of $\theta = 0.6$ was taken in the previously reported use of NRG-FSIFOAM [4].

The two domains are coupled through the open-source library preCICE [44]. This library contains efficient implementations of existing coupling and mapping algorithms, and it is highly parallel. The fluid and structural grids are generally not conforming at the fluid-structure interface, thus the forces and displacements have to be mapped onto the respective structural and fluid grids. For this, radial basis functions are used, which are already implemented in preCICE. Using this method, the displacements are mapped from the structural to the fluid interface in a consistent manner, and the forces are mapped conservatively from the fluid to the structural domain.

Due to the typically low density ratios (ρ_s/ρ_f) in the application of FSI to nuclear reactor related problems, implicit coupling methods are preferred. This is because implicit coupling methods are more robust, and therefore more apt for strongly coupled problems. Within the realm of implicit methods, several have been applied in NRG-FSIFOAM, such as Gauss-Seidel, IQN-ILS and manifold mapping [4, 14, 45]. In the validation cases that are discussed below, the IQN-ILS coupling algorithm is used.

2.2.2. Validation of NRG-FSIFOAM

The NRG-FSIFOAM framework has been validated with numerous test cases, both numerical and experimental. The well-known Turek & Hron benchmarking case has been simulated and the results from NRG-FSIFOAM have been compared to those of Turek & Hron [46]. Furthermore, the framework has been compared to the previously validated FSI framework of STAR-CCM+, which gave similar results in the simulation of vibrating bare and wire-wrapped rods. Finally, the framework has been used to replicate the experiment of Liu et al. [6], in which a cantilever beam is subjected to turbulent axial flow. In this subsection, the most relevant validation cases and their results are discussed.

Turek & Hron

The benchmark case proposed originally by Turek & Hron [46] involves a rigid cylinder with an elastic flap attached to it, which is subjected to laminar incompressible flow, the case is illustrated in fig. 2.2. For the validation of NRG-FSIFOAM, the density of the fluid was taken to be equal to that of the structure, $\rho_f = \rho_s = 1000 kg/m^3$, and the kinematic viscosity is equal to $\nu_f = 10^{-3} m^2/s$. Because the flow is laminar and dominated by vortex-induced vibrations, it is not necessary to utilize the PFM. A parabolic velocity profile is used at the inlet, where the maximum velocity is at channel half-width, and it is equal to $\bar{U} = 2m/s$. Finally, the material of the structure has a Young's modulus of $E = 5.6 \cdot 10^6 Pa$ and a Poisson ratio of $\nu_s = 0.4$. Due to the low solid-to-liquid density ratio, this case is particularly suited to benchmark FSI frameworks that need to simulate strongly coupled problems. The case was solved for three different meshes ranging from coarse to fine. The timestep was kept at $\Delta t = 0.001s$ for all simulations. The set-up as described in section 2.2.1 was used, with the IQN-ILS scheme as coupling algorithm. The manifold mapping algorithm was also used in an attempt to validate it. However, as the simulation with the current implementation of this coupling algorithm

in preCICE was very unstable, no convergence could be reached [45]. Further attempts of validating this algorithm in NRG-FSIFOAM have not been made.

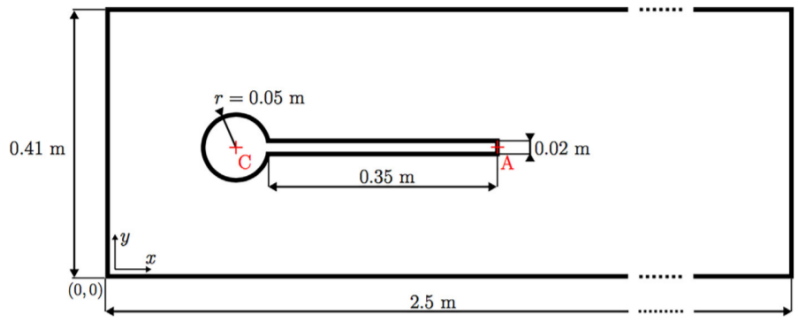

Figure 2.2: The geometry of the Turek & Hron benchmark case [4].

The obtained results for the benchmark case are shown in fig. 2.3 and table 2.1. As can be seen, the results of the NRG-FSIFOAM simulation converge to the reference data of Turek & Hron [46]. For the finest mesh, a discrepancy of only 3% is found. Thus, from these results, it can be concluded that NRG-FSIFOAM can accurately predict the displacements of structures in strongly coupled FSI problems, for laminar flow.

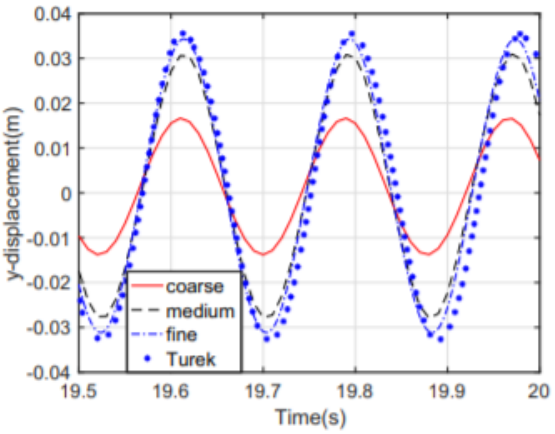

Figure 2.3: The displacement history of the endpoint of the flap, compared to the reference data of Turek & Hron [4].

Table 2.1: Amplitude at the endpoint of the flap, compared to the reference data of Turek & Hron [4].

Case	**Amplitude [m]**
Coarse	0.0146
Medium	0.0289
Fine	0.0330
Reference data	0.0340

Beam in laminar axial flow

Next to the numerical simulation of Turek & Hron [46], the NRG-FSIFOAM framework has replicated experiments as well, such as the Vattenfall-1 test case, which consists of a beam in laminar axial flow. The beam is clamped at the inlet and pinned at the outlet, and an initial displacement of $10mm$ is given in the centre of the beam. After this, the beam is released and the displacement of the beam is monitored [5]. The set-up of the experiment is shown in fig. 2.4. The beam is made of stainless steel with a density of $\rho_s = 8000kg/m^3$, and the Young's modulus is equal to $188GPa$. The fluid is water at $8.4°C$ with a flow velocity of $1m/s$.

The initial displacement had to be imposed in the simulation. This was done by using a smooth ramp function to displace the centre of the beam. In 0.5 seconds the beam was displaced to the required displacement size. During this, both the fluid and structural domains were solved, but traction was ignored. The flow was allowed to settle for 0.1 seconds, and after this, the beam was released and simulated for an additional 0.1 second. The results of the simulation versus the experiment are shown in fig. 2.5. As can be seen, the amplitudes are qualitatively closely matched. Furthermore, it was found that the simulated frequency of oscillation was equal to 9.9 Hz, and the experimental frequency was equal to 10 Hz, giving an error of only 1%. Thus, this experiment has further validated the numerical framework NRG-FSIFOAM for FSI applications to heavily coupled problems in laminar flow.

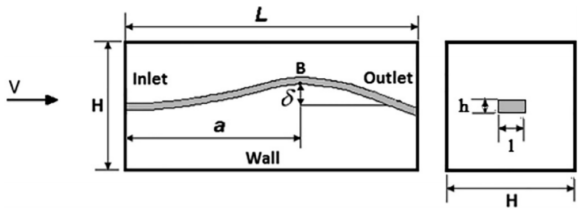

Figure 2.4: The experimental set-up of the Vattenfall-1 test case, the given dimensions are L = 1.5 m, H = 0.8 m, a = 0.75 m, h = 8 mm, l = 20 mm and δ = 10 mm [5].

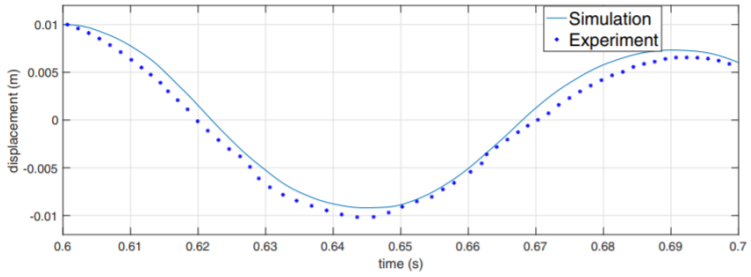

Figure 2.5: The displacement time history of the simulation of the Vattenfall-1 test case [4].

Validation of Turbulent Cases

The previous cases have validated the ability of NRG-FSIFOAM to solve strongly coupled cases in the case of laminar flow. Additional validation was done to show that this is also the case for turbulent flow. For this, a bare and a wire-wrapped rod have been simulated in turbulent axial flow, which has been compared to the previously validated framework that is implemented in STAR-CCM+ [45]. Furthermore, the framework was used to replicate an experiment of a cantilever beam in turbulent axial flow [6].

NRG-FSIFOAM uses the URANS approach for solving the fluid domain. As briefly touched upon in chapter 1, this method is not able to give the instantaneous pressure, which is why a PFM is necessary to fully represent the instantaneous pressure on the wall surfaces. The FSI implementation in STAR-CCM+ does not contain a PFM, thus the NRG-FSIFOAM framework is used both with and without the PFM to compare its results to that of STAR-CCM+. Here, only the results of the bare rod in axial flow are discussed. In table 2.2, the modal characteristics calculated by the different methods are shown. Note that for the simulations without the PFM, an initial impulsive force was necessary to vibrate the bare rod, as the flow as resolved by URANS does not excite the structure. It was found that NRG-FSIFOAM shows excellent agreement with STAR-CCM+, as the calculated frequencies for the simulation without the PFM are within 2% of the values obtained by STAR-CCM+. From table 2.2, it can be seen that there is a discrepancy in the third eigenfrequency for the simulation with the PFM. This could be due to the method of excitation, as for the simulation with the PFM, no initial impulsive force is necessary to excite the structure. While the eigenfrequencies show great resemblance, it was found that the damping ratios were systematically overestimated by NRG-FSIFOAM, compared to STAR-CCM+. In particular, for several cases the damping ratio was overestimated by more than 50%.

Table 2.2: The modal characteristics of the bare rod in turbulent axial water flow [4].

	$f_1[Hz]$	$f_2[Hz]$	$f_3[Hz]$
STAR-CCM+	44.92	142.38	295.24
NRG-FSIFOAM w/o PFM	45.08	145.54	296.93
NRG-FSIFOAM with PFM	46.83	145.03	338.02

Finally, the experiment of Liu et al. [6] was replicated to validate the ability of NRG-FSIFOAM to predict the vibration amplitude of rods in turbulent axial flow. In the experiment, a hollow cylindrical beam is used, which has a length of 1.05 m, with inner and outer diameter of 8.8mm and 10.1mm respectively. It has the same material characteristics as the Vattenfall-1 test case [5]. Water was used as the fluid, with an inflow velocity of 1.49m/s and a density of ρ_f = 997.13kg/m^3. The beam is clamped at the outlet of the domain,

and it is free at the end that is pointing towards the inlet. For clarity, the experimental set-up is shown in fig. 2.6.

The experiment was simulated with NRG-FSIFOAM both with and without the PFM. It was found that the modal characteristics matched those of the experiment, where 5.69 Hz was found in the experiment, and 5.68 Hz was found in the simulations [4]. The maximum displacement was used as a measure to validate the ability to predict the vibration amplitude. With the PFM, the simulation gave an error of roughly 10% in the maximum displacement, as the simulation predicted a maximum displacement of $0.145mm$ in the x-direction, and a maximum displacement of $0.206mm$ in the y-direction, whereas the experiment denoted a maximum absolute displacement of $0.180mm$. Without the PFM, the NRG-FSIFOAM framework estimates a maximal displacement of $4e-4mm$, due to the lack of turbulent excitation. The RMS displacement has sadly not been compared for this case. This gives a more relevant measure of the ability to predict the vibration amplitude, as the maximum displacement is much more sensitive to the random component that is introduced by the PFM. For example, in the study by Kottapalli et al. [14], the RMS amplitude was used as a measure, and it was found that this gave a much larger difference with respect to the experiment, as the RSM amplitudes were only in the same order of magnitude, and thus it was much further off than 10%.

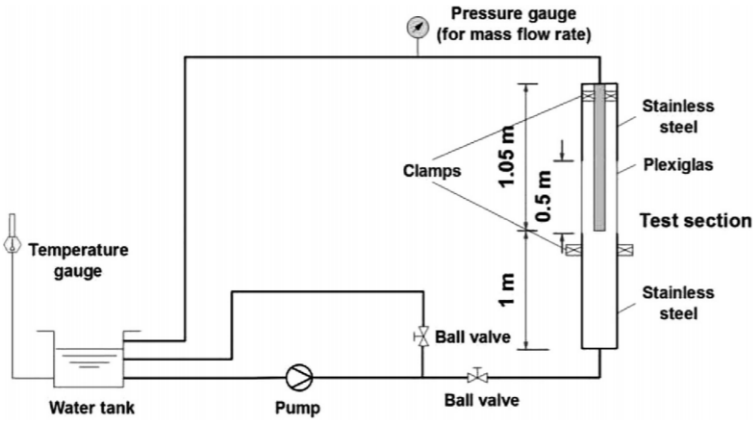

Figure 2.6: The experimental set-up of a cantilever beam subjected to turbulent axial flow [6].

In the previously reviewed validation cases, it was shown that NRG-FSIFOAM can produce accurate results for the amplitude and modal characteristics of FSI problems with laminar flow. Furthermore, it demonstrated the ability to accurately predict the modal frequencies of FSI problems with turbulent flow. When including PFM, it was shown that the prediction of the vibration amplitude was improved for turbulent flows, however at best the prediction gave results in the same order of magnitude. Furthermore, other characteristics such as the damping, or the power spectral density of the amplitudes have not been compared to high-fidelity simulations or experimental data. This gives motivation to improve the currently implemented PFM model and to further validate its effect on the FSI simulations for nuclear fuel rods. The PFM is reviewed in detail in chapter 4, where also several other synthetic turbulence models are reviewed. Because the current NRG-FSIFOAM framework with the IQN-ILS coupling scheme and radial basis function mapping has been extensively validated, it was decided to use the framework with these algorithms for validation cases in the thesis.

2.3. Summary

In this chapter, a review of the important aspects of fluid-structure interaction is given, along with the application of FSI in nuclear reactors. First, the physical representation of FSI was reviewed, which included an overview the governing equations for both the fluid and the structural domain, and the necessary interface conditions to couple the fluid and the structural domain. After the review of the necessary concepts relating to FSI, the implementation in NRG-FSIFOAM was summarized and reviewed. The FSI framework uses a partitioned approach, where OpenFOAM is used for solving the fluid domain, and Deal.II is used to solve the structural domain. The two solvers are treated as black boxes, and they are coupled through preCICE. Several coupling algorithms can be used, but the reviewed validation cases all used the IQN-ILS coupling scheme. In NRG-FSIFOAM, the URANS approach is used for solving the fluid domain, in particular, the $k-\omega$ SST model. To account for pressure fluctuations, a pressure fluctuation model is implemented in OpenFOAM, which im-

poses the pressure fluctuations plus the ensemble-averaged pressure on the structure. From the validation cases, it became clear that NRG-FSIFOAM is capable of accurately calculating the vibration amplitude and frequencies for laminar flow FSI cases and the vibration frequency for turbulent flow FSI case. This framework will be used to validate the new pressure fluctuation model that will be constructed in the thesis. Because the focus of the thesis will be on the accuracy of the pressure fluctuation model rather than the performance of the FSI coupling, the IQN-ILS coupling scheme will be used due to its thorough validation.

3

Turbulence Modelling

From chapter 2, it was found that NRG-FSIFOAM could not accurately predict the vibration amplitude for applications with turbulent flow. This is due to the method that is used for solving the fluid domain, as the current method only solves for the ensemble average velocities. To remedy this, a pressure fluctuation model was implemented, but it still needs to be improved. Possible improvements could be made to the PFM, but for this, an in-dept knowledge of fluid dynamics and turbulence is necessary. For these reasons, apt concepts in fluid dynamics are reviewed. In this chapter, the characteristics of turbulence are assessed, after that the different solving methods are discussed. Then, the focus is shifted on the necessary knowledge for developing a PFM, where the modelling for the Reynolds stress tensor, the governing equation for the pressure fluctuations, and the desired characteristics for a PFM are discussed.

3.1. Characterisation of Turbulence

Turbulence is a notable problem in physics, and it has puzzled scientists since its discovery. It was Horace Lamb who said: "I am an old man now, and when I die and go to heaven there are two matters on which I hope for enlightenment. One is quantum electrodynamics, and the other is the turbulent motion of fluids. And about the former I am rather optimistic." [47]. In this section, first an overview is given of the general characteristics of turbulence, and then the concept of the energy cascade is introduced.

3.1.1. Turbulence Characteristics

While turbulence is a very complex phenomenon, from experimental and numerical studies, certain features that are characteristic to turbulence can be deduced. These characteristics were first reported by Tennekes & Lumley [48] and later updated by Tsinober [49], and they are shortly summarised in this subsection. With this description, it is possible to distinguish turbulent flows from simply chaotic or random flows.

- *Turbulence is chaotic.* This property is intrinsic to turbulence as the chaos is created, given that the Reynolds number is high enough. There is no need for an external excitation such as in the boundary or initial conditions. However, it is extremely sensitive to small disturbances in the initial or boundary conditions. It seems that the cause of this is that turbulence self-amplifies the velocity derivatives. Partly due to the apparent randomness, a statistical approach is often taken to describe turbulence. Do note that while turbulence is chaotic, it is deterministic, and coherent structures are present in turbulence [49].
- *Turbulence has a wide range of scales interaction.* In the application of fluid dynamics in nuclear reactors, the relevant length scales range from meters to fractions of millimeters, and many have a strong interaction. This interaction is caused by the nonlinear term in the NS-equations. Partly due to the many length scales and the complexity of the interaction, statistical approaches are typically taken to describe turbulence [49].
- *Turbulence is statistically stable.* While slightly different initial conditions can completely change the details of the realisation of turbulence, the statistical properties, such as the mean average skin friction or the average Reynolds stress tensor, of both flows are the same. This is another argument for the statistical approach to turbulence [49].

- *Turbulence is rotational and a 3-D phenomenon.* It shows predominant vortex stretching, which points to a production of enstrophy, which is the square of the vorticity. This mainly happens at the larger length scales, and it is dissipated at smaller length scales. Furthermore, there is also a production of strain at the larger scales. Both are due to the self-amplification of the velocity derivatives. For engineering applications, turbulence is always a 3-D phenomenon. This is because in 2-D, only a z-component of the vorticity exists, making it orthogonal to the velocity gradients. This prohibits characteristic features of turbulence such as vortex stretching. It is found that in 2-D "turbulence", smaller scales merge and form larger scales, whereas in 3-D turbulence, the larger scales break down into smaller scales. Thus, for engineering applications, turbulence is always a 3-D phenomenon [49].

- *Turbulence is strongly dissipative and diffusive.* The production of turbulence by the larger scales is counteracted by the dissipation at the smaller scales. Thus, due to the dissipation of the smaller scales, the dissipation is higher than laminar flows. An example of this is the difference in skin friction coefficient for a flat plate in the laminar and turbulent regime. Furthermore, turbulent flow has enhanced transport processes of momentum, energy, and weightless particles [49].

3.1.2. Energy Cascade

The concept of an energy cascade was first introduced by Richardson [50]. It was observed that the larger length scales of the flow produced the turbulent kinetic energy, the larger scales then transfer the energy to slightly smaller length scales. This process is repeated until the energy is dissipated by the smallest length scales. This is not entirely accurate as there is dissipation at every length scale, but it is dominated by the dissipation of the smallest length scales, as the larger length scales can be characterised as approximately inviscid. This energy cascade can be interpreted through the turbulent kinetic energy spectrum. The turbulent kinetic energy is defined in eq. (3.1), but it can also be defined in wavenumber space. The wavenumber κ is directly related to the length scale l of an eddy, $\kappa = \frac{2\pi}{l}$. Then, the turbulent kinetic energy can be defined as the integral of the energy spectrum over the entire wavenumber range, as shown in eq. (3.2).

$$k = \frac{1}{2} u_i' u_i' \tag{3.1}$$

$$k = \int_0^\infty E(\kappa)\, d\kappa \tag{3.2}$$

A special case of turbulence is that of homogeneous isotropic turbulence. This means that the turbulence properties are independent of the reference location, and independent of any rotation or reflection of the coordinate system [51]. For this case, more simplifications can be applied, and a 1-D energy spectrum can represent the turbulent kinetic energy. A sketch of a typical energy spectrum is given in fig. 3.1.

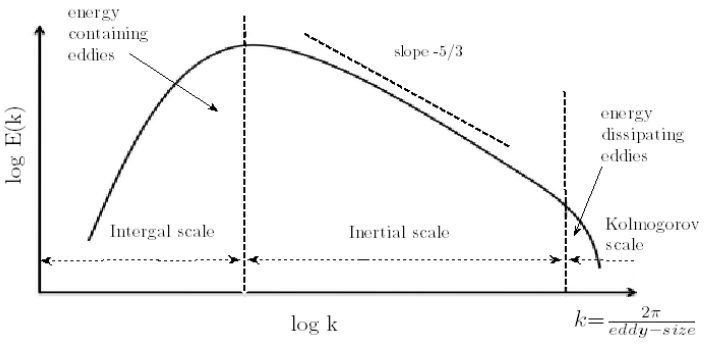

Figure 3.1: A sketch of a typical energy spectrum for homogeneous isotropic turbulence [7].

Kolmogorov [52] stated that the smallest scales are independent of the largest scales, and thus, the smallest scales are entirely determined by the cascaded energy of the larger scales and the kinematic viscosity [53]. Since the production of turbulent kinetic energy mainly occurs at the largest scales, and the dissipation mainly at the smallest scales, there is a range in between, which is purely affected by the energy cascade. These three ranges can be found in fig. 3.1, and they are called the large-scale range, the inertial subrange, and the dissipation range. As mentioned previously, the large scale range produces the turbulence and thus

the turbulent kinetic energy. The large eddies have length and velocity scales that are similar to the mean flow, and thus these scales also depend on the same quantities as the mean flow, such as the boundary conditions and the geometry of the problem [53]. The turbulent kinetic energy that is "produced", is extracted from the mean flow.

In the dissipation range, Kolmogorov stated that the behaviour of the eddies is dominated by the viscosity and the dissipation rate [52, 54]. Using dimensional analysis, it is possible to determine the relevant length, time and velocity scales that characterise these small eddies. The characteristic scales are found by eq. (3.3) through eq. (3.5). Thus the characteristics of the smallest eddies are dependent on general properties of the flow.

$$\eta \sim (\frac{\nu^3}{\varepsilon})^{1/4} \tag{3.3}$$

$$\tau \sim (\frac{\nu}{\varepsilon})^{1/2} \tag{3.4}$$

$$v \sim (\nu\varepsilon)^{1/4} \tag{3.5}$$

If the range between the large scales and the Kolmogorov scales is large enough, a third range can be found, the inertial subrange. In this range, the energy cascade is still of effect, but the dissipation and production of turbulence is negligible. Kolmogorov concluded that in this range, the energy spectrum only depends on the dissipation rate and the length scale of the eddy [52]. From this, using dimensional analysis, the relation from eq. (3.6) can be found.

$$E(\kappa) = C_K \varepsilon^{2/3} \kappa^{-5/3} \tag{3.6}$$

Since the Kolmogorov scales characterise the smallest eddies, that means that it is possible to fully resolve the Navier-Stokes equations, with the requirement that the grid size and timesteps are smaller than the respective Kolmogorov scales. As previously mentioned, the Kolmogorov scales depend on the flow properties, and it can be shown that they are directly related to the characteristic Reynolds number of the flow. The large eddies are approximately inviscid, and its kinetic energy is proportional to its characteristic velocity squared. Furthermore, the dissipation rate can be assumed to be proportional to the turn-over time of the large eddies [53]. Doing so, a similarity for the dissipation rate can be found, as shown in eq. (3.7). Here, the subscript l denotes the characteristics of the largest eddies. From this, the non-dimensional Kolmogorov length scale can be expressed in terms of Reynolds number, as done in eq. (3.8), from which it can be concluded that for large enough Reynolds numbers, an inertial subrange exists.

$$\varepsilon \sim \frac{u_l^3}{l_l} \tag{3.7}$$

$$\frac{\eta}{l_l} \sim \left(\frac{\nu}{u_l l_l}\right)^{-3/4} = (Re_l)^{-3/4} \tag{3.8}$$

3.2. High-Fidelity Methods

Solution techniques for the Navier-Stokes equations can be distinguished by the range of wavenumbers that are resolved. As mentioned in section 3.1.2, turbulence is fully characterised by a finite range of wavenumbers. If the full range of wavenumbers is captured by the simulation technique, the turbulence is fully resolved. Thus, it is possible to fully resolve the turbulence by solving the Navier-Stokes equations on a fine enough grid and with small enough timesteps. High-fidelity methods resolve a larger part of the energy spectrum than low-fidelity techniques. In Direct Numerical Simulations (DNS), the full energy spectrum is resolved, thus eliminating the need for a turbulence model. While DNS would preferably be used in every CFD simulation, it is an incredibly expensive method, due to its strict mesh size and time step requirements. For this reason, it has been mainly applied to simple flow cases at low Reynolds numbers [13, 55].

In section 3.1.2, it was mentioned that only the largest eddies are directly affected by the geometry and boundary conditions, the other scales mostly depend on the energy cascade. Thus, one technique is to resolve the largest eddies, and model the smaller eddies. This is done in Large-Eddy Simulations, which is based on solving the filtered Navier-Stokes equations. The incompressible filtered Navier-Stokes equations are shown

in eq. (3.9) and eq. (3.10). The term $(\overline{u_i u_j} - \bar{u}_i \bar{u}_j)$ is also known as the subgrid stress tensor, and this term needs to be modelled in order to solve the filtered NS equations.

$$\frac{\partial \bar{u}_i}{\partial x_i} = 0 \tag{3.9}$$

$$\rho \frac{\partial \bar{u}_i}{\partial x_i} + \rho \frac{\partial \bar{u}_i \bar{u}_j}{\partial x_j} = -\frac{\partial \bar{p}_i}{\partial x_i} + \frac{\partial}{\partial x_j}(\bar{\tau}_{ij} - \rho(\overline{u_i u_j}) - \bar{u}_i \bar{u}_j)) \tag{3.10}$$

While the computational cost of LES is lower than that of DNS, it is often still too large for practical applications of industry problems [53]. This is more so the case in fluid-structure interaction problems, as each coupling step requires multiple iterations of the fluid solver, and for implicit schemes, the number of sub-iterations increases with decreasing timestep [41]. Thus, the high-fidelity approaches are not directly applicable in industry due to its high computational costs. However, the methods that are described in this section and the previous section are valuable for constructing a synthetic turbulence model, as they provide knowledge in the important characteristics that the synthetic turbulence model must replicate.

3.3. Reynolds-Averaged Method

A lower-fidelity method is to not solve for the instantaneous properties, but for the averaged properties. This can be done by applying Reynolds averaging to the NS equations, this method is called the Reynolds Averaged Navier Stokes (RANS) method. The following methods have been described by Ferziger [56] and Wilcox [57] among others, and the description below is based on their explanations. As OpenFOAM is used for CFD simulations, only methods that are available in OpenFOAM are discussed. With Reynolds averaging, the velocity is decomposed into the mean value and the fluctuating value, as seen in eq. (3.11). The mean value can be determined by a time-average for statistically steady flows, but in the case of unsteady flows, the mean value varies. In this case, the mean value is seen as an ensemble average, which is defined in eq. (3.12). The RANS method applied to unsteady flows is called URANS. The averaging in URANS will eliminate the small turbulent fluctuations, but the larger scales will still be captured [56].

$$u = \bar{u} + u' \tag{3.11}$$

$$\bar{u} = \lim_{N \to \infty} \frac{1}{N} \sum_{N} u \tag{3.12}$$

From the NS equations, the Reynolds averaged NS equations can be constructed. As incompressible flow is more apt for the thesis, only the incompressible form without body forces will be considered. The result of Reynolds averaging is shown in eq. (3.13) and eq. (3.14). As can be seen, the equations are very similar to the original NS equations, except there is an additional unknown term $-\rho \overline{u_i' u_j'}$ at the right-hand side. This term follows from the nonlinear term that is present in the NS equations, it introduces 6 additional unknowns to the system, and it is called the Reynolds stress tensor. Due to the 6 additional unknowns, extra assumptions must be made and additional equations must be introduced in order to create a closed system of equations. Several methods exist to close this system, however, the focus will be on the 2-equation eddy viscosity methods and the Reynolds stress transport methods.

$$\frac{\partial \bar{u}_i}{\partial x_i} = 0 \tag{3.13}$$

$$\frac{\partial \bar{u}_j}{\partial t} + \frac{\partial \bar{u}_i \bar{u}_j}{\partial x_i} = -\frac{1}{\rho}\frac{\partial \bar{p}_j}{\partial x_j} + \frac{1}{\rho}\frac{\partial}{\partial x_i}(\bar{\tau}_{ij} - \rho \overline{u_i' u_j'}) \tag{3.14}$$

3.3.1. Two-Equation Methods

Linear eddy viscosity models, of which most 2-equation methods are part of, are all based on the Boussinesq hypothesis [57]. This hypothesis states that the Reynolds stress tensor can be seen as a stress that is similar to the shear stress, and thus this suggests that the Reynolds stress can be modelled by means of a turbulent viscosity, from here on named the eddy viscosity. From the hypothesis, the expression from eq. (3.15) followed, where S_{ij} is the strain rate tensor. Then, only an apt expression for the eddy viscosity μ_t has to be found. For this, methods were formulated that contained 0, 1, or 2 additional Partial Differential Equations

(PDEs). While the Boussinesq hypothesis provides a simple relation for the Reynolds stress tensor, there are two main flaws that can cause inaccurate CFD predictions. Firstly, the eddy viscosity is modelled as a scalar, which implies that the turbulent viscosity is isotropic. Secondly, from eq. (3.15), it can be found that the RMS of the velocity fluctuations are equal in every direction, $\overline{u'^2} = \overline{v'^2} = \overline{w'^2}$. This implies that the kinetic energy is equally distributed in all three directions, whereas this is not found in high-fidelity simulations [55]. Despite the flaws of the Boussinesq hypothesis, eddy viscosity models have shown to give accurate results for certain flow cases, and they are the industry standard [57]. In particular, two-equation models show desirable results with respect to their computational requirements, and they are the most often used models across several industries [57], thus these will be elaborated upon.

$$-\rho\overline{u_i'u_j'} = 2\mu_t\bar{S}_{ij} - \frac{2}{3}\rho k\delta_{ij} \tag{3.15}$$

The basis of 2-equation models is to solve the transport equation for turbulent kinetic energy k, along with a second differential equation to close the system. The transport equation for k can be derived by taking the trace of the Reynolds stress transport equation, but several complicated terms such as triple correlations occur [57]. To simplify, the turbulent transport and diffusion terms are approximated by a gradient-like term. The simplified transport equation for k is shown in eq. (3.16), where σ_k is a modelling constant. The dissipation ε is unknown, which is found through another PDE, in the case of a 2-equation method.

$$\rho\frac{\partial k}{\partial t} + \rho\bar{u}_i\frac{\partial k}{\partial x_i} = -\rho\overline{u_i'u_j'}\frac{\partial\bar{u}_j}{\partial x_i} - \rho\varepsilon + \frac{\partial}{\partial x_i}\left[(\mu + \frac{\mu_t}{\sigma_k})\frac{\partial k}{\partial x_i}\right] \tag{3.16}$$

$k-\varepsilon$ Method

The $k-\varepsilon$ method uses an additional transport equation for the dissipation to complete the system of equations. While an exact equation for ε is possible, it contains again many terms with triple correlations. Instead, Jones & Launder [58] postulated a transport equation for the dissipation with additional model constants. The equation for the dissipation is found in eq. (3.17), and eq. (3.18) is used as an expression for the eddy viscosity, which is based on dimensional analysis. The values for the coefficients can be found in Wilcox [57]. The model gives good results for external aerodynamics, but only for cases without strong streamline curvature, strong pressure gradients or separation [53]. This is partly due to its performance in near-wall regions, and a wall model is necessary.

$$\frac{\partial\varepsilon}{\partial t} + \rho\bar{u}_i\frac{\partial\varepsilon}{\partial x_i} = -\rho\overline{u_i'u_j'}C_{\varepsilon1}\frac{\varepsilon}{k}\frac{\partial\bar{u}_j}{\partial x_i} - C_{\varepsilon2}\rho\frac{\varepsilon^2}{k} + \frac{\partial}{\partial x_i}\left[(\mu + \frac{\mu_t}{\sigma_t})\frac{\partial\varepsilon}{\partial x_i}\right] \tag{3.17}$$

$$\mu_t = C_\mu\rho\frac{k^2}{\varepsilon} \tag{3.18}$$

$k-\omega$ & SST Method

The $k-\omega$ method proposed by Wilcox [59] postulates a transport equation for the specific turbulence dissipation rate ω, which is defined in eq. (3.19). The transport equation has a similar form to eq. (3.17), and it is shown in eq. (3.20). Finally, the eddy viscosity is defined as in eq. (3.21). While the differences in formulation with respect to the $k-\varepsilon$ method are small, they give a large effect. The method shows better results for boundary layer flows, strong pressure gradients and separation prediction than the $k-\varepsilon$ method. However, this method shows more sensitivity to the prescribed turbulence properties at the inlet.

$$\omega = \frac{1}{C_\mu}\frac{\varepsilon}{k} \tag{3.19}$$

$$\frac{\partial\omega}{\partial t} + \rho\bar{u}_i\frac{\partial\omega}{\partial x_i} = -\rho\overline{u_i'u_j'}\alpha\frac{\omega}{k}\frac{\partial\bar{u}_j}{\partial x_i} - \beta\rho\omega k + \frac{\partial}{\partial x_i}\left[(\mu + \sigma\mu_t)\frac{\partial\omega}{\partial x_i}\right] \tag{3.20}$$

$$\mu_t = \rho\frac{k}{\omega} \tag{3.21}$$

The $k-\omega$ SST method was introduced by Menter [60], and it combines the features of the $k-\varepsilon$ and the $k-\omega$ method. The method uses the $k-\omega$ formulation in boundary layers, and it switches to the $k-\varepsilon$ formulation in the free stream. This ensures that the boundary layer can be correctly resolved, and it does not show the sensitivity to the inlet conditions that is present with the $k-\omega$ method. For these reasons, the $k-\omega$ SST method is the preferred linear eddy viscosity 2-equation model.

Cubic $k-\varepsilon$ method

The previous two discussed methods were based on the Boussinesq hypothesis, which states that the Reynolds stress tensor varies linearly with the strain tensor, which results in the assumption of isotropic turbulence. One method to create a more accurate representation of the Reynolds stress tensor is to assume that the Boussinesq hypothesis is simply the leading term of a series expansion [57]. Such a method, the Lien Cubic $k-\varepsilon$ method, is also implemented in OpenFOAM. The implemented method is based on the paper by Craft et al. [61], which is an adjusted version of the original method of Lien. This method expands the Boussinesq hypothesis up to cubic terms. In OpenFOAM, also a quadratic $k-\varepsilon$ model is available. However, the only difference with the Cubic $k-\varepsilon$ model is the number of expansion terms of the Boussinesq hypothesis, thus due to the similarity, this model is not further discussed.

Consider the definition of the tensor a_{ij} in eq. (3.22), which defines its relationship with the Reynolds stress tensor. In eq. (3.23) Craft et al. expand the Boussinesq hypothesis for a_{ij} up to cubic terms, where $\tilde{\varepsilon}$ is the adjusted dissipation rate as defined in eq. (3.24), and the terms c_1 through c_6 are closure coefficients. Except for the relation between the Reynolds stress tensor and the eddy viscosity, the cubic $k-\varepsilon$ method is equal to the linear eddy viscosity $k-\epsilon$ method, i.e. the model still solves the transport equations as shown in eq. (3.16) and eq. (3.17).

$$a_{ij} \equiv \frac{\overline{u_i u_j} - \frac{2}{3}\delta_{ij}k}{k} \tag{3.22}$$

$$\begin{aligned} a_{ij} = &-\frac{\nu_t}{k}S_{ij} + c_1\frac{\nu_t}{\tilde{\varepsilon}}\left(S_{ik}S_{jk} - 1/3S_{kl}S_{kl}\delta_{ij}\right) \\ &+ c_2\frac{\nu_t}{\tilde{\varepsilon}}\left(\Omega_{ik}S_{jk} + \Omega_{jk}S_{ik}\right) \\ &+ c_3\frac{\nu_t}{\tilde{\varepsilon}}\left(\Omega_{ik}\Omega_{jk} - 1/3\Omega_{kl}\Omega_{kl}\delta_{ij}\right) \\ &+ c_4\frac{\nu_t k}{\tilde{\varepsilon}^2}\left(S_{ki}\Omega_{lj} + S_{kj}Q_u\right)S_{kl} \\ &+ c_5\frac{\nu_t k}{\tilde{\varepsilon}^2}\left(\Omega_{iI}\Omega_{lm}S_{mj} + S_{il}\Omega_{lm}\Omega_{mj} - \frac{2}{3}S_{lm}\Omega_{mn}\Omega_{nl}\delta_{ij}\right) \\ &+ c_6\frac{\nu_1 k}{\tilde{\varepsilon}^2}S_{ij}S_{kl}S_{kl} + c_7\frac{\nu_t k}{\sigma^2}S_{ij}\Omega_{kl}\Omega_{kl} \end{aligned} \tag{3.23}$$

$$\varepsilon = \tilde{\varepsilon} + 2\nu\left(\frac{\partial\sqrt{k}}{\partial x_j}\right)^2 \tag{3.24}$$

Next to the cubic $k-\varepsilon$ model, other non-linear models exists based on the $k-\omega$ formulation, such as the cubic BSL $k-\omega$ method. Similar to the cubic $k-\varepsilon$ model, the largest difference with the BSL $k-\omega$ method is the expansion of the Boussinesq hypothesis. Thus, the $k-\omega$ based methods show similar features as the original $k-\omega$ method, such as sensitivity to the prescribed turbulence properties at the inlet. Nonlinear eddy viscosity models based on the $k-\omega$ formulation are not available in OpenFOAM. However, in nuclear applications for rod bundles, $k-\varepsilon$ models are often used [62].

One extra difference between the linear and the cubic $k-\varepsilon$ methods, is that the closure coefficient C_μ is not a constant anymore in the cubic method. A constant C_μ typically results in an over prediction of turbulent energy in stagnation regions and regions of impingement [63]. Due to its similar formulation to the linear $k-\varepsilon$ method, it is only 10% computationally more expensive [61], making it an attractive substitute to linear eddy viscosity models. While the cubic $k-\varepsilon$ improves the modelling of the Reynolds stress tensor, it still assumes a scalar value for the eddy viscosity, and the closure coefficients are based on experimental data [62]. While eddy viscosity models give accurate results for certain types of flows, more accurate models are desired which can better predict the Reynolds stress. Such models are discussed in the next subsection.

3.3.2. Reynolds Stress Models

A big limitation of the discussed eddy viscosity models is the Boussinesq hypothesis, or the extension thereof. This hypothesis implicitly states that the turbulent viscosity is isotropic, as a scalar quantity (μ_t) is used to model turbulence. A family of methods that do not use the Boussinesq hypothesis, is the family of Reynolds Stress Models (RSM). With these models, the Reynolds stress transport equations are approximated, this usually results in 7 additional equations. The exact Reynolds stress transport equation can be derived from the

NS equations, and it is shown in eq. (3.25). For the full formulation of each term, the reader is referred to [57]. From the terms on the right-hand side of eq. (3.25), T_{ij}, D^p_{ij}, Φ_{ij} and ε_{ij} can not directly be computed from mean flow quantities. However, from DNS data and experimental data, it was found that the pressure diffusion term D^p_{ij} is negligible [57].

$$\frac{\partial \overline{u_i' u_j'}}{\partial t} + \bar{u}_k \frac{\partial \overline{u_i' u_j'}}{\partial x_k} = \overbrace{P_{ij}}^{Production} + \underbrace{T_{ij} + D^v_{ij} + D^p_{ij}}_{Diffusion} + \overbrace{\Phi_{ij}}^{Pressure-strain} - \underbrace{\varepsilon_{ij}}_{Dissipation} \tag{3.25}$$

From the discussion in section 3.1.2, it became clear that the dissipation is mainly concentrated at the smallest scales. Thus, as this happens mainly at the smallest eddies, the dissipation is often assumed to be isotropic [52, 56]. Then, the dissipation term is modelled as in eq. (3.26), where the scalar dissipation is often solved by using the dissipation transport equation from the $k-\varepsilon$ method or the specific turbulence dissipation transport equation from the $k-\omega$ method.

$$\varepsilon_{ij} = \frac{2}{3}\varepsilon \delta_{ij} \tag{3.26}$$

The transport term T_{ij} contains the derivative of the triple correlation $\overline{u_i' u_j' u_k'}$. First it was argued that the easiest approximation for the triple correlation would be in the form of the derivative of the Reynolds stress, i.e. as shown in eq. (3.27) [64]. However, this form would be inconsistent with the fact that the triple correlation is rotationally invariant [57]. Later, the form in eq. (3.28) by Launder et al. [65] was proposed, which is used in the LRR RSM. In this form, the approximation is also rotationally invariant.

$$\overline{u_i' u_j' u_k'} \sim \frac{\partial \overline{u_i' u_j'}}{\partial x_k} \tag{3.27}$$

$$\overline{u_i' u_j' u_k'} = \frac{2}{3} C_s \frac{k^2}{\varepsilon} \left[\frac{\partial \overline{u_j' u_k'}}{\partial x_i} + \frac{\partial \overline{u_i' u_k'}}{\partial x_j} + \frac{\partial \overline{u_i' u_j'}}{\partial x_k} \right] \tag{3.28}$$

The main differences between Reynolds stress models typically lie in the method of modelling the pressure strain term. The pressure strain term can be divided into two parts, the slow term (denoted with superscript s in eq. (3.29)) models the return to isotropic state, whereas the rapid term (superscript r in eq. (3.29)) models the immediate effect. The LRR RSM by Launder et al. [65] only models the linear term of both the slow and the rapid term, whereas the SSG RSM by Speziale et al. [66] also model the quadratic terms.

$$\Phi_{ij} = \Phi^S_{ij} + \Phi^R_{ij} \tag{3.29}$$

Next to the modelling of the pressure-strain term, the Reynolds stress models also differ in the calculation of the scalar dissipation. Several models such as the SSG RSM and the LLR RSM are based on the ε transport equation. However, the RSM proposed by Wilcox & Rubesin [67] or the SMC RSM [57] and others are based on the ω transport equation, which allows more accurate near-wall treatment. Since the Reynolds stress tensor is symmetric, eq. (3.25) gives six additional PDEs, and an extra PDE is necessary to calculate ε, thus in total seven additional PDEs need to be solved with Reynolds stress models. While this gives the individual Reynolds stresses and it can account for anisotropy, it also requires significant extra computational power compared to 2-equation models.

A compromise between these methods would be an Explicit Algebraic Reynolds Stress Model (EARSM). These models are similar to nonlinear eddy viscosity models, except the constitutional relationship is derived from the full Reynolds stress transport equations [57]. Most famous is the EARSM developed by Wallin & Johansson [68], newer methods are based on their stress-strain relationship [69].

3.4. Governing Equation of Pressure Fluctuations

With the reviewed turbulence modelling methods in section 3.3, confidence is established in the ability to create URANS simulations for the desired FSI cases. The next step is to review the knowledge that is necessary to create a pressure fluctuation model. As the PFM must model the pressure fluctuations, it is necessary to derive how this quantity relates to the Navier-Stokes equations and the URANS equations. In the conservation of momentum equation, the decomposition of the velocity $u = \bar{u} + u'$ and pressure $p = \bar{p} + p'$ is substituted, as

shown in eq. (3.30). Then, the URANS conservation of momentum is subtracted, and the divergence operator is applied. From this, eq. (3.31) is found.

$$\frac{\partial(\bar{u}_j + u'_j)}{\partial t} + \frac{\partial(\bar{u}_i + u'_i)(\bar{u}_j + u'_j)}{\partial x_i} = -\frac{1}{\rho}\frac{\partial(\bar{p} + p')}{\partial x_j} + \frac{1}{\rho}\frac{\partial}{\partial x_i}\tau_{ij} \tag{3.30}$$

$$\frac{\partial^2 p'}{\partial x_i \partial x_i} = -\rho\left[2\frac{\partial \bar{u}_i}{\partial x_j}\frac{\partial u'_j}{\partial x_i} + \frac{\partial^2}{\partial x_i \partial x_j}\left(u'_i u'_j - \overline{u'_i u'_j}\right)\right] \tag{3.31}$$

Interestingly, eq. (3.31) shows that the pressure fluctuations can be solved for by solving a Poisson equation. Furthermore, it shows that the pressure fluctuations are only dependent on the mean flow velocities, which are available from the URANS simulation, and the velocity fluctuations. Thus, in order to model the pressure fluctuations, only the velocity fluctuations have to be modelled. Equation (3.31) has been used in previous literature to establish a relation for the pressure fluctuations, and it was found that the contributions to the pressure fluctuations can be decomposed into a rapid and a slow term [57, 70], which was earlier established when the pressure-strain term of the Reynolds stress transport equations were discussed (section 3.3.2). The rapid term is the first right-hand side term in eq. (3.31), and it varies quickly with respect to flow conditions. The slow term is the second right-hand side term in eq. (3.31), it is also called the turbulence-turbulence interaction term as it solely depends on the velocity fluctuations.

3.5. Characteristics for Synthetic Turbulence

Since only the velocity fluctuations have to be modelled for the PFM, the focus of the thesis will be on modelling Synthetic Turbulence (ST). In this section, the favourable characteristics of synthetic turbulence will be elaborated upon. These characteristics form the basis for the search of applicable synthetic turbulence models, and they will be used to evaluate which ST model is the most apt. The favourable characteristics are based on the Navier-Stokes equations, the governing equation for pressure fluctuations, and the general characteristics of turbulence as discussed in section 3.1.

3.5.1. Governing Equations

Ideally, the sum of the ensemble-averaged velocity and velocity fluctuations would adhere to the Navier-Stokes equations, however, to achieve this, DNS is needed, and the velocity fluctuations are not modelled but calculated. While satisfying the exact NS-equations is not feasible, an approximation of the NS-equations can be satisfied. Consider the continuity equation for incompressible flow in eq. (3.32), where the velocity u is decomposed into its Reynolds average and its fluctuating component. From the results of eq. (3.13), it is found that the velocity fluctuations must also satisfy the divergence constraint, i.e. its divergence must be equal to zero.

$$\frac{\partial(\bar{u}_i + u'_i)}{\partial x_i} = \frac{\partial \bar{u}_i}{\partial x_i} + \frac{\partial u'_i}{\partial x_i} = 0 \Rightarrow \frac{\partial u'_i}{\partial x_i} = 0 \tag{3.32}$$

For the conservation of momentum, several assumptions are made. As mentioned in section 3.1, the larger eddies can be assumed to be inviscid, thus the Euler equations as shown in eq. (3.33) can be used as an approximation to describe the flow. By filling in the Reynolds decomposition, and assuming that the flow is negligibly accelerated by the local pressure gradient, eq. (3.34) is constructed. Finally, by assuming that $u'_i << \bar{u}_i$, it is found that the velocity fluctuations should be convected by the local mean flow velocity, which is also known as Taylor's frozen wake hypothesis [71]. From comparison to DNS data of turbulent channel flow, it was found that the correlation implied from eq. (3.34) is greater than 0.85 for the entire flow field, and greater than 0.96 for $y^+ > 30$. Thus, the approximation that eddies are convected by the local mean velocity seems to hold accurately.

$$\frac{\partial u_i}{\partial t} + u_k\frac{\partial u_i}{\partial x_k} + \frac{1}{\rho}\frac{\partial p}{\partial x_i} = 0 \tag{3.33}$$

$$\frac{\partial u'_i}{\partial t} + \bar{u}_k\frac{\partial u'_i}{\partial x_k} + \cancelto{\approx 0}{u'_k\frac{\partial u_i}{\partial x_k}} = 0 \tag{3.34}$$

3.5.2. The Energy Spectrum

From section 3.1, it was found that the properties of turbulence differed for different length scales. This could be summarised by representing the turbulent kinetic energy as a continuous energy spectrum of wavenumbers, where the wavenumbers are inversely proportional to the eddy length scales. Thus, in order to get an accurate representation of turbulence, this energy distribution must be reproduced. By accurately representing the energy spectrum, each eddy length scale gets a realistic amount of kinetic energy, and this directly influences the magnitude of the velocity fluctuations.

Another property of turbulence is the wide range of scale interactions. While turbulence may seem chaotic, coherent structures exists and interact with each other. Thus, spatial correlation exists in turbulence, and the synthetic turbulence can not be represented by a white noise field. This spatial correlation is also implicitly modelled through the turbulent kinetic energy spectrum, as the energy spectrum tensor of a velocity signal is defined as the Fourier transform of the auto correlation function of that series [72]. Thus, by accurately modelling the energy spectrum, the spatial correlation functions are implicitly also accurately modelled.

In the case of applications of synthetic turbulence to FSI, it is theorised that not the whole energy spectrum needs to be accurately represented. By using Taylor's frozen wake hypothesis, the wavenumber spectrum can be converted into a frequency spectrum. Then, it is theorised that the structure's excitation will mainly come from the pressure fluctuations that are in the range of the structure's eigenfrequency. Thus only this region of the spectrum would have to be accurately modelled. If this is true, this could reduce the computational power that is necessary for the synthetic turbulence model. However, for the current thesis, the first priority is establishing an accurate synthetic turbulence model, and further research in this area for the optimisation of computational resources is left as a recommendation for future work.

3.5.3. Anisotropy

The Reynolds stress tensor is of importance to create accurate synthetic turbulence. As can be seen in eq. (3.31), it directly affects the calculation for the pressure fluctuations. It is also of importance for accurately modelling the degree of anisotropy of the synthetic turbulence. One measurement of anisotropy of the flow is the distribution of kinetic energy. For isotropic turbulence, it is assumed that the kinetic energy is equally distributed among all three spatial directions. However, in practice, near-wall turbulence shows an anisotropic distribution of kinetic energy. Since the Reynolds stress tensor is directly related to the anisotropy of the energy distribution, for synthetic turbulence it is important to accurately replicate the Reynolds stress tensor.

3.5.4. Temporal decay

One of the characteristics of turbulence that was mentioned in section 3.1, was its strongly dissipative nature. Due to the dissipation, turbulence is decayed. Indeed, in cases where there is no production of turbulence, such as a homogeneous isotropic box, turbulence decay can be found [11]. Due to the constant production and dissipation of turbulence, a temporal decorrelation can be found in turbulence. Thus, in terms of temporal correlation, the convection relation is not an accurate enough approximation of the conservation of momentum. From this, it was concluded that the decorrelation through production and decay of turbulence must be modelled separately.

3.5.5. Summary of Characteristics

From the review on turbulence and its characteristics, several requirements were found to accurately model synthetic turbulence. Firstly, it must adhere to the continuity equation, i.e. the divergence constraint, as well as the simplified momentum equation. Secondly, to model an accurate distribution of energy and accurate spatial correlation, the kinetic energy spectrum must be replicated. Thirdly, the Reynolds stress tensor must be replicated to account for the anisotropy of the flow. Finally, the synthetic turbulence must show the temporal decorrelation that is caused by turbulence production and decay.

3.6. Modelling the Reynolds Stress Tensor

As mentioned in section 3.5, a requirement for the synthetic turbulence model is to accurately replicate the Reynolds stress tensor. However, this also implies that it is important for the URANS solution to give an accurate Reynolds stress tensor as input. The accuracy of the Reynolds stress tensor depends on the URANS method that is used. For Reynolds stress models, the accuracy of the Reynolds stress tensor is typically higher than linear and nonlinear eddy viscosity models [57], due to its direct modelling of the transport equations of

the Reynolds stress tensor.

Linear eddy viscosity models imply that the RMS velocity fluctuations are isotropic, however it has been shown that in practice this is not the case for the near-wall flow [57]. Thus if a method such as the $k-\omega$ SST method is used, the synthetic turbulence would be isotropic even if it could model anisotropy. To counteract this, there are several methods that can more accurately reconstruct the Reynolds stress tensor from URANS data, based on empirical findings. These methods are not necessary for nonlinear eddy viscosity models, as they do not assume isotropy in the RMS velocity fluctuations.

Laraufi et al. [73] investigated these empirical methods for the implementation to synthetic turbulence. Note that the methods are only applicable for the diagonal terms of the Reynolds stress tensor, thus the cross-terms of the Reynolds stress tensor are still evaluated through the Boussinesq hypothesis. The two most notable methods were the method based on Wilcox's hypothesis, and the empirical model by Marusic & Kunkel [74]. The Wilcox's hypothesis method based the velocity fluctuations on Wilcox's nonlinear eddy viscosity model [67]. From this, the relations of the velocity fluctuations to the kinetic energy are given in eq. (3.35) through eq. (3.37).

$$\overline{u'u'} = \frac{8}{9}k \tag{3.35}$$

$$\overline{v'v'} = \frac{4}{9}k \tag{3.36}$$

$$\overline{w'w'} = \frac{6}{9}k \tag{3.37}$$

The second method was the method of Marusic & Kunkel [74]. Here, the empirical model was based on the attached eddy hypothesis, and it takes into account the effect of the Reynolds number. For the full description of this method, the reader is referred to the original paper of Marusic & Kunkel [74]. Due to the empirical nature of the model, it is only valid for $Re_\theta > 3200$ and for zero pressure gradient flows. From the assessment by Laraufi et al. [73], it was found that Wilcox's hypothesis was mainly valid for $y^+ > 100$, and for smaller y^+-values, it showed a larger discrepancy. The method of Marusic & Kunkel showed better results for the inner part of the boundary layer, but only for $Re_\theta > 3200$. Thus, due to its more general application and its ease of implementation, Wilcox's hypothesis is the preferred method to compute the diagonal terms of the Reynolds stress tensor, especially if wall-models are used. With this information, the reconstruction of the Reynolds stress tensor based on Wilcox's hypothesis can be compared to that of the cubic $k-\varepsilon$ method, and the LLR RSM. From the comparison, an apt turbulence model can be selected that will be used for subsequent simulations.

3.7. Summary

In this chapter, the literature regarding turbulence, its characteristics, and the modelling thereof has been reviewed. First, observations of the general characteristics of turbulence were made. From these observations, a more quantitative characterisation of turbulence could be made, with the use of the turbulent kinetic energy spectrum. It was found that large scales mainly produced the turbulent energy by subtracting energy from the mean flow. The dissipation was mostly due to the smallest scales, which are characterized by the Kolmogorov scales. As the smallest scales have a finite length, it is possible to completely resolve the turbulence spectrum and thus there is no need for a turbulence model. Another method is to resolve the scales up to in the inertial subrange, and model the smallest scales. However, these methods are too computationally expensive for current industry applications, and thus a different method must be used.

From this, Reynolds-averaged methods were introduced as a more cost-effective method. Here, only the ensemble average of the flow field is computed. Due to the nonlinearity of the NS-equations, a Reynolds stress term appears in the Reynolds-averaged NS equations, which needs to be modelled. Linear eddy viscosity models assume the Boussinesq hypothesis to model the Reynolds stress tensor, which implies isotropy in the turbulent kinetic energy. A relatively cheap improvement is a nonlinear eddy viscosity model, which does not assume isotropy in turbulent energy, but the turbulent viscosity is still modelled as a scalar, and closure coefficients are necessary to close the system. Reynolds stress models do not use a constitutive relation between the Reynolds stress term and the strain of the mean velocity, but rather they solve the transport equations for the individual Reynolds stress terms.

With the clear distinction between the different methods of modelling turbulence, the governing equation for the pressure fluctuations was investigated. It was found that the pressure fluctuations can be computed solely from the mean velocities and the velocity fluctuations, thus rather than modelling the pressure fluctuations, the velocity fluctuations could be modelled. This is also known as modelling synthetic turbulence. For synthetic turbulence, the desired characteristics were derived. From the Navier-Stokes equations, it was found that the synthetic turbulence must obey a divergence criterion, and that eddies are approximately

convected by the local mean flow velocity. The energy spectrum must be accurately approximated, as it determines the amount of energy the different scales have, and it implicitly determines the spatial correlations between the velocity fluctuations. In order to accurately portray the energy spectrum, the Reynolds stress tensor must be replicated, as it directly influences the size and skewness of the energy spectrum. For linear eddy viscosity models, Wilcox's hypothesis can be used as a better reconstruction method for the Reynolds stress tensor. Lastly, due to the production and dissipation of turbulence, it shows a decorrelation in time. Thus next to convection, this decorrelation must also be modelled. With these characteristics in mind, the available synthetic turbulence methods are reviewed, which is done in chapter 4.

4

Synthetic turbulence

As discussed in section 3.4, the pressure fluctuation field for an incompressible flow can be obtained by solving a Poisson equation, of which the right-hand-side only depends on the averaged velocity field, and the velocity fluctuation field. Thus pressure fluctuations are directly related to the velocity fluctuations, and only the velocity fluctuations need to be modelled, as the averaged velocity field is obtained from a URANS simulation. A modelled velocity fluctuation field is also called Synthetic Turbulence (ST). In this chapter, first, a small overview is given of the research areas where synthetic turbulence is applied. Then, the method of generating synthetic turbulence currently applied in NRG-FSIFOAM is presented, along with its assumptions. Subsequently, a review is given of the current state-of-the-art synthetic turbulence generators from the aforementioned research areas. The given ST generators are reviewed critically, and arguments are presented for the methods that are most suitable for the application of FSI calculations on fuel rods subjected to axial flow.

It was found that there are discrepancies in notation for certain common variables among the different authors. It was decided to keep consistency with the original authors when discussing a synthetic turbulence method, such that the notation is not confusing when one decides to dig further into a specific method. Note that this means that in this chapter, different variable names are used per method, depending on what the original authors used.

4.1. Research areas

Synthetic turbulence has been applied in several fields within computational fluid dynamics. It has been proven to be useful for constructing the inflow conditions for LES and DNS [72, 75–81], it has been used for noise modelling [10, 82–86], particle dynamics modelling [75], hybrid LES-RANS transition regions [9, 73, 87–91], modelling of pressure forces on tall buildings [92], the modelling of fatigue loading on wind turbines [93–95], and for FSI predictions of fuel rods subjected to axial flow [4, 14, 36]. In this section, a small overview is given of the largest research areas and how synthetic turbulence is applied here. Since the application to FSI for nuclear applications has already been discussed in chapter 2, this won't be elaborated upon again. Furthermore, synthetic turbulence models for the purpose of modelling fatigue loading are often derived from existing models, but they are adjusted for the properties of atmospheric boundary layers. It was found that novel methods are often proposed for hybrid RANS/LES, LES inflow conditions, and noise modelling. Thus, the focus will be put on these fields.

4.1.1. Inflow conditions for LES

One of the applications of synthetic turbulence is the creation of inflow conditions for large eddy simulations. In (U)RANS, all variables that are defined on the boundaries are defined as ensemble averages, thus no small scale fluctuations are necessary as input. In LES however, the turbulent scales are resolved up to a certain range, and thus the variables in LES are always stochastically varying up to the resolved scales. This means that these fluctuations also must be represented on the inflow boundary [96]. If only the mean velocities are given at the inflow such as is done in RANS, then that means that the flow must be developed into a turbulent flow, and this can take large lengths before the flow is fully developed. Thus in general, not only mean velocities but also velocity fluctuations are supplied at the inlet, which reduces the development length from inlet to fully turbulent flow.

This is a very active research field, and new methods are still being developed [97]. Several methodologies can be used to generate velocity fluctuations, such as recycling/rescaling methods, precursor simulation methods, or using synthesised turbulence [8, 98]. For this application, synthetic turbulence is only generated on a 2D-plane, however, it does generate turbulence with three components. Typically, if the method includes spatial correlation, this is only done in two dimensions. ST methods that stem from this field will have to be adjusted such that they can generate synthetic turbulence for a full 3D domain. For this application, the main goal of synthetic turbulence is to create a development length as short as possible. Thus, this is often used as a benchmark to compare ST methods. However, this benchmark does not necessarily translate to having physically accurate turbulence. For example, for time correlation a constant convection velocity is often assumed, and the divergence-free criterion is not always respected. This is because the generated turbulence is injected into the computational domain, and in the next steps it will be corrected to adhere to the governing equations. For the application to FSI, this is not the case and thus turbulence adhering to the physical laws is more desired to obtain accurate pressure fluctuations.

4.1.2. Interfaces between RANS and LES

This field is very similar to that of section 4.1.1. Zonal hybrid methods are used when a high fidelity simulation is computationally too expensive, and the flow does not need to be accurately resolved in the whole domain. Thus a RANS or URANS computation is performed over a large part of the domain, while the area that needs to be more resolved is computed via LES. This is illustrated in fig. 4.1.

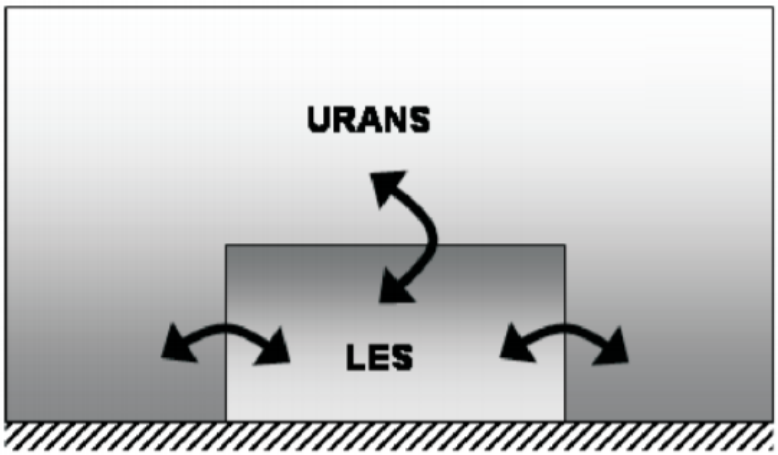

Figure 4.1: Sketch of RANS/LES coupling: embedded LES [8].

Similarly to LES, there is a region in which the turbulence gets fully developed. In zonal methods, this region is resolved by both (U)RANS and LES. The region starts at the inlet of the LES domain, and it ends at the outlet of the (U)RANS domain, as shown in fig. 4.2. Here, synthetic turbulence is introduced at the LES inlet, in order to have a shorter buffer region. Thus in this case, the synthetic turbulence is also generated only for a 2D plane, and it would have to be adjusted to be a fully 3D method. For this application, similar to LES inflow conditions, the shortest buffer region is desired, and this is often used as a benchmark. Often, methods for RANS/LES transition and LES inflow conditions can be used interchangeably.

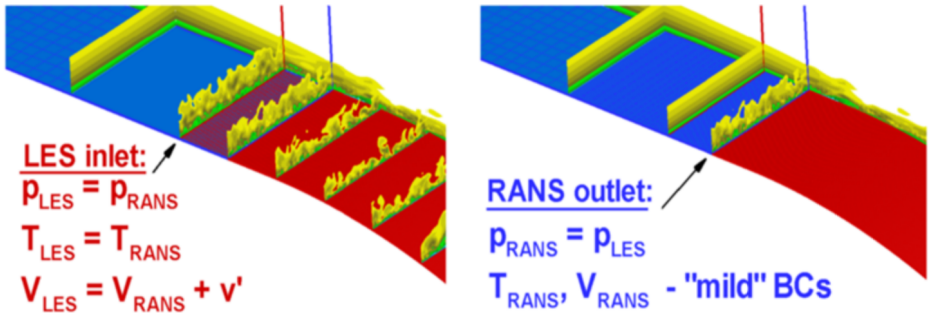

Figure 4.2: The interface between the LES and RANS calculation [9].

4.1.3. Noise Modelling in Computational Aeroacoustics

In Computational AeroAcoustics (CAA), the problem can be divided into the generation of sound and the propagation of sound. Both problems can be solved by using DNS or LES [10], however in this field the computational requirements of LES and DNS are often too large as well. A solution to this is to model the sound sources (i.e. turbulence) and use the linearised Euler equations to propagate this sound. This results in a method that is computationally cheaper than LES or DNS. The turbulence is modelled by synthetic turbulence. In this field, a full three-dimensional turbulence field is constructed, thus ST methods generated for this field can be readily applied to a fuel rod subjected to axial flow. In this field, more attention is paid to the divergence-free criterion, as having a non-divergence-free field can lead to spurious pressure waves, which poses a problem for CAA [99]. Validation is often done directly through noise modelling, thus not all new methods publish the validation of the one and two-point statistics for a simplified flow case, such as turbulent channel flow.

4.2. Current Model of NRG

The current synthetic turbulence model that is implemented in NRG-FSIFOAM is a slightly adjusted version of that described by Kottapalli et al. [14]. The method was adjusted internally at NRG and this method is described below. It is based on a random flow generation method, which will be elaborated upon in section 4.3. In short, it generates an isotropic velocity fluctuation field, based on a modified Von Karman spectrum. This method is also partly based on that of Senthooran [100], which used it to predict the pressure on a high-rise building. The velocity fluctuations are calculated as follows:

$$u'(\mathbf{x},t) = 2\sum_{n}^{N} \tilde{u}_n cos[k_n(\mathbf{x} - t u_{c_n}) + \psi_n + \omega_n t]\sigma_n \tag{4.1}$$

Where $\tilde{u}_n$, ψ_n, ω_n, and σ_n are the amplitude, phase angle, characteristic angular frequency, and the direction of the n^{th} mode with wavevector k_n. u_c is the convective velocity. Note that these quantities are spatially varying. From the incompressible continuity equation, it follows that the velocity fluctuation field must be divergence-free, as shown in eq. (4.2). For the formulation of the velocity fluctuations as given in eq. (4.1), this translates into eq. (4.3), i.e. the wavenumber vector is always perpendicular to the direction vector. Note that this method of ensuring the divergence-free criterion is valid in the infinitesimally small domain, but the criterion is not met exactly due to the discretization of the divergence operator [101]. This will be elaborated upon in section 4.3.4. The angular frequency is calculated with eq. (4.4), and the convection velocity is calculated with eq. (4.5). Note that the convection velocity is calculated for every mode, and that its direction is the unit direction. It is not clear why this choice was made.

$$\nabla \cdot \mathbf{u}' = 0 \tag{4.2}$$

$$k_n \cdot \sigma_n = 0 \tag{4.3}$$

$$\omega_n = (\varepsilon k_n^2)^{1/3} \tag{4.4}$$

$$u_{c_n} = \frac{\omega_n}{k_n}\begin{bmatrix}1 & 1 & 1\end{bmatrix}/\sqrt{3} \tag{4.5}$$

4.2.1. Wavenumber & Direction Calculations

The smallest wavenumber is correspondent to the largest length scale L in the domain, this can be approximated by eq. (4.6), as done in [100]. The current method implemented by NRG is more conservative, and the smallest wavenumber is calculated by eq. (4.7), which was based on dimensional analysis. It was found that this is necessary to fully capture the turbulent spectrum and eq. (4.6) would lead to clipping the spectrum such that energy-containing eddies are neglected.

$$k_{eddy} = \frac{2\pi}{L} = \frac{2\pi\varepsilon}{K^{3/2}} \tag{4.6}$$

$$k_{eddy} = \frac{\varepsilon}{max(||\mathbf{u}||^3)} \tag{4.7}$$

Given the wavenumber space from k_{eddy} to k_η, the edge-wavenumbers are logarithmically distributed as shown in eq. (4.8), where γ is defined in eq. (4.9). Then the wavenumbers are defined as $k_n = \tilde{k}_{n+1/2}$. From fig. 4.3, the relation between the magnitude of the wavenumber and the wave vector can be established, shown in eq. (4.10).

$$\tilde{k}_i = k_{eddy} \cdot e^{\gamma i} \tag{4.8}$$

$$\gamma = \frac{log(k_\eta / k_{eddy})}{N} \tag{4.9}$$

$$\mathbf{k_n} = k_n[\sin\theta_n \cos\psi_n, \sin\theta_n \sin\psi_n, \cos\theta_n]^T \tag{4.10}$$

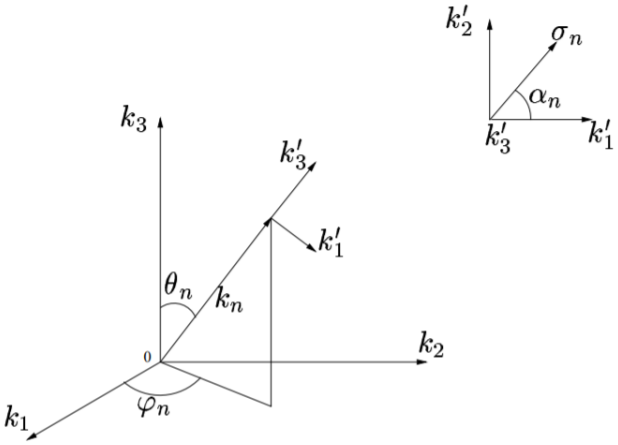

Figure 4.3: Wave vector geometry of the n^{th} Fourier mode [10].

In order to satisfy the divergence criterion, the direction vector must be orthogonal to the wavevector. Senthooran [100] accomplished this by assuming that σ_n lies in a plane perpendicular to $\mathbf{k_n}$. From this, eq. (4.11) is found. All the angle definitions are defined in fig. 4.3.

$$\sigma_n = \begin{bmatrix} \cos\alpha_n \cos\phi_n - \cos\theta_n \sin\phi_n \sin\alpha_n \\ \cos\alpha_n \sin\phi_n + \cos\theta_n \cos\phi_n \sin\alpha_n \\ \sin\theta_n \sin\alpha_n \end{bmatrix} \tag{4.11}$$

The velocity fluctuations are stochastic due to the randomness introduced by the phase angle, as well as the angles related to the direction of the wavenumber vector. Namely, ϕ_n, ψ_n and θ_n are randomly generated. Kottapalli et al. [14] generated only one random variable, which was scaled to represent the other random variables. Doing this gives a correlation to the random variables, which is not desired. The current method implemented in NRG-FSIFOAM generates three independent random variables. Furthermore, Kottapalli et al. [14] generated a random variable for each spatial location, but this gives uncorrelated spatial noise. For this reason, the random variables in the current implementation are created for each wavenumber mode once per timestep. To ensure isotropic turbulence, the following probability functions are used:

$$P(\psi_n) = \frac{1}{\pi}, \qquad P(\phi_n) = \frac{1}{2\pi}, \qquad P(\theta_n) = \frac{1}{2} sin(\theta_n) \tag{4.12}$$

4.2.2. Turbulent Kinetic Energy Spectrum

The velocity fluctuations must be in agreeance with the available data from (U)RANS. This is done by relating the turbulent kinetic energy K and the dissipation rate ε to the velocity fluctuations through the energy spectrum [92], as shown in eq. (4.13) and eq. (4.14).

$$\int_0^\infty E(k)dk = K \tag{4.13}$$

$$2\nu\int_0^\infty k^2 E(k)dk = \varepsilon \tag{4.14}$$

The modified Von Karman spectrum is used as an expression for the turbulent kinetic energy spectrum, given in eq. (4.15). Where A is a constant depending on the turbulent kinetic energy, k_{max} is the wavenumber at maximal turbulent kinetic energy, and k_η is the highest wavenumber i.e. the wavenumber corresponding to the Kolmogorov scale. Only k_{max} and A are unknowns, as they are used to scale the spectrum to the appropriate quantities. They can be found by using the constraints displayed in eq. (4.13) and eq. (4.14).

$$E(k) = A\frac{2K}{3k_{max}}\frac{(k/k_{max})^4}{[1+(k/k_{max})^2]^{(17/6)}}exp(-2(\frac{k}{k_\eta})^2) \tag{4.15}$$

Kottapalli et al. [14] simplifies the method of Senthooran [92] by assuming that the modified Von-Karman spectrum overlaps with the Kolmogorov spectrum for the inertial subrange, showed in eq. (4.16) [52]. Equating this to the energy spectrum and neglecting the exponential term (which is close to unity in the inertial subrange), gives eq. (4.17). Note that this simplification means that eq. (4.14) is not necessarily adhered to, as it is not explicitly imposed as done in Senthooran [92]. The constant A can be determined from eq. (4.13). To simplify the integral, a substitution is made from [100], where $\beta = 2(\frac{k_{max}}{k_\eta})^2$. The result is shown in eq. (4.18). With A and k_{max} known, the modified Von Karman spectrum can be calculated. The integral is evaluated using Simpson's rule, as opposed to the Riemann's sum Kottapalli et al. [14] used to integrate. Note that it is possible for k_{max} to be larger than k_η, however, this is nonphysical and it can lead to numerical instabilities. Thus k_{max} is clipped at $k_\eta/2$. This situation was not encountered often and thus it should have no large effects on the results.

$$E(k) = A\varepsilon^{2/3}k^{-5/3} \tag{4.16}$$

$$k_{max} = \varepsilon(\frac{3}{2K})^{3/2} \tag{4.17}$$

$$A = 3\left[\int_0^1 \frac{\eta^{3/2}}{(1-\eta)^{2/3}}exp(-\beta\frac{\eta}{1-\eta})\right]^{-1}d\eta \tag{4.18}$$

The amplitudes of the velocity fluctuations are directly related to the turbulent kinetic energy. $K = \frac{1}{2}||u'||^2$, which can be related to the magnitudes of each mode. The method of Senthooran [100] is used (eq. (4.19)), where the integral of the turbulent kinetic energy spectrum is approximated using a Riemann's sum, resulting in eq. (4.20). Thus by definition, the velocity fluctuations adhere to the prescribed turbulent kinetic energy, for $N \to \infty$.

$$\int_0^\infty E(k)dk = \sum_n \tilde{u}_n^2 \tag{4.19}$$

$$\tilde{u}_n = \sqrt{E(k_n)\Delta k_n} \tag{4.20}$$

4.2.3. Pressure Fluctuations

With the model for the velocity fluctuations completely defined, and the URANS inputs, the pressure fluctuations can be calculated, by solving the partial differential equation eq. (3.31). In the PFM by NRG, this equation is slightly adjusted, with the assumption that eq. (4.2) holds. In fact, eq. (4.21) is solved. By applying the chain rule to the first two right-hand-side terms of eq. (4.21), and using eq. (4.2) and the continuity equation for incompressible flow, eq. (3.31) can be reconstructed. Thus, the divergence criterion is of key importance to eq. (4.21), and must be exactly enforced for this equation to be correct.

$$\frac{\partial^2 p'}{\partial x_i \partial x_i} = -\rho\left[\frac{\partial^2}{\partial x_i \partial x_j}\left(\overline{u}_i u'_j + u'_i\overline{u}_j + u'_i u'_j - \overline{u'_i u'_j}\right)\right] \tag{4.21}$$

For the calculations of the pressure fluctuations, the spatial mean is subtracted from the right-hand side of eq. (4.21). This is done because if the spatial mean is not equal to zero, the solution is dominated by a three-dimensional parabola. This can be shown for a simplified Poisson equation in one dimension, where

the right-hand side is decomposed in the spatial mean, and the spatial fluctuating component, as shown in eq. (4.22). The solution of this equation is shown in eq. (4.23), and it shows that the spatial mean gives a parabolic solution. Thus, to prevent this solution, the spatial mean of the right-hand side of eq. (4.21) is subtracted before the equation is solved. As can be seen there are still a linear and a constant term in eq. (4.23). These terms are determined by the boundary conditions.

$$\frac{\partial^2 p'}{\partial x^2} = rhs' + \overline{rhs} \tag{4.22}$$

$$p' = \frac{1}{2}\overline{rhs}x^2 + c_1 x + c_2 + \int\int rhs' dx dx \tag{4.23}$$

4.2.4. Remarks

In this section, an elaborate review of the current synthetic turbulence method of NRG is given, which was based on the work of Kottapalli et al. [14] and Senthooran [92, 100]. While it has given initially promising results, there are a few points on which this model can be improved. The main problems are its lack of spatial correlation and the current method of temporal correlation, as well as the assumption of isotropic turbulence. Next to this, other small problems were found as well.

In the current method, it is attempted to achieve temporal correlation by assuming the fluctuations are convected over time. However, the convected velocity of each mode is not in the direction of that mode, but rather in the unit direction. Furthermore, it was found that this method of temporal correlation created convection velocities that were very small relatively to the mean flow velocity [102]. The largest scales have the highest convection velocity, which is in accordance with the theory described in section 3.5. However, even for these scales, the convection velocity is only a fraction of the mean velocity. This also caused unrealistically elongated flow structures that significantly lowered the estimation of the RMS pressure fluctuations. Finally, the temporal decorrelation due to production and dissipation of turbulence is currently not represented by the synthetic turbulence.

Due to how Kottapalli et al. [14] solves for the wavenumber of maximal turbulent energy, it does not necessarily adhere to eq. (4.14). Thus, the dissipation rate obtained from the velocity fluctuations does not have to be the same as the one obtained from (U)RANS data. Finally, the current method assumes isotropic turbulence. The vibrations in fuel rods subjected to axial flow are caused by the at-the-wall turbulence, which is anisotropic. Thus, in order to have an ST model that is applicable to fuel rods in axial flow, it is of importance that the synthetic turbulence can be anisotropic.

4.3. Random Flow Generation

The Random Flow Generation method was first proposed by Kraichnan [103]. This was used as a method for generating homogeneous isotropic turbulence by using random Fourier modes. This was one of the first methods for developing synthetic turbulence and a bulk of the methods today stem from Kraichnan. New models are often a continuation of older models and in this case, three clear trends of continuation can be distinguished. In this section, each trend is explained, and the latest model of this trend is treated in more detail.

4.3.1. Bailly, Senthooran, Kottapalli, and Billson

Bailly & Juve [83] adjusted Kraichnan's method [103] such that time correlation was introduced. This was done by adding the convection and angular frequency terms that are also present in eq. (4.1). Senthooran [100] then slightly adjusted this method and applied it to model pressure fluctuations. In turn Kottapalli et al. [14] adjusted it, which was presented in section 4.2. Billson et al. [10, 82] had also adjusted Bailly & Juve's method, which is presented below.

The generated velocity fluctuations are defined in eq. (4.24), where similar to the method of section 4.2, $k_n \cdot \sigma_n = 0$. Where Senthooran [100] used an expression to relate θ to α, Billson et al. also generate α randomly. Moreover, Billson et al. calculate the amplitudes $\tilde{u}_n$ in the same way as Senthooran [100], using eq. (4.20). The modified Von Karman Spectrum is used to represent the turbulent energy spectrum, however, the constants A and k_{max} are calculated differently. In this method, also the turbulent kinetic energy is used to find A, but with the assumption of high Reynolds number, which results in the analytical expression eq. (4.25), where $\Gamma()$ is the extension of the factorial function. The wavenumber associated with the peak turbulent energy

k_{max} is found by linking the turbulent length scale found by the (U)RANS simulation to that of the velocity fluctuations, resulting in eq. (4.26).

$$\mathbf{u}_t(\mathbf{x}) = \sum_n \tilde{u}_n \cos(\mathbf{k_n x} + \psi_n)\sigma_n \tag{4.24}$$

$$A = \frac{4}{\sqrt{\pi}} \frac{\Gamma(17/6)}{\Gamma(1/3)} \tag{4.25}$$

$$k_{max} = \frac{9\pi}{55} \frac{A}{\Lambda} \tag{4.26}$$

The part where Billson et al. differentiates his method from previous methods, is his method for time correlation and convection. The realised generation of a velocity fluctuation field at timestep m is defined as $\mathbf{u}_t^m(\mathbf{x})$. Each generated field is independent of the others and they have a statistical mean zero in time, i.e. it is white noise. The new velocity fluctuation field can then be defined as in eq. (4.27), where $a = e^{-\Delta t/\tau}$, $b = \sqrt{1-a^2}$ and τ is the time scale. The parameter b ensures that the root mean squared velocity fluctuations of $\mathbf{v}_t^m(\mathbf{x})$ are equal to those of $\mathbf{u}_t^m(\mathbf{x})$. Thus this method creates a temporal correlation by superimposing a random field with the field of the previous timestep. To account for convection, the advection equation is solved for $\mathbf{v}_t^{m-1}(\mathbf{x})$, as shown in eq. (4.28), before it is used in eq. (4.27).

$$\mathbf{v}_t^m(\mathbf{x}) = a\mathbf{v}_t^{m-1}(\mathbf{x}) + b\mathbf{u}_t^m(\mathbf{x}) \tag{4.27}$$

$$\frac{\partial \rho \mathbf{v}_t^{m-1}}{\partial t} + \frac{\partial \rho u_j \mathbf{v}_t^{m-1}}{\partial x_j} = 0 \tag{4.28}$$

The current presented method is applicable to isotropic turbulence, but the same method can be adjusted for anisotropic turbulence. Billson et al. proposed to diagonalise the normalised Reynolds stress as shown in eq. (4.29), where a is the normalised Reynolds stress tensor as defined in eq. (4.30), R is the matrix of eigenvectors of a, $(\rho k)_{avg}$ is the average turbulent kinetic energy, and a^* is the diagonalised stress tensor. This is essentially a transformation to the principal coordinate system. Using this transformation, an isotropic fluctuation field in the principal coordinate system can be transformed to an anisotropic fluctuation field in the spatial coordinate system. In the following equations, the superscripts $*$,a and i refer to the principal coordinate system, anisotropic and isotropic respectively. In order to generate an anisotropic fluctuation field, first the fluctuation field is transformed to the principal coordinate system, by multiplying with R^T. Then the field is made anisotropic by scaling the isotropic field with the anisotropic normalised stress tensor, i.e. multiplying by $a^{*1/2}$. Then, the field is transformed back to the original coordinate system by multiplying with R. This whole string of operations can be done in one go, as shown in eq. (4.31).

$$a^* = R^T a R \tag{4.29}$$

$$a_{ij} = \frac{-3}{2} \frac{\tau_{ij}}{(\rho k)_{avg}} \tag{4.30}$$

$$\begin{aligned} u_t^a = R \cdot a^{*1/2} R^T u_t^i = R \cdot 2 \sum_n \tilde{u}_n \cos(k_n^{*a} x + \psi_n)\sigma_n^{*a} \\ k_n^{*a} = a^{*1/2} R^T k_n \\ \sigma_n^{*a} = a^{*1/2} R^T \sigma_n \end{aligned} \tag{4.31}$$

This method of generating anisotropy reproduces the Reynolds stress tensor that is given as input, thus it corresponds more accurately to the properties of the flow than the method of Senthooran [100] or Kottapalli et al.[14], as these do not take the Reynolds stress into account. One disadvantage of the presented method is that the divergence-free criterion is now met in the principal coordinate system, but this is not translated back to the spatial coordinate system, due to the scaling operation. For homogeneous isotropic flow, the correlation functions showed great agreeance with the analytical solution [10]. The correlation functions had not been compared for anisotropic flow. It was verified however, that the Reynolds stress tensor was indeed correctly represented by the velocity fluctuation field, and a qualitative comparison of the fluctuations with data DNS also gave great agreeance [82]. This method has been used in the field of CAA, as well as for LES inflow conditions [89]. In conclusion, the model proposed by Billson et al. models all the characteristics that were determined in section 3.5, with two small exceptions. Firstly, it uses the assumption of $Re >> 1$ to arrive to an analytical expression for the coefficients of the energy spectrum. Secondly, due to its representation of the inhomogeneous Reynolds stress tensor, the divergence criterion can only approximately be met.

4.3.2. Smirnov, Batten, Yu, and Castro

Smirnov et al.[75] proposed a method for simulating inhomogeneous anisotropic turbulence, based on the method of Kraichnan [103]. This method scales the isotropic velocity fluctuations obtained by Kraichnan's method [103] with a tensor, which is obtained by similarity scaling of the Reynolds stress. The fluctuations are also scaled based on the local time and length scales. Since the Reynolds stress and the time and length scales vary in space, the method is implicitly inhomogeneous. Smirnov et al.'s method uses a Gaussian energy spectrum as opposed to the modified Von Karman Spectrum. This choice has been shown to give unrealistic results for applications such as atmospheric boundary layers [97]. Another disadvantage of this method is that the divergence criterion is only met for homogeneous turbulence. The varying scaling causes the divergence criterion not to be met, although Smirnov et al. did show that it is approximately met when the Reynolds stress is slowly varying in space [75]. Lastly, Smirnov et al.'s method does not account for the convection of turbulence. This method has been implemented for LES inflow conditions in ANSYS Fluent [104].

Batten et al.[87] simplified this method by using Cholesky decomposition instead of using similarity transformations. Huang et al. [105] modified Smirnov's method such that any spectrum model could be used. Castro [72] later adjusted this method with an improvement of the temporal correlations, this method is elaborated upon.

Castro defined the velocity fluctuations as shown in eq. (4.32). Here $\tilde{k}$ and $\tilde{x}$ are the non-dimensionalised wavenumber and position, respectively. The wavenumber is non-dimensionalised by the lowest wavenumber of the spectrum, and x by the turbulent length scales. τ_0 is not the turbulent time scale, but rather an ad-hoc parameter that must be set by the user. This method does not use a 1D energy spectrum, but instead it assumes that the 1D spectrum is equal to the weighted sum of the energy spectra along each principal axis. The factors $p_i^{m,n}$ and $q_i^{m,n}$ align the energy spectrum according to the diagonal of the Reynolds stress tensor. Namely, the velocity fluctuations must obey the constraint given in eq. (4.33). From this, the scaling factor c_i is determined. E_i is the turbulent energy spectrum of direction i. The factors $p_i^{m,n}$ and $q_i^{m,n}$ are then calculated using eq. (4.34) and eq. (4.35), respectively. Here, $r_i^{(m,n)}$ is a random variable with a distribution $N(0,1)$. From this, the wavenumber vectors can be calculated as to satisfy the divergence criterion, shown in eq. (4.36) and eq. (4.37).

$$u_i(\mathbf{x},t) = \sum_m \sum_n \left[p_i^{m,n} \cos(\tilde{k}_j^{m,n} \tilde{x}_j + \omega_{m,n} \frac{t}{\tau_0}) + q_i^{m,n} \sin(\tilde{k}_j^{m,n} \tilde{x}_j + \omega_{m,n} \frac{t}{\tau_0}) \right] \tag{4.32}$$

$$u_{rms,i}'^2 = c_i \int_0^\infty E_i(k)\,dk \tag{4.33}$$

$$p_i^{(m,n)} = \frac{r_i^{(m,n)}}{||r_i^{(m,n)}||} \sqrt{\frac{4c_i}{N} E_i(k_m) \Delta k_m \frac{r_i^{(m,n)}}{1+r_i^{(m,n)}}} \tag{4.34}$$

$$q_i^{(m,n)} = \frac{r_i^{(m,n)}}{||r_i^{(m,n)}||} \sqrt{\frac{4c_i}{N} E_i(k_m) \Delta k_m \frac{1}{1+r_i^{(m,n)}}} \tag{4.35}$$

$$\mathbf{k}^{(m,n)} \cdot \mathbf{p}^{(m,n)} = 0 \tag{4.36}$$

$$\mathbf{k}^{(m,n)} \cdot \mathbf{q}^{(m,n)} = 0 \tag{4.37}$$

Advantages of this method over previous methods is that it provides a divergence-free inhomogeneous anisotropic field, and it is a highly parallel method, as the general procedure is independent for each point. Furthermore, it shows great temporal and spatial correlation compared to analytical results, and the energy spectrum is free of choice, meaning that more accurate spectra than a Gaussian spectrum can be used. However, the anisotropy of this method is only related to the diagonal of the Reynolds stress tensor, meaning that the off-diagonal components are not necessarily accurately represented. Next to this, the method has several ad-hoc parameters that need to be tuned to get the most accurate result.

4.3.3. Adamian and Shur

Adamian et al. [91] developed a new RFG method that took inspiration from several older models [75, 84, 87, 103]. It is a quite simple algorithm that uses a lot of ad-hoc parameters. Nevertheless, when applied to LES inflow conditions, it saw a considerably shorter development length compared to other models [91]. Later, this model was improved by Shur et al. [9], by adding time correlation.

The velocity fluctuations are defined such that the second moment tensor is equal to the Reynolds stress obtained from the (U)RANS simulation, by using Cholesky decomposition, $r_{ij} = a^T a$, where a is defined

in eq. (4.38). Then the velocity fluctuations are defined as $u'_i(r,t) = a_{ij}v'_j(r,t)$, where $v'_j(r,t)$ is defined in eq. (4.39). Here q^n is the normalised amplitude of mode n, k^n is the amplitude of the wavevector of mode n, d^n is a random unit vector uniformly distributed over a sphere, σ^n is the direction vector, which is orthogonal to d^n [103]. The angle determining the plane in which σ^n lies is a random variable with $P(2\pi)$. ϕ^n is the phase angle which is also a random variable with $P(2\pi)$. Unique to this method is that the random variables are only defined once.

$$a_{ij} = \begin{bmatrix} \sqrt{r_{11}} & 0 & 0 \\ r_{21}/a_{11} & \sqrt{r_{22}-a_{21}^2} & 0 \\ r_{31}/a_{11} & (r_{32}-a_{21}a_{31})/a_{22} & \sqrt{r_{33}-a_{31}^2-a_{32}^2} \end{bmatrix} \tag{4.38}$$

$$\mathbf{v}'(r,t) = \sqrt{6}\sum_n \sqrt{q^n}\left[\sigma^n \cos(k^n \mathbf{d^n}\cdot\mathbf{r}' + \phi^n)\right] \tag{4.39}$$

$$q^n = \frac{E(k^n)\Delta k^n}{\sum_n E(k^n)\Delta k^n} \tag{4.40}$$

The turbulence is propagated in time by assuming Taylor's Hypothesis [106], i.e. the turbulence is convected with a constant velocity equal to the mean flow. Shur et al. assumed that the flow would be in the x-direction, and defined the position vector as in eq. (4.42). Here l_e is the length of the eddy with the largest turbulent kinetic energy. This determined by eq. (4.41), where d_w is the wall distance, $C_l = 3.0$ and l_t is the turbulent length scale as obtained from (U)RANS.

$$min(2d_w, C_l l_t) \tag{4.41}$$

$$r = \left[\frac{2\pi}{k^n max(l_e(\mathbf{r}))}(x - U_0 t) \quad y \quad z\right] \tag{4.42}$$

Shur et al. [9] uses a modified version of the Von Karman Spectrum. An advantage of this method is that the height of the spectrum is not important, as the amplitudes are normalised. Thus no computations as eq. (4.18) or eq. (4.25) are necessary. The spectrum is displayed in eq. (4.43), where f_{cut} damps the spectrum at wavenumbers larger than the Nyquist value. This function is only applicable for LES inflow or LES/RANS transition conditions. The function is shown in eq. (4.44), where $k_{cut} = 2\pi/l_{cut}$ and l_{cut} is defined as in eq. (4.45). Note that the definition in eq. (4.43) is slightly different than eq. (4.15), namely there is an additional factor 2.4 in the denominator and an additional factor 12 in the exponent term. It is not clear where these discrepancies come from. For the wavenumbers, Shur et al. [9] use a geometric series rather than a uniform or logarithmic one.

$$E(k) = \frac{(k/k_{max})^4}{[1+2.4(k/k_{max})^2]^{(17/6)}} exp(-(12\frac{k}{k_\eta})^2) f_{cut} \tag{4.43}$$

$$f_{cut} = exp\left(-\left[\frac{4max(k-0.9k_{cut},0)}{k_{cut}}\right]^3\right) \tag{4.44}$$

$$l_{cut} = 2min\{[max(h_y,h_z,0.3h_{max}) + 0.1d_w], h_{max}\} \tag{4.45}$$

Regarding the generation of velocity fluctuations, Shur et al. [9] only showed qualitative verification by comparing the generated fluctuation fields with those of LES data of a turbulent channel flow. It does not compare any statistics for this generated field. However, it does compare statistics of an LES simulation using the described method as inflow condition for the velocity fluctuations at various distances from the inlet. This shows a quick recovery of the skin friction coefficient, as well as the Reynolds stresses. It is unclear however, how this translates to the validity of the synthetic turbulence model, and if a shorter recovery length is related to the accuracy of the synthetic turbulence model. The model presented by Shur et al. is simple and very easy to implement. However, for the time correlation, Shur et al. assumed a constant convection velocity for all of the turbulence, specifically in 1 direction only. Moreover, there are several ad-hoc parameters, which are used for calculating the wavenumber of the eddies that contain the largest energy, as well as the cut-off wavenumber. Next to this, there are discrepancies in the energy spectrum compared to other models such as Kottapalli et al. [14] or Billson et al. [10]. The method shows promising results for the application to the inflow conditions of LES or DNS, and it has been used several times for this application [107, 108]. For LES

inflow conditions, the time correlation is not as important as for the application to CAA or FSI, which is an explanation for the current method of time correlation that Shur has implemented. Combining this method with the time correlation steps of Billson et al. [10] could give a method that is more suitable for CAA and FSI. Given the successful results of its current application, the method adjusted for FSI is an attractive option for the modelling of nuclear fuel rods subjected to axial flow.

4.3.4. A Note On The Divergence Criterion

In the shown Random Flow Generation methods, the constraint $k_n \cdot \sigma_n = 0$ is always adhered to in order to preserve a solenoidal field in the case of homogeneous turbulence. This relation was proved by Kraichnan [103] in his original method. With the velocity fluctuations given by eq. (4.24), the divergence can be written as in eq. (4.46).

$$\nabla \cdot \mathbf{u} = -2 \sum_n \hat{u}_n k_n \cdot \sigma_n \sin(k_n \cdot x + \psi_n) \sigma_n \tag{4.46}$$

Thus, by satisfying $k_n \cdot \sigma_n = 0$, the divergence is equal to zero, for the case of the exact divergence. However, Saad et al. [101] showed that the discrete divergence is not necessarily zero if the condition of $k_n \cdot \sigma_n = 0$ is met. Rather, the condition $\tilde{k}_n \cdot \sigma_n = 0$ should be met, where $\tilde{k}_n$ is the modified wavenumber vector, for which the modification depends on the discretization scheme. The modified wavenumber vector is equal to the original wavenumber vector in the limit of the grid spacing approaching zero.

For homogeneous isotropic turbulence, the modified wavenumber vector can be determined exactly. This vector gives a zero discrete divergence. As an example, the modified wavenumber vector is derived for the central difference scheme, as shown as in eq. (4.47), where the subscript d denotes a discrete operator.

$$\left.\frac{\partial u}{\partial x}\right|_d = \frac{u(x+\Delta x) - u(x-\Delta x)}{2\Delta x} \tag{4.47}$$

Since the turbulence is homogeneous, eq. (4.48) holds in this case. Next to this, one can use the trigonometric identity $\cos(x+\Delta x) - \cos(x-\Delta x) = -2\sin(x)\sin(\Delta x)$ to combine eq. (4.47) and eq. (4.48). From this, it is found that for this case, the modified wavenumber is equal to $\tilde{k}_n = \sin(k_n \Delta x)/(\Delta x)$. By evaluating its limit, it can be found that it approaches k_n for $\Delta x \to 0$. While the modified wavenumber vector can be calculated for homogeneous flows, this is not generally the case. Thus, while the exact divergence is zero, the discrete divergence is not. In future remarks, the divergence criterion refers to the exact divergence. Thus even though a method is classified as "divergence-free", the discrete divergence may be non-zero.

$$\boldsymbol{u}(\boldsymbol{x} + \Delta \boldsymbol{x}, t) = 2 \sum_n^N \tilde{u}_n cos[k_n(\mathbf{x} + \Delta \boldsymbol{x}) + \psi_n] \sigma_n \tag{4.48}$$

Methods that are capable of representing anisotropic turbulence, typically used a scaling and transformation method similar to that of Smirnov et al. [75]. Using this scaling and transformation method does not violate the exact divergence-free criterion, in the case that the flow is homogeneous. The scaling operation of the velocity fluctuation is shown in eq. (4.49), from this the divergence can be derived, which results in eq. (4.50). In both equations, c_i is the scaling vector, which is based on the local Reynolds stress tensor. As can be seen, for the divergence criterion to be met, the scaling tensor can not have any spatial variation, i.e., for homogeneous flows the scaling does not violate the divergence-free criterion. However, if the Reynolds stresses vary in space, the divergence is not equal to zero. It can be said that the divergence is approximately zero for spatially slowly varying Reynolds stress, which is often the case for (U)RANS simulations [75]. Unlike the scaling operation, the transformation tensor does not violate the divergence criterion.

$$w_i = c_i u_i \tag{4.49}$$

$$\frac{\partial w_i}{\partial x_i} = \frac{\partial c_i}{\partial x_i} u_i + c_i \frac{\partial u_i}{\partial x_i} \tag{4.50}$$

4.4. Digital Filtering Method

The digital filtering method was first proposed by Klein et al. [109]. In this method, the velocity fluctuations are represented by filtering random fluctuations such that prescribed time and space correlations are imposed. Di mare [76] adjusted the method such that any correlation function shape could be used, however,

this proposed method did not have a unique solution and only for a few cases an explicit expression for the filters could be derived [97]. Fathali et al. [110] proposed a similar method, based on random fields rather than filtered random noise. Klein's method was later adjusted by Xie & Castro [111], which used exponential functions to determine the correlations, rather than Gaussian functions. Furthermore, it adjusted the method to be more computationally efficient, by using 2D slices and providing a time correlation between them, rather than generating a 3D filtered velocity field. Kim et al. [80] adjusted Xie & Castro's method by making it divergence-free. In this section, the method of Xie & Castro, as well as the adjustments by Kim et al. are reviewed.

Similar to several other methods, the Reynolds stress tensor is imposed on the velocity fluctuations by use of Cholesky decomposition, shown in eq. (4.51), where a_{ij} is defined in eq. (4.38). The digital filter is applied to an "intermediate" velocity field ψ in eq. (4.52), where the subscript m denotes the mth mesh cells, r_{m+j} is a random variable from $N(0,1)$, and b_j is the jth filter coefficient. Xie & Castro assumed an exponential correlation function, from this eq. (4.53) was derived, where b'_j is given by eq. (4.54). Note that b'_j is only approximately calculated [111]. The variable N is defined by $N = \frac{2I}{\Delta x}$, where I is the integral length scale. With this definition, the filter is able to capture twice the desired length scale, which ensures sufficient filtering at a moderate cost [112]. The length scale is assumed to be constant, likewise, Δx is assumed to be constant i.e. the method is designed for a uniform Cartesian grid.

$$u'_i = a_{ij} u^*_j \tag{4.51}$$

$$\psi_m = \sum_{j=-N}^{N} b_j r_{m+j} \tag{4.52}$$

$$b_j = \frac{b'_j}{(\sum_{k=-N}^{N} b'^2_k)^{1/2}} \tag{4.53}$$

$$b'_j \approx exp\left(-\frac{\pi|j|}{2n}\right) \tag{4.54}$$

Applying 1 filter gives a 1D correlated velocity field, for a 2D correlated velocity field, a random variable has to be filtered twice, shown in eq. (4.55). For the application to an LES inflow condition, only a two-dimensional field is necessary. However, for the application to CAA and FSI, a fully 3D correlated velocity field is necessary, and thus a random variable has to be filtered three times. This gives a quite high computational cost compared to RFG methods [97]. To achieve time correlation, a similar method to Billson et al. [10] is used. In eq. (4.56), the relation for the velocity fluctuations (before the Cholesky correction) at time $(t + dt)$ is given. At each moment in time, a new field is created corresponding to eq. (4.55) or its 3D version, which is then correlated with the previous solution by means of an exponentially decaying function. Here $C_x = \frac{\pi}{4}$ is a model constant, and T is the turbulent time scale, based on the mean flow velocity and the integral length scale.

$$\psi_{m,l} = \sum_{j=-N}^{N} \sum_{k=-N}^{N} b_j b_k r_{m+j,l+k} \tag{4.55}$$

$$u^*_i(t+dt) = u^*_i(t) exp\left(-\frac{C_x \Delta t}{T}\right) + \psi_i \left[1 - exp\left(-\frac{C_x \Delta t}{T}\right)\right]^{1/2} \tag{4.56}$$

The above method gives a synthetic turbulence field with prescribed Reynolds stresses, as well as spatial and temporal correlation. However, while the mean of the velocity fluctuations is modelled to be zero, this is not always the case when the method is applied. This is because a finite number of random variables is used, and thus the mean may not always be zero. For the application to inflow conditions, these small differences in mass flux can give large changes in pressure, thus Kim et al. [80] proposed a simple method to correct the mass flux difference. The velocity is corrected by multiplying the obtained velocity field from Xie & Castro's method with the prescribed bulk velocity divided by the generated bulk velocity, as shown in eq. (4.57), the generated bulk velocity is defined as the integrated generated velocity field divided by the area, shown in eq. (4.58).

$$u_i = \frac{U_b}{U_{b,T}} u_{i,T} \tag{4.57}$$

$$U_{b,T} = \frac{\int_S u_{n,T} dS}{S} \tag{4.58}$$

Another flaw of the method presented by Xie & Castro, is that it is not divergence-free. Kim et al. [80] also proposed a method which through a predictor-corrector method would make the generated velocity field by Xie & Castro's method approximately divergence-free. This method is only valid for incompressible flow, and it is incorporated in the PISO algorithm [113]. With this method, the turbulence is not injected directly at the inlet, but rather at 1 boundary length away from the inlet. The PISO algorithm is as follows, consider the semi-discretised momentum equation for incompressible flow at node P shown in eq. (4.59). Here, the subscript l denotes the neighbours that are used for the discretisation scheme, the superscript n indicates the time level, A denotes discretisation matrices, which are dependent on the chosen discretisation scheme, and Q_i contains the known values such as the boundary conditions and the values of the previous timestep. The equation can be rewritten in the form of eq. (4.60), where $\tilde{u}_{i,P}^{n+1} = Q_i - \frac{\sum_l A_l u_{i,l}^{n+1}}{A_p}$. In subsequent equations, $\tilde{u}$ is defined similarly, but without the term Q_i. By applying the divergence operator to eq. (4.60), a form of the mass conservation equation is obtained (eq. (4.61)).

$$A_P u_{i,P}^{n+1} + \sum_l A_l u_{i,l}^{n+1} = -\left(\frac{\partial p^{n+1}}{\partial x_i}\right)_p + Q_i \tag{4.59}$$

$$u_{i,P}^{n+1} = \tilde{u}_{i,P}^{n+1} - \frac{1}{A_p}\left(\frac{\partial p^{n+1}}{\partial x_i}\right)_P \tag{4.60}$$

$$\frac{\partial}{\partial x_i}\left[\frac{1}{A_p}\left(\frac{\partial p^{n+1}}{\partial x_i}\right)_P\right]_p = \frac{\partial}{\partial x_i}\left[u_{i,P}^{n+1}\right] \tag{4.61}$$

With the PISO algorithm, this is solved by first guessing the pressure, from that the velocities are calculated, and then the guessed quantities are corrected. The corrector step is usually done twice. The guess of the pressure is that of the previous timestep, from which the predictor velocity is calculated, which can be seen in eq. (4.62). Kim et al. [80] adjust the PISO algorithm such that it takes the velocity fluctuations into account at the injection plane. The predictor step is kept the same as in the PISO algorithm, but in the corrector steps, the generated turbulence is added to the velocity. This is shown in eq. (4.63) and eq. (4.64), where the superscript g indicates that the generated turbulence is added. The corrector steps are repeated and lead to $u_{i,P}^{***}$ and $p_{i,P}^{**}$, where $u_{i,P}^{***}$ is now divergence-free.

$$u_{i,P}^{*} = \tilde{u}_{i,P}^{*} - \frac{1}{A_p}\left(\frac{\partial p^{n}}{\partial x_i}\right)_P \tag{4.62}$$

$$\frac{\partial}{\partial x_i}\left[\frac{1}{A_p}\left(\frac{\partial p^{*}}{\partial x_i}\right)_P\right]_p = \frac{\partial}{\partial x_i}\left[\tilde{u}_{i,P}^{g,*}\right] \tag{4.63}$$

$$u_{i,P}^{**} = \tilde{u}_{i,P}^{g,*} - \frac{1}{A_p}\left(\frac{\partial p^{*}}{\partial x_i}\right)_P \tag{4.64}$$

With this method, Kim et al. [80] create divergence-free inhomogeneous anisotropic synthetic turbulence. Note that while the method of making the synthetic turbulence divergence-free by Kim et al. was applied to Xie & Castro's method [111], it is also possible to apply this to other ST methods. The step of making the generated turbulence divergence-free does not need extra computational power, as the step is integrated into the PISO algorithm. However, as the generated velocity fluctuations are corrected, they do not exactly fulfil the prescribed inputs anymore. I.e. the Reynolds stress and the prescribed spatial correlations are not met exactly anymore. As mentioned earlier, the method is designed for uniform Cartesian grids. The fluctuations can first be generated on such a grid and then interpolated on any non-uniform unstructured grid, however, this leads to extra computations such as grid generation and interpolation, and it is computationally not very feasible to apply this to industry problems. For the application to FSI, it is necessary to create a 3D field of velocity fluctuations, for the presented method the computational costs will then be in the order of $\mathcal{O}(N^3)$, and generally this is computationally expensive [97]. Another problem of the proposed method is that it uses a constant value for the integral length scale, whereas the integral length scale typically varies. Dietzel et al. [112] found that this method mainly produces large scale structures, and thus the energy spectrum is not properly represented due to the lack of small scales. Furthermore, it was found that the prescribed correlation functions did not agree with experimental data of homogeneous isotropic turbulence [112], whereas the RFG method by Billson et al. [10] did. This in turn also results in an energy spectrum that is less accurate. The Digital Filtering method does not seem to provide a more accurate method to generate synthetic turbulence.

However, the method proposed by Kim et al. [80] to make the synthetic turbulence divergence-free shows promise, and it could be applied to other ST methods. It is unclear whether the improvement of a divergence-free field outweighs the fact that the prescribed inputs such as the Reynolds stress are not completely met.

4.5. Random Particle Mesh Method

The random particle method, which was first proposed by Ewert [114], is closely related to the Digital Filtering methods. It is also based on taking a random variable and through filtering obtaining a correlated velocity field. The method first could only be used with a Gaussian filter, which in turn gave a Gaussian energy spectrum. However, several methods have been developed such that a specific energy spectrum can be used, at a price of extra computational costs [115, 116]. With the formulation of Ewert et al. [85], the Reynolds stress tensor could also be adhered to. This method was first developed for CAA purposes, but it has also been applied in other cases. Recently, the RPM method has been applied to study pressure fluctuations at walls [117, 118]. In this section, the method as applied in Hu et al. [117] is elaborated upon, as well as the method proposed by Wohlbrandt et al. [116] to model energy spectra other than a Gaussian one.

The Random Particle method has seen most of its applications to 2D CAA simulations, however, the method could be easily extended to 3D, such as Hu et al. [117] did. The stream function is represented by a filtered stochastic field, of which then the cross product is taken to obtain the velocity, thereby guaranteeing a divergence-free velocity field (in the case of homogeneous turbulence). This is shown in eq. (4.65), where $\hat{a}_{ik}$ is a scaling tensor in order to comply with an input Reynolds stress, G is a three-dimensional filter function, and the cross product is implicitly stated by $\epsilon_{klm}\frac{\partial}{\partial x_l}$, where ϵ_{klm} is the Levi-Civita symbol. The white noise U_i has to fulfil the properties given in eq. (4.66) and eq. (4.67). Equation (4.67) states that the white noise is convected with the local mean flow velocity, given by the term $\delta(\mathbf{r}-\mathbf{u}\tau)$, where δ is the Dirac delta function. The exponential term is introduced to model the temporal decay of turbulence, where τ_s is the local time scale.

$$u_i(\mathbf{x},t)' = \hat{a}_{ik}(\mathbf{x})\int_{V_s}\epsilon_{klm}\frac{\partial}{\partial x_l}G(\mathbf{x}-\mathbf{x}')U_i(\mathbf{x}',t)d\mathbf{x}' \tag{4.65}$$

$$\langle U_i(\mathbf{x}',t)\rangle = 0 \tag{4.66}$$

$$\langle U_i(\mathbf{x}',t)U_j(\mathbf{x}'+\mathbf{r},t+\tau)\rangle = \delta(\mathbf{r}-\mathbf{u}\tau)exp(-\frac{\tau}{\tau_s})\delta_{ij} \tag{4.67}$$

Due to the fact that a Gaussian filter is used, the filter can be done independently in each direction, thus the three-dimensional filter is as shown in eq. (4.68), with the one-dimensional filter being defined in eq. (4.69), where l is the turbulent length scale. Hu et al. [117] used a stretching factor for the length scales not in the wall-normal direction, $l_1 = \gamma l_2 = \gamma l_3$. The relation $l_s = (l_1 l_2 l_3)^{1/3}$ was assumed [57], which gives $l_2 = l_3 = ls\gamma^{-1/3}$. The turbulent length scale l_s can be determined from (U)RANS data with eq. (4.70), with $c_l = 0.09$ and $C_\mu = 0.54$. The turbulent time scale can be determined with eq. (4.71), where $c_\tau = 1.2$ was found from experiments [117]. Finally, the scaling tensor $\hat{a}_{ik} = a_{ik}/c_{(k)}$, where a_{ik} is the Cholesky decomposition, earlier given in eq. (4.38), and $c_{(k)}$ is given in eq. (4.72) through eq. (4.74).

$$G(\mathbf{x}-\mathbf{x}') = g(x_1-x_1',l_1)g(x_2-x_2',l_2)g(x_3-x_3',l_3) \tag{4.68}$$

$$g(y,l) = exp\left(\frac{-\pi y^2}{2l^2}\right) \tag{4.69}$$

$$l_s = \frac{c_l\sqrt{k_t}}{C_\mu\omega} \tag{4.70}$$

$$\tau_s = \frac{c_\tau l_s}{\sqrt{k_t}} \tag{4.71}$$

$$c_{(1)} = \sqrt{\pi l_s}\gamma^{1/3} \tag{4.72}$$

$$c_{(2)} = \sqrt{\frac{\pi l_s}{2}}\frac{\sqrt{1+\gamma^2}}{\gamma^{2/3}} \tag{4.73}$$

$$c_{(3)} = c_{(2)} \tag{4.74}$$

The domain is divided into equally sized control volumes V_p, where a particle x_p is assigned to the centre of each volume. These particles move with their respective local convective velocities. Each particle is

associated with a random variate r_{ip}, which is related to U_i through eq. (4.75). While U_i is used to describe the theory, in practice the random variate r_{ip} is generated directly, through eq. (4.76), where σ_{ip}^n is a random variate with $N(0,1)$. From this, the discretised form of eq. (4.65) can be solved, denoted in eq. (4.77). Here, the position of the particle $\mathbf{x}_p$ is adjusted every time step based on the local mean flow velocity.

$$r_{ip}^{n+1} = \int_{V_p} U_i(\mathbf{x}', t^{n+1}) d\mathbf{x}' \tag{4.75}$$

$$r_{ip}^{n+1} = \left(1 - \frac{\Delta t}{\tau_s}\right) r_{ip}^n + \left(\frac{2V_p \Delta t}{\tau_s}\right)^{1/2} \sigma_{ip}^n \tag{4.76}$$

$$u_i^{n+1}(\mathbf{x}) = \sum_p \hat{a}_{ik} \epsilon_{klm} \frac{\partial}{\partial x_l} G(\mathbf{x} - \mathbf{x}_p) r_{mp}^{n+1} \tag{4.77}$$

This concludes the numerical method that Hu et al. [117] used for modelling wall pressure fluctuations. In the above method, Hu et al. [117] use a Gaussian correlation function, which leads to a Gaussian energy spectrum. To be able to model more realistic energy spectra, Wohlbrandt et al. [116] proposed a method that uses a sum of weighted Gaussian spectra. Each Gaussian spectrum is multiplied by $f(l_j)\Delta l_j \hat{A}_j$ as shown in eq. (4.78), where $f(l_j)$ is a weighting function specific to the desired energy spectrum, and $\hat{A}_j$ is the amplitude associated with the Gaussian spectrum with length scale l_j. An exponential distribution is used for the length scales, given in eq. (4.79), where l_0 and l_M are user-defined minimum and maximum length scales. Wohlbrandt et al. [116] derived the weighting function $f(l_m)$ for the von Kárman, Liepmann, and the modified Von Kárman spectrum. It was found that 10 weighted Gaussian spectra were needed to accurately represent the modified Von Kárman spectrum.

$$u_i^{n+1}(\mathbf{x}) = \hat{a}_{ik} \epsilon_{klm} \frac{\partial}{\partial x_l} \sum_j f(l_j) \Delta l_j \hat{A}_j \sum_p G(\mathbf{x} - \mathbf{x}_p) r_{mp}^{n+1} \tag{4.78}$$

$$l_m = l_0 \left(\frac{l_M}{l_0}\right)^{m/M} \tag{4.79}$$

$$\hat{A}_m = \sqrt{\frac{\rho_0 2 k_t}{3\pi l_m}} \tag{4.80}$$

While the theory behind this method is complex, the algorithm is easy to implement. For homogeneous turbulence, this method is divergence-free. However, similar to other methods [9, 10, 75, 119], the method is only approximately divergence-free for inhomogeneous turbulence, assuming slowly spatially varying turbulence characteristics. An advantage of this method is that it uses the local length scales and turbulent kinetic energy, making the method suitable for highly non-uniform mean flow fields. Furthermore, it takes into account the convection of the turbulence and the time decorrelation due to dissipation. Sadly, the method contains several ad hoc parameters such as γ and c_τ. The method has shown accurate results in 2D and 3D applications [85, 117, 118], however the method is computationally very expensive. Hu et al. [118] simulated 3 wall patches of the Airbus-A320. Each patch was limited to 3, 1.05, and 2.5 boundary layer lengths for 1-point statistics with a mesh size of $128 \times 64 \times 128$, and 12, 3 and 4 boundary layer lengths for 2-point statistics with a mesh size of $156 \times 32 \times 64$. This was done to keep the computational costs low. For the application to FSI, this is worrying, as the main goal of using (U)RANS with a synthetic turbulence model, is to reduce computational costs. Since there are no comparisons made in literature, it is unsure how the computational time of this method compares to that of other synthetic turbulence methods. The Random Particle Mesh method shows great features in representing turbulence and it could be a befitting model to couple with FSI simulations, however, the computational cost is of concern and must be examined further.

4.6. Synthetic Eddy Method

The Synthetic Eddy Method (SEM) was first proposed by Jarrin et al. [77, 90], and its philosophy is that it mimics the representative coherent eddies of turbulent flow from a structural point of view. In essence, it creates a box of eddies of varying length scales and these eddies are then convected into the domain, with the averaged RANS velocity as convection velocity. The velocity fluctuations are based on the synthetic eddies. Each eddy is given a velocity distribution, the velocity fluctuations are then determined by the distribution and the distance from each eddy. The velocity distribution function gives spatial coherence to the generated

eddies. This method has been mainly used for inflow conditions of LES [79, 90, 97], but recently it has also been applied in the field of computational aeroacoustics [99, 119–121].

Poletto et al. [79] adjusted the method of Jarrin to be divergence-free, this was done by applying the idea of SEM to vorticity, which is then transformed back to velocity. Sescu & Hixon [99] proposed a similar method, where the SEM is applied to the vector potential instead of to the velocity directly, resulting in a divergence-free field. To comply with the Reynolds stresses, Smirnov's method [75] is used. This makes the resultant velocity field only approximately divergence-free. However, this method also satisfies the momentum equation linearized about the mean flow. The method of Sescu & Hixon [99] has been applied in the field of CAA [120, 121]. Hirai et al. [121] proposed to add a decorrelation term for the eddy intensity, to account for the dissipation effect of turbulence. The method of Sescu & Hixon and the addition by Hirai et al. are described below.

The velocity fluctuations are defined by the curl of the vector potential, shown in eq. (4.81). The vector potential field is represented by a superposition of N eddies which are described by their associated vector potential functions ψ^n, displayed in eq. (4.82). The eddy vector potential function are characterised by their shape functions in each direction (eq. (4.83)). In the case of Hirai et al. [121], this was the Gaussian Shape function, shown in eq. (4.84), where r^n is the distance between the spatial position and the centre of the nth eddy, as shown in eq. (4.85). The centre location of each eddy $\mathbf{x}^n$ is taken from a uniform distribution over the box of eddies.

$$\mathbf{v}'(x_1, x_2, x_3) = \nabla \times \mathbf{\Psi}(x_1, x_2, x_3) \tag{4.81}$$

$$\mathbf{\Psi}(x_1, x_2, x_3) = \sqrt{\frac{V_b}{N}} \sum_{n}^{N} \mathbf{\Psi}^n \left(\frac{x_1 - x_1^n}{L_b}, \frac{x_2 - x_2^n}{L_b}, \frac{x_3 - x_3^n}{L_b} \right) \tag{4.82}$$

$$\mathbf{\Psi}^n = \psi_1^n \mathbf{i} + \psi_2^n \mathbf{j} + \psi_3^n \mathbf{k} \tag{4.83}$$

The coefficient C is introduced to adhere to the normalisation as defined by [99]. For the case of a Gaussian shape function, $C \approx 0.516$. ε_i^n determines the strength and sign of the n^{th} eddy. This is a stochastic variable and it is sampled from the normal distribution $N(0,1)$. To preserve the Reynolds stresses, the velocity fluctuations v' are transformed using Smirnov's method [75] of similarity scaling, $u_i' = a_{ij} c_j v_j$, where c_j are the eigenvalues of the Reynolds stress tensor, and a_{ij} are the eigenvectors of the Reynolds stress tensor.

$$\psi_i^n = C \varepsilon_i^n e^{-(3r_n)^2} \tag{4.84}$$

$$r^n = \sqrt{\left(\frac{x_1 - x_1^n}{L_b} \right)^2 + \left(\frac{x_2 - x_2^n}{L_b} \right)^2 + \left(\frac{x_3 - x_3^n}{L_b} \right)^2} \tag{4.85}$$

The locations of the centres of the eddies are convected with the mean flow velocity, which gives a time dependency. However, the intensity of the eddy stays constant, which is not in line which the expected dissipation effect of turbulence. To remedy this, Hirai et al. [121] proposed a method to de-correlate the intensity of the eddies. This is done in a similar method as Billson's time correlation [10], shown in eq. (4.86). Here, the coefficients α_i and β_i are defined in eq. (4.87) and eq. (4.88), respectively. The variable τ_i is the timescale, defined by eq. (4.89), where Hirai et al. introduced a tuning parameter to achieve proper time correlation. The variable $G_i^{(0,1)}$ indicates a sample from the normal distribution $N(0,1)$.

$$\varepsilon_i^n(t) = \alpha_i \varepsilon_i^n(t - dt) + \beta_i G_i^{(0,1)} \tag{4.86}$$

$$\alpha_i = e^{dt/\tau_i} \tag{4.87}$$

$$\beta_i = \sqrt{1 - \alpha_i^2} \tag{4.88}$$

$$\tau_i = f_{\tau_i} \frac{k^n}{\varepsilon^n} \tag{4.89}$$

The presented method shows the ability to reconstruct the Reynolds stresses, as well as provide an accurate correlation for the Reynolds stresses in time and space, while being approximately divergence-free. Furthermore, it showed accurate turbulent kinetic energy decay for the test case of spatially decaying isotropic turbulence [99]. However, the current method does not take the energy spectrum as input. Thus, it is not necessarily able to generate an accurate spectrum. For the application to FSI, it is important to have a correct distribution of energy among the eddies that are closely related to the natural frequency of the structure, to

accurately predict the effect of the pressure fluctuations on the surface interface between CFD and CSM. Kim & Haeri [119] proposed a method to produce synthetic eddies that adhered to the Von Karman energy spectrum. However, this was achieved by adding extra ad hoc parameters and solving an optimisation problem for 15 parameters. This would need to be solved before every individual simulation, as the solution depends on problem-specific parameters, such as the turbulent intensity, turbulent length ratio, and the domain size. Thus while it is possible for an SEM to be modelled after an energy spectrum, it requires a complex procedure. Other methods such as Billson et al. [10], or Shur et al. [9] accomplish similar features while the method is much less complex.

4.7. Power Spectral Density Method

The Power Spectral Density (PSD) methods are a class of methods that aim to predict the power spectral density of pressure fluctuations. In particular, it relates the non-dimensional surface pressure to the non-dimensional frequency. The relations are based on theoretical knowledge, but they are fitted to empirical data, making them semi-empirical. Goody et al. [122] showed a good model including Reynolds dependency, for zero pressure gradient flat plate flow. Rozenberg et al. [123] adjusted Goody's method such that it can handle adverse pressure gradients, this gives good results for adverse pressure gradients, but not for zero pressure gradients. Finally, Lee et al. [124] adjust Rozenberg et al.'s model such that it can handle both situations fairly well. The main disadvantage of this method is that it only provides the Power Spectral Density of the pressure fluctuations, and it is mainly used to calculate the surface pressure fluctuations from RANS. It is possible to construct a time series based on the PSD for a RANS simulation. However, for the application to nuclear fuel rods, the flow is not in steady state. Furthermore, it is uncertain how well the fitted relations for flat plates apply to heavily curved surfaces.

4.8. Summary

In this chapter, the applications and methods of synthetic turbulence were reviewed. It was found that synthetic turbulence has many applications within the fields of LES inflow conditions, LES/RANS hybrid zonal methods, computational aeroacoustics, and fluid-structure interaction. From the review of the current method that is implemented into NRG-FSIFOAM, it was found that some of its assumptions cause the turbulence to not be accurately represented. The current ST model assumes isotropic turbulence, thus the Reynolds stresses are not accurately represented. Furthermore, the convection velocity of each mode has a unit direction, and the effect of turbulence dissipation is not incorporated as well.

From literature, other models were found that had more attractive features, such as the inclusion of the Reynolds stresses. Billson et al. [10] proposed a method that could take the Reynolds stresses into account and provided a more accurate method for time correlation. Castro et al. [72] proposed a method that has similar features, but it introduces several ad hoc parameters and only the diagonal Reynolds stresses are modelled. Shur et al. [9] proposed a method that uses a non-dimensional form of the energy spectrum, causing fewer assumptions. Due to its method for calculating the length scales, it shows a good representation of vortical structures. Shur et al.'s method was originally meant for LES, and therefore the time correlation was not accurately modelled. An interesting option for the new ST method for NRG-FSIFOAM would be to combine Shur et al.'s method with the time correlation method of Billson et al.

The previously discussed models are all Random Flow Generation methods, however other methods also exist. The Digital Filtering method filters white noise such that the fluctuations follow prescribed correlations in time and space. Thus, instead of prescribing an energy spectrum, this is implicitly prescribed by the chosen filter. A consequence of this is that with the current filters being used (Gaussian or exponential), it does not show the same level of agreement with homogeneous isotropic turbulence as RFG methods. The Random Particle Mesh method is similar to the Digital Filtering method, except it filters random particles that are convected with the local flow. This method can be adjusted such that it reproduces a given energy spectrum at an added cost. This method shows great results and attributes, and it is widely used in CAA. However, for 3-D applications, the computational costs are relatively high. Finally, the Synthetic Eddy Method was reviewed. It generates synthetic eddies that are then used to determine the velocity fluctuations. The main disadvantage of this method is that a prescribed energy spectrum can not easily be obtained. For each model, the main characteristics have been summarised in table 4.1. From the proposed methods, the RPM method and an RFG method based on a combination of Shur et al. [9] and Billson et al. [10] seem to be the most fitting synthetic turbulence models for the application of simulating nuclear fuel rods in axial flow.

Table 4.1: A summary of how each model fulfils the desired characteristics that were introduced in chapter 3.

	NRG	**Billson et al. [10]**	**Castro et al. [72]**	**Shur et al. [9]**	**Kim et al. [80]**	**Hu et al. [117]**	**Hirai et al. [121]**
Divergence free	Yes	Approx	Yes	Approx	Approx	Approx	Approx
Models RST	No	Yes	Only diagonal	Yes	Yes	Yes	Yes
Von-Karman Energy Spectrum	Yes	Yes	Yes	Yes	No	Yes [1]	Yes [2]
Convection	Yes	Yes	No	Yes	No	Yes	Yes
Time decorrelation	No	Yes	Yes	No	Yes	Yes	Yes
Computational requirements	Low	Low	Low	Low	High	High	Middle

[1] At additional cost
[2] At high additional cost and complexity

5

A New Pressure Fluctuation Model

Based on the review of the current state-of-the-art synthetic turbulence models, a new model is proposed. This model aims to combine the synthetic turbulence model of Billson et al. [10] with that of Shur et al. [9], into a new model that has the strengths of both respective methods. This synthetic turbulence is then, along with the URANS solution, the input for the pressure fluctuations equation. In this chapter, the new model, called *"AniPFM"*, is discussed. The name is derived from the fact that this model is able to reproduce anisotropic Reynolds stresses. First, the generation of velocity fluctuations is discussed. After this, the generation of the pressure fluctuations is discussed.

5.1. Velocity Fluctuations Generation

The goal is to model velocity fluctuations that are a function of space and time, and that can reconstruct anisotropic Reynolds stresses. The final velocity fluctuations are called $\mathbf{u}_t(x,t)$, and they are constructed from non-dimensional isotropic fluctuations, called $\mathbf{v}_t(x,t)$. The relation is shown in eq. (5.1), where a_{ij} is the Cholesky decomposition of the Reynolds stress tensor R, as shown in eq. (5.2). For the Cholesky decomposition a, it follows that $a^T a = R$. Thus, if $< \mathbf{v}_t(x,t)^2 >= \delta_{ij}$, it follows that $< \mathbf{u}_t(x,t)^2 >$ would be equal to the Reynolds stress tensor. From this it can be concluded that $\mathbf{v}_t(x,t)$ must indeed be isotropic, and the squared-averaged components must be equal to unity.

$$\mathbf{u}_t(\mathbf{x},t) = a_{ij}\mathbf{v}_t(\mathbf{x},t) \tag{5.1}$$

$$a_{ij} = \begin{bmatrix} \sqrt{R_{11}} & 0 & 0 \\ R_{21}/a_{11} & \sqrt{R_{22}-a_{21}^2} & 0 \\ R_{31}/a_{11} & (R_{32}-a_{21}a_{31})/a_{22} & \sqrt{R_{33}-a_{31}^2-a_{32}^2} \end{bmatrix} \tag{5.2}$$

The fluctuations $\mathbf{v}_t(x,t)$ are obtained by applying time correlation methods to non-dimensional fluctuations that are solely a function of space, called $\mathbf{w}_t(x)$. These fluctuations are similar to how Shur et al. [9] calculated their non-dimensional fluctuations. The fluctuations $\mathbf{w}_t(x)$ are calculated through a Fourier decomposition, the equation is shown in eq. (5.3). Here, q_n is the non-dimensional energy, $\boldsymbol{\sigma}_n$ is the direction vector, $\mathbf{k}_n$ is the wavenumber vector, and ϕ_n is a random phase shift with a uniform distribution as given in eq. (4.12), the subscript n denotes that it is for the n-th mode.

$$\mathbf{w}_t(\mathbf{x}) = \sqrt{6}\sum_n \sqrt{q_n}\left[\boldsymbol{\sigma}_n \cos(\mathbf{k}_n \cdot \mathbf{x} + \phi_n)\right] \tag{5.3}$$

The multiplication factor of $\sqrt{6}$ comes from two sources. First, a one-sided signal (i.e. positive wavenumbers) is used to construct the nondimensional velocity fluctuations; thus, each component must be multiplied by 2. Secondly, a requirement for $\mathbf{w}_t(x)$ is that its squared average must be equal to the Kronecker-delta, thus the sum of the squared components of $\mathbf{w}_t(x)$ must be equal to three. The sum of the non-dimensional energy of each mode is equal to one, as shown in eq. (5.4), and the average of a cosine squared is equal to 0.5. Thus, with a multiplication factor of $\sqrt{6}$, eq. (5.5) is achieved, and the requirement is satisfied. Since its square

average must be equal to the Kronecker-delta, the different components must have the same magnitude. This is achieved by having an isotropic distribution of the direction vector.

$$\sum_n q_n = 1 \tag{5.4}$$

$$\sum_i < w_{t,i}^2 >= 3 \sum_n q_n \tag{5.5}$$

5.1.1. Turbulent Kinetic Energy Spectrum

The value for q^n for each mode is defined by a modified Von-Kármán energy spectrum, it is normalized as shown in eq. (5.6), where $E_k(k^n)$ is the modified Von-Kármán energy spectrum evaluated at k^n, and Δk^n is an interval in the spectrum centered around k^n. The exact definition of Δk^n is elaborated upon in section 5.1.2. The modified Von-Kármán spectrum is defined in eq. (5.7), where k_e is the wavenumber at which the energy spectrum has its maximum, and k_η is the Kolmogorov wavenumber. This spectrum is very similar to eq. (4.15), however, a big difference is that now the constant A is no longer necessary, as the value for q^n is scaled by normalization. Because of this, the integral in eq. (4.18) does not have to be evaluated, which reduces the total computational time and the complexity of the model.

$$q_n = \frac{E_k(k_n)\Delta k_n}{\sum_n^N E_k(k_n)\Delta k_n} \tag{5.6}$$

$$E(k) = \frac{(k/k_e)^4}{[1+2.4(k/k_e)^2]^{(17/6)}} exp(-(12\frac{k}{k_\eta})^2) f_{cut} \tag{5.7}$$

The eddy wavenumber k_e can be calculated by $k_e = \frac{2\pi}{l_e}$, where the length scale l_e can be approximated by eq. (5.8), where C_l is a modelling constant, which has been set to 3.0 based on matching the spectrum with that of experimental data of Comte-Bellot & Corrsin [11]. Note that this definition for l_e differs from that of Shur et al.[9]. Shur et al. include a term that takes into account the distance to the nearest wall, however, this method gives a much lower estimation for the pressure fluctuations near walls, due to an underestimation in the eddy wavenumber. The focus of Shur et al.'s work was not on pressure fluctuations; thus, it is logical that this effect was not taken into consideration. This effect is more elaborated upon in section 6.2.5. The Kolmogorov wavenumber is calculated as shown in eq. (5.9).

$$l_e = C_l l_t \tag{5.8}$$

$$k_\eta = 2\pi(\frac{\varepsilon}{\nu^3})^{\frac{1}{4}} \tag{5.9}$$

Finally, the modified Von Kármán spectrum is multiplied by a cut-off filter f_{cut}. Without the cut-off filter, the spectrum continues until the Kolmogorov wavenumber. However, typically the mesh can not resolve wavenumbers that far; otherwise, it would be more favourable to use DNS techniques. Since the inputted spectrum would not be fully resolved, an aliasing effect can be found in the reconstruction of the energy spectrum. To counteract this, a cut-off filter is used, this makes sure that a more correct distribution is found in the reconstructed energy spectrum. The cut-off filter is shown in eq. (5.10), where $k_{cut} = \frac{2\pi}{l_{cut}}$, and l_{cut} is the cut-off length. For the cut-off length, multiple formulations are possible. However, for this thesis it was chosen to focus on the definition given by Shur et al. [9] in eq. (4.45), and the definition as given in eq. (5.11). These two methods were chosen such that the effect of the amount of resolved energy can be quantified and then a correct method can be chosen from the two. This is further elaborated upon in section 6.2.5.

$$f_{cut} = exp\left(-\left[\frac{4max(k-0.9k_{cut},0)}{k_{cut}}\right]^3\right) \tag{5.10}$$

$$l_{cut} = 2V_{cell}^{\frac{1}{3}} \tag{5.11}$$

5.1.2. Wavenumber & Direction Calculations

The smallest wavenumber corresponds to the largest eddy length scale L in the domain, for which a conservative estimate can be found from eq. (5.12). In the case where the flow is stationary, eq. (5.13) is used. There are some other considerations that must be taken into account. The wavenumber at which the peak of the energy spectrum is located was denoted by k_e, naturally this must be larger than the starting wavenumber, otherwise the bulk of the energy is not captured. Furthermore, geometrical considerations must also be taken into account. For this, the user can input a user length scale l_{user}, which denotes the maximum length

that can be captured given the geometry of the problem. For example, in turbulent channel flow the maximum wavelength in the wall-normal direction is equal to the channel height. The largest wavenumber for which the spectrum is sampled is k_{end} (eq. (5.15)), which is based on the cut-off wavenumber as the spectrum quickly goes to zero after this point.

$$k_{start} = \frac{\varepsilon}{max(||\mathbf{u}||^3)} \tag{5.12}$$

$$k_{start} = \frac{2\pi}{L} = \frac{2\pi\varepsilon}{K^{3/2}} \tag{5.13}$$

$$k_{start} = \max\left[\min(k_{start}, \frac{1}{2}k_e), \frac{2\pi}{l_{user}}\right] \tag{5.14}$$

$$k_{end} = \frac{3}{2}k_{cut} \tag{5.15}$$

Given the wavenumber space from k_{start} to k_{end}, the space is divided in N intervals, with $N+1$ edge-wavenumbers. These edge-wavenumbers are used to define Δk_n. The edge-wavenumbers are logarithmically distributed as shown in eq. (5.16), where γ is defined in eq. (5.17). Then the wavenumbers are defined as $k_n = \tilde{k}_{n+1/2}$, i.e. in the logarithmic middle of interval n. The variable Δk_n is defined as $\tilde{k}_{n+1} - \tilde{k}_n$.

$$\tilde{k}_n = k_{start} \cdot e^{\gamma i} \tag{5.16}$$

$$\gamma = \frac{log(k_{end}/k_{start})}{N} \tag{5.17}$$

The wavenumber vector is defined exactly the same as in the previous method of NRG, namely with eq. (5.18), where θ_n, ψ_n are random variables with distributions given in eq. (4.12). Similarly, the condition for continuity is also required for the new model, which resulted in $k_n \cdot \sigma_n = 0$, as mentioned in section 4.3.4. However, a different method is used to determine the direction vector for the new model, because it was found that the old method of NRG for determining the direction vectors resulted in an anisotropic distribution. The old method resulted in over-predicted velocities in the streamwise direction and underpredicted velocities in the wall-normal direction.

In the new method for determining σ_n, another random vector that has a uniform distribution over a unit sphere is generated, namely ζ_n. This vector is generated similarly as $\mathbf{k}_n$, as can be seen in eq. (5.19), with the main difference being that new instances of the random variables are used for each timestep (depending on the time correlation method, see section 5.1.3). Then, σ_n is defined as the normalized cross-product between ζ_n and the wavenumber vector of the n-th mode. Since the dot product of a vector with the cross product of the same vector is equal to zero, the condition stated in eq. (4.3) is met.

$$\mathbf{k_n} = k_n[\sin\theta_n\cos\psi_n, \sin\theta_n\sin\psi_n, \cos\theta_n]^T \tag{5.18}$$

$$\zeta_n = [\sin\theta_\zeta\cos\psi_\zeta, \sin\theta_\zeta\sin\psi_\zeta, \cos\theta_\zeta]^T \tag{5.19}$$

$$\sigma_n = \frac{\zeta_n \times k_n}{|\zeta_n \times k_n|} \tag{5.20}$$

5.1.3. Time Correlation

The procedure for calculating the non-dimensional variable $\mathbf{w}_t(\mathbf{x})$ has been fully defined in the previous subsections. In this subsection, it is explained how correlation methods create a space-time-dependent velocity fluctuation signal from a purely space-dependent velocity fluctuation signal.

Two main phenomena have to be taken into account when constructing a temporally correlated velocity field. Namely, the convection of turbulent eddies and the decorrelation due to the production and dissipation terms. These phenomena are explained more elaborately in section 3.5. The individual phenomena can be modelled quite accurately, but it is difficult to combine these effects. This is why in this subsection four different methods are discussed for time correlation. These four methods will be tested for the turbulent channel flow case, from which the best method will be selected.

Convection & Exponential Correlation There is a method to combine both effects, however this method has its own disadvantages. The method consists of two parts. The first part is to convect the velocity fluctuations by solving for eq. (5.21). Here, $\mathbf{v}_t^{m-1}$ are the non-dimensional velocity fluctuations generated at timestep $m-1$, and U_j is the Reynolds-averaged velocity as calculated by the accompanied URANS simulation. Then in the second part, a new solution $\mathbf{v}_t^m$ is calculated from a combination of the (convected) previous solution $\mathbf{v}_t^{m-1}$, and a newly generated field $\mathbf{w}_t^m$. The coefficients a and b are defined in eq. (5.23) and eq. (5.24) respectively, where τ is the timescale determined from the URANS simulation, and f_τ is a modification factor for fine-tuning the correlation. Billson et al. [10] used a factor of $f_\tau = 17$, for the simulation of a 3D jet. The same factor is used, to test if it can be used as a general coefficient. The coefficients are defined such that the squared mean properties of $\mathbf{v}_t$ are still respected, i.e. $<\mathbf{v}_t^2>=\delta_{ij}$.

$$\frac{\partial \mathbf{v}_t^{m-1}}{\partial t} + U_j \frac{\partial \mathbf{v}_t^{m-1}}{\partial x_j} = 0 \tag{5.21}$$

$$\mathbf{v}_t^m(\mathbf{x}, t) = a\mathbf{v}_t^{m-1}(\mathbf{x}) + b\mathbf{w}_t^m(\mathbf{x}) \tag{5.22}$$

$$a = e^{-f_\tau \Delta t/\tau} \tag{5.23}$$

$$b = \sqrt{1-a^2} \tag{5.24}$$

Note that this method is slightly different from the one proposed by Billson et al. [10]. Billson et al. correlated the actual velocity fluctuations $\mathbf{u}_t$, which is only possible if the simulation is at steady state. This is because in an unsteady case the velocity fluctuations from the previous simulation may not contain the same amount of energy as the newly generated velocity fluctuations. Using non-dimensional velocity fluctuations allows for constant statistical properties of both $\mathbf{v}_t$ and $\mathbf{w}_t$, which means it can also be used in unsteady simulations. A disadvantage of this method is that solving the advection equation numerically can introduce numerical diffusion, which causes the solution of $\mathbf{v}_t^{m-1}$ to be smeared out. To combat this, Billson et al. used a four-point stencil, however, a loss of energy was still observed [10]. In OpenFOAM, only second-order schemes are available, thus this effect will be worse. Ultimately, this causes the replicated Reynolds stresses to be underestimated, which could potentially lead to an underestimation of the pressure fluctuations as well.

Rescaled Convection & Exponential Correlation As mentioned in the previous paragraph, numerically solving for the convection equation introduces a diffusion error to the non-dimensional velocity fluctuations. While $\mathbf{v}_t^{m-1}$ should have a magnitude of $\sqrt{3}$, due to diffusion this can actually be less. To counteract this, the newly introduced velocity fluctuations $\mathbf{w}_t^m$ can be rescaled such that no energy is lost from diffusion. This means that an adjusted value for b must be used, and thus the exponential correlation is not exactly met. Note that this is actually also the case for the non-rescaled Convection & Exponential Correlation method, as $\mathbf{v}_t^{m-1}$ is slightly adjusted by solving the convection equation, giving a different measure for the decorrelation between $\mathbf{v}_t^{m-1}$ and $\mathbf{v}_t^m$.

The new definition of b is given in eq. (5.25). Here, b is defined such that $<(\mathbf{v}_t^m)^2>$ is equal to 1 in each normal direction, and thus no energy is lost. An example of the effect of the rescaling is shown in fig. 5.1 and fig. 5.2, where the values for a and b are taken from a simple channel flow case, the loss of energy is set to 6%, and it is assumed that $<(\mathbf{v}_t^{m-1})^2>$ and $<(\mathbf{w}_t^m)^2>$ are equal to 1, for illustration purposes. As can be seen, the contribution of the newly generated velocity fluctuations $\mathbf{w}_t^m$ increases significantly, and thus the velocity fluctuations decorrelate faster than indicated by the exponential relation. Note that in practice this rescaling can change the relative distribution of the energy. This is because in reality the distribution of $<(\mathbf{v}_t^{m-1})^2>$ is not uniform, due to the difference in diffusion error in the domain.

$$b = \sqrt{1 - \frac{1}{\sqrt{3}} <\mathbf{v}_t^{m-1}\mathbf{v}_t^{m-1}> a^2} \tag{5.25}$$

Solely Exponential Correlation This method solely uses eq. (5.22) to create the time-correlated velocity fluctuations, the previous fluctuations $\mathbf{v}_t^{m-1}$ are not convected. Although this method does not lead to an underestimation in the Reynolds stresses, it can also not represent the convection that the eddies undergo. This will affect the shape of the frequency spectrum, which is ultimately important for FSI simulations.

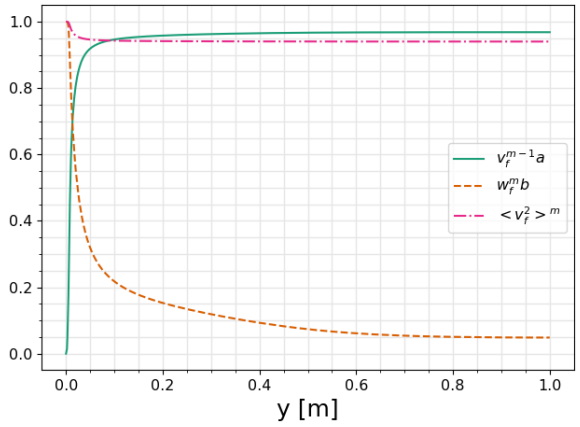

Figure 5.1: Example calculation of the magnitude of the velocity fluctuations of the new time step, with b defined by eq. (5.24).

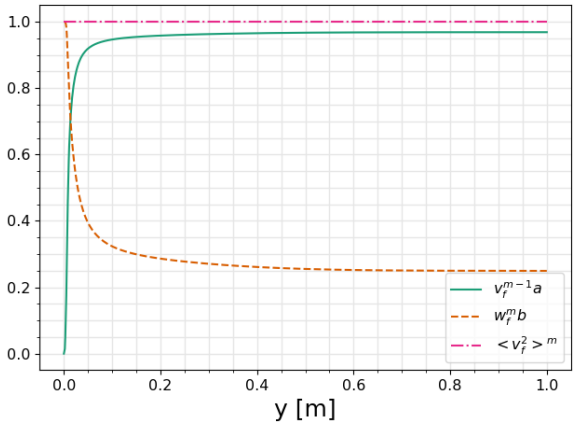

Figure 5.2: Example calculation of the magnitude of the velocity fluctuations of the new time step, with b defined by eq. (5.25).

Solely Convection This method is the most used method for generating a time-correlation in synthetic turbulence, as it is used by Shur et al. [9], Poletto et al. [79], and Ewert et al. [85] among others. With this method, the generated fluctuations are directly a function of time, i.e. $\mathbf{w}_t(\mathbf{x})$ is not created, but $\mathbf{v}_t(\mathbf{x},t)$ is created directly, with eq. (5.26). Here, $\mathbf{U}$ is the velocity as retrieved from the URANS simulation, as opposed to Kottapalli et al. [14], who used a different definition for the convection velocity. With this method, the random variables are not a function of time, but they are created in the first iteration and stored. This method makes use of the exact solution of the advection equation, thus no numerical methods are used for this, and the Reynolds stresses are still replicated accurately.

$$\mathbf{v}_t(\mathbf{x}) = \sqrt{6}\sum_n \sqrt{q_n}\left[\sigma_n \cos(\mathbf{k}_n \cdot (\mathbf{x} - \mathbf{U}t) + \phi_n)\right] \tag{5.26}$$

5.2. Pressure Fluctuations Generation

In this section, it is explained how the pressure fluctuations are calculated based on the modelled velocity fluctuations. The governing equation is elaborated upon, as well as the boundary conditions that are used for this equation.

5.2.1. Governing equation

Similarly to the previous model of NRG as described in section 4.2, the aniPFM calculates the pressure fluctuations based on the Poisson equation derived in section 3.4. However, the assumption of $\nabla \cdot u_t = 0$ is not used. As discussed in section 4.3.4, the divergence criterion is met exactly, but the discrete divergence criterion is not. For this reason, assuming that $\nabla \cdot u_t = 0$ can introduce an error in the calculation of the pressure fluctuations. Instead, the pressure fluctuation equation as shown in eq. (3.31) is solved, meaning that this error is not introduced. Note that this assumes that the full pressure fluctuations are computed, but in reality only the fluctuations caused by the resolved velocity fluctuations are solved for. Thus, the effect of the unresolved turbulence on the pressure fluctuations is not accounted for in this method. Due to the non-linear source terms, this filtering effect would add an extra term to the right-hand side of the equation.

Similarly to the previous model of NRG, the average of the source term is subtracted over the domain, such that the average is zero. This was done because mathematically it should be zero, but due to introduced randomness this is not exactly the case. In turn, a non-zero average source term can cause nonphysical behaviour in the solution, as elaborated upon in section 4.2.3.

5.2.2. Boundary Conditions

Boundary conditions have to be specified to solve eq. (3.31). The boundary conditions for the pressure fluctuation equation have similar challenges as boundary conditions for LES or DNS simulations. Because the solution is a highly fluctuating field, it is not possible to use uniform values as boundary conditions, such

as is typically done with RANS simulations. The main focus of the *AniPFM* is to apply it to internal flows in nuclear reactor applications. Due to this, three boundary conditions are considered, inlet, outlet, and wall. The specification of the inlet and outlet boundaries are usually related, thus these are treated together. The boundary conditions specified here are for incompressible flow.

Wall Boundary Typically, a zero-gradient boundary condition for the pressure is used in DNS and RANS simulations [56]. This is because the pressure that is solved for is actually a "pseudo-pressure" that acts as a Lagrange multiplier to constrain the velocity to be divergence-free. Since this boundary condition is used for both the instantaneous pressure and the averaged pressure, it can be derived that it must also hold for the pressure fluctuation. I.e, the boundary condition for the pressure fluctuations at the wall is defined by eq. (5.27).

$$\frac{\partial p'}{\partial n} = 0 \tag{5.27}$$

Inlet/Outlet Boundary: Dirichlet There are several options for the inlet and outlet boundary conditions. These types can be divided into Dirichlet boundary conditions (fixed value) and Neumann boundary conditions (fixed derivative). There are three options for Dirichlet boundary conditions, periodic, mapped, or calculated boundaries. In case of periodic flows, i.e. in cases where the flow statistics are expected to be equal at the inlet and the outlet, periodic boundary conditions can be used. In case of periodic boundary conditions, the problem is underdetermined, as in reality only one boundary condition is prescribed. This would give a nonunique solution, but it is solved by prescribing an extra constraint, namely, that the average of the pressure fluctuations over the whole domain is equal to zero. For nonperiodic flow cases, mapped or calculated boundary conditions can be used. With a mapped boundary, a slice at a specified location in the previous timestep is mapped onto the boundary in the new timestep. For this method, it is important that the flow properties at the map location are equal or close to the flow properties at the boundary. Finally, a calculated boundary condition can be used. From dimensional analysis, an estimation for the pressure fluctuations can be based on the velocity fluctuations and the density [125]. This relation is adjusted such that the average is zero, as shown in eq. (5.28).

$$p' = \frac{\rho u'^2}{\sqrt{2}} - \overline{\frac{\rho u'^2}{\sqrt{2}}} \tag{5.28}$$

Inlet/Outlet Boundary: Neumann Another option for the inlet and outlet boundary is to use a Neumann boundary condition. However, this has consequences for the behaviour of the pressure fluctuation equation in the full domain. To understand this, a comparison is drawn with a simpler one-dimensional example; see eq. (5.29). The solution to this equation is given in eq. (5.30). Given the definition of the pressure fluctuations, they must oscillate around zero and their average must be zero. For pressure fluctuations to oscillate around zero, the coefficient c_1 must be equal to zero, otherwise a linear profile will govern the solution. With a zero-gradient boundary condition at $x = 0$, eq. (5.31) holds. As can be seen, in case the indefinite integral of $f(x)$ at the boundary is not equal to zero, c_1 will not be equal to zero either, leading to a linear profile in the solution. To prevent a linear profile from dominating the solution, it is recommended not to use Neumann boundary conditions for the inlet and outlet.

$$\frac{\partial^2 p'}{\partial x^2} = f(x) \tag{5.29}$$

$$p' = c_1 x + c_2 + \int\int f(x)dxdx \tag{5.30}$$

$$\frac{\partial p'}{\partial x} = 0 = c_1 + \int f(0)dx \tag{5.31}$$

5.3. Summary

The AniPFM is a pressure fluctuation model, which based the generation of synthetic turbulence on the models of Billson et al. [10] and Shur et al. [9]. This new model aims to take the strengths of both methods. The

formulation of the non-dimensional velocity fluctuations resemble that of Shur et al., but instead of modelling the total kinetic energy, only the resolved kinetic energy is modelled. Furthermore, the definition of the eddy length scale is adjusted to not include the wall distance. For time correlation, several methods have been implemented, based both on Billson et al. and Shur et al. These different methods will be compared in section 6.2.7. Boundary conditions for the pressure fluctuation equation were formulated, and it was found that the zero-gradient condition is suitable for wall boundaries, whereas a Dirichlet condition based on dimensional analysis was prescribed for inlets and outlets. Neumann boundary conditions for inlet and outlet could possibly lead to errors The presented pressure fluctuation model consists of many parts, and thus it is hard to keep track of every moving part. For this reason, an overview of the various computational steps of the AniPFM is shown in a flowchart in fig. 5.3.

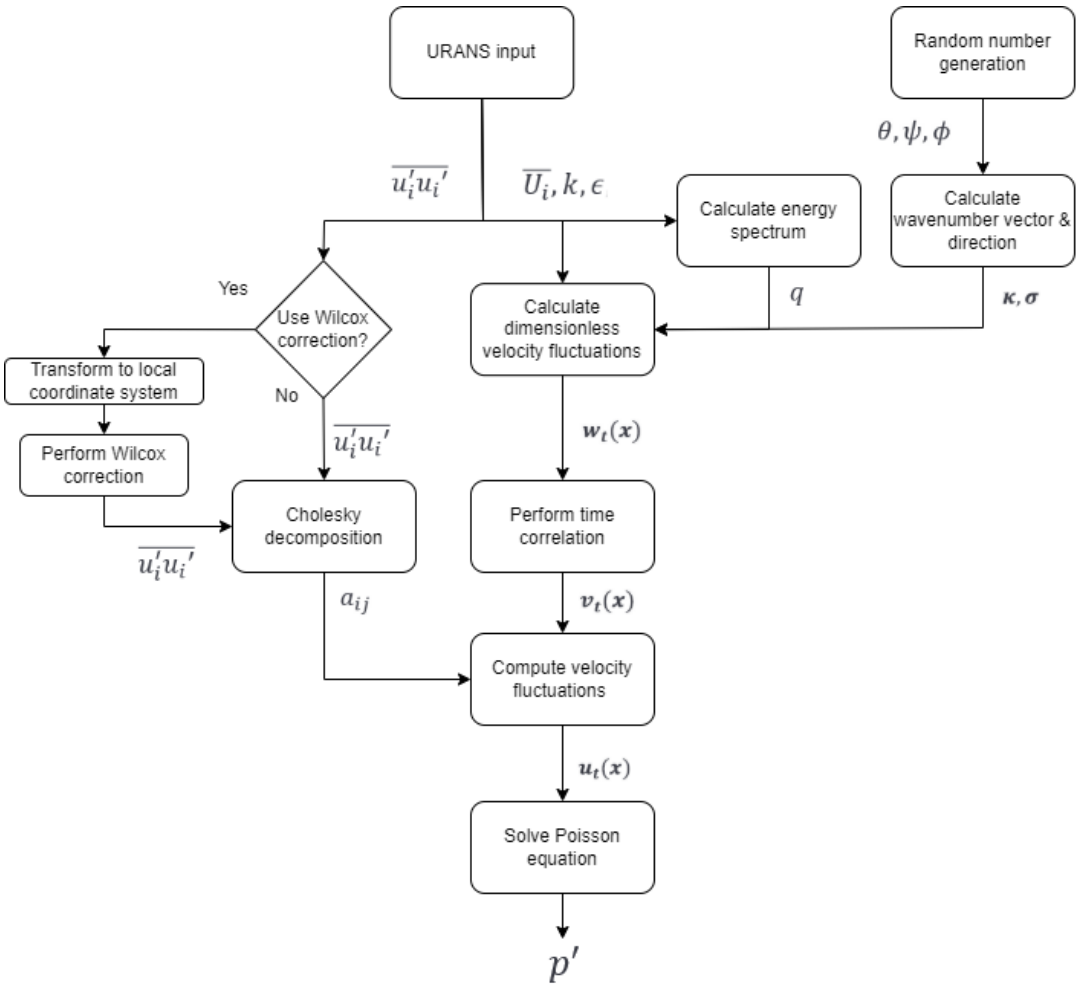

Figure 5.3: A flow-chart of the different computational steps of the proposed AniPFM.

6

Verification & Validation of AniPFM

A new pressure fluctuation model was elaborated upon in chapter 5, where the different modelling choices were explained. In this chapter, the model is verified and validated using two test cases, namely, Homogeneous Isotropic Turbulence (HIT), and Turbulent Channel Flow (TCF). For these test cases, both experimental and numerical validation data exists, which will be used to assess the performance of the new aniPFM. In previous work, these test cases were also explored for the PFM previously used by NRG [102]. The name *PFM* refers to the previous model of NRG, and the name *AniPFM* refers to the model that was implemented during the thesis. Using the same test cases for both models allows for a comparison between the results of PFM and AniPFM. This chapter is solely for the verification and validation of the AniPFM, it is not yet applied to FSI test cases. The chapter is divided into two sections, each covering one respective test case. In these sections, the methodology for the numerical simulation is explained, and then the results are discussed. In the first section, the HIT case is discussed. The turbulent channel flow case is discussed in the latter section.

6.1. Homogeneous Isotropic Turbulent Box

In this section, the simulations of homogeneous isotropic turbulence are discussed. The set-up for these simulations was discussed in a previous report from NRG [102]. However, this report is unpublished, thus for the sake of keeping a self-contained thesis, the set-up is repeated here. For the HIT validation case, two different simulations will be done. One replicating the experiment of Comte-Bellot & Corrsin [11], and one replicating the DNS of Gotoh et al. [12]. First, the methodology for both cases is discussed. After this, the results for both cases are elaborated upon.

Both cases have slightly different purposes. First, the Comte-Bellot & Corrsin experiment gives data of the three-dimensional energy spectrum, as well as data on the time-correlation of the axial velocity. The energy spectrum data will be used to verify that the PFM indeed can replicate an isotropic energy spectrum. Next to this, the ability of the AniPFM to replicate the actual time correlation is tested. Several parameters of the AniPFM will be varied such that the influence of these parameters can be evaluated. The DNS of Gotoh et al. contains data of the nondimensional energy and pressure spectrum for several Reynolds numbers Re_λ, where λ is the Taylor microscale. This data will be used to validate the implementation of the calculations of the pressure fluctuations for several Reynolds numbers.

6.1.1. Methodology

For both simulations, a box of $LxLxL$ is created, which is discretized by a uniform mesh of $NxNxN$. All boundaries of the box are periodic, and there is a mean velocity of zero. There are no source terms, thus the turbulence in the box will decay over time.

Comte-Bellot & Corrsin

In table 6.1, the turbulence models, initial conditions, and time step are shown. For the URANS simulation, the initial values of k and ε are taken from the paper published by Comte-Bellot & Corrsin [11]. The initial kinetic energy was calculated as $k = \frac{3}{2}u_{11}^2$, given that the flow is isotropic. A backward time scheme is used, giving second order accuracy in time. The time step is not based on CFL number, because the velocity is very close to zero, thus this is not the limiting factor. The timestep is limited by the resolution of the experiment

of Comte-Bellot & Corrsin [11]. The time step was set such that similar sampling intervals could be taken in the simulation as in the experiment. The initial pressure was set to $1e-6$, as a zero pressure would lead to a non-converging solution. The PISO-algorithm is used to solve the system of equations. A mesh of $64 \times 64 \times 64$ is used, unless specified otherwise.

Table 6.1: Details of the simulations replicating Comte-Bellot & Corrsin.

Turbulence model	k-ε
Initial k [m^2/s^2]	0.4740
Initial ε [m^2/s^3]	0.07393
Initial U [m/s]	0
Initial p [Pa]	1e-6
ν [m^2/s]	1.5e-5
Time step [s]	0.001
Duration [s]	0.874

Gotoh et al.

The approach is slightly different for this case, as Gotoh et al. only provide nondimensional data. This data is matched by achieving the same Reynolds number Re_λ. The definitions of the Taylor microscale and Re_λ are given in eq. (6.1) and eq. (6.2), respectively. From choosing the dynamic viscosity, and up to how far the energy spectrum should be resolved, the values for k and ε can be determined for the URANS simulation. The numerical experiment by Gotoh et al. was non-decaying, and only data of the energy and the pressure spectrum is known. Thus, it is only necessary to look at an instantaneous point in time. In order to keep the mesh size reasonable, the spectrum was resolved up to 50% of the Kolmogorov length scale, for a mesh of $128 \times 128 \times 128$. Several mesh sizes are used, in order to evaluate the accuracy of the AniPFM for coarser meshes. An example of a simulation set up is shown in table 6.2, where the initial conditions are shown for $Re_\lambda = 70$.

$$\lambda = \sqrt{\frac{10\nu k}{\varepsilon}} \tag{6.1}$$

$$Re_\lambda = \frac{\frac{2}{3}\sqrt{k}\lambda}{\nu} \tag{6.2}$$

Table 6.2: Details of the simulations replicating Gotoh et al. at $Re_\lambda = 70$.

Turbulence model	k-ε
Initial k [m^2/s^2]	0.012568
Initial ε [m^2/s^3]	0.01377
Initial U [m/s]	0
Initial p [Pa]	1e-6
ν [m^2/s]	1.5e-5
Time step [s]	0.001
Duration [s]	0.001 (instantaneous solution)

6.1.2. Energy Spectrum Replication

Replication of the energy spectrum is essential for simulating turbulence, as the energy spectrum contains information about the spatial correlation, the total kinetic energy, and the dissipation rate. In this subsection, it is verified whether the AniPFM can accurately represent the energy spectrum of isotropic turbulence, and how it compares to the results of the PFM. The replication of the energy spectrum depends on two factors. Namely, it depends on how well the input spectrum for the AniPFM matches the experimental spectrum, and on how well this input spectrum is replicated by the AniPFM.

First, the input spectrum is compared to the experimental spectrum of Comte-Bellot & Corrsin [11], and to the input energy used in the previous PFM. As mentioned in section 4.3.3, the input spectrum differs slightly

from the input spectrum of the PFM, and the definition for the wavelength that contains the maximum energy is also slightly different. For the purpose of this comparison, the cut-off filter is not used. The influence of the cut-off filter is investigated in section 6.1.5. In fig. 6.1, the two input spectra are compared. As can be seen, the wavelength with maximum energy is better predicted by AniPFM, and both methods show a small deviation in the inertial range of the spectrum. The peak of the spectrum is slightly underpredicted by the PFM, giving a slightly different energy distribution.

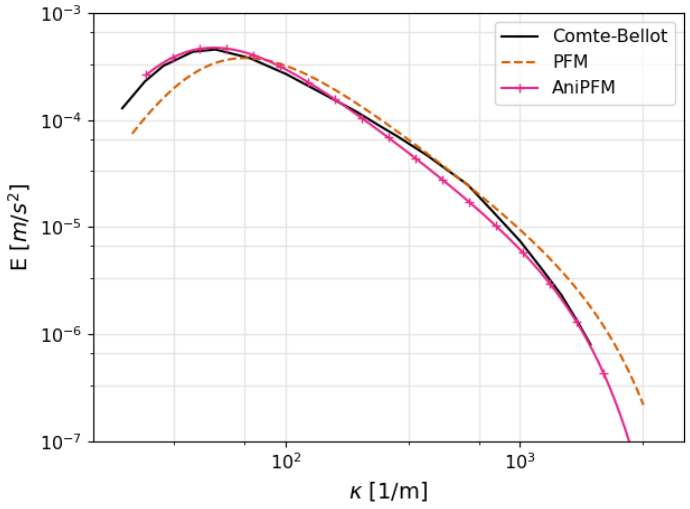

Figure 6.1: Comparison of the input spectrum for PFM and AniPFM, with experimental results from Comte-Bellot & Corrsin [11].

The spectrum of the created velocity fluctuations can be evaluated with eq. (6.3). Here, $k_n = k_0 n$, where k_0 is the smallest captured wavenumber, the hats denote the Fourier transformed variables, and $*$ denotes the complex conjugate. Due to the homogeneous and isotropic nature of the turbulence in this case, the spectrum can directly be evaluated from the magnitude of the wavenumber.

$$E(k_n) = \sum_{k_0(n-1/2)\leq k\leq k_0(n+1/2)} \frac{1}{2}\hat{\mathbf{u}}_f \cdot \hat{\mathbf{u}}^*_f k_0^{-1} \tag{6.3}$$

As shown in fig. 6.1, the input spectrum is generated until the Kolmogorov scale. However, typically CFD simulations don't have a mesh that is refined enough to resolve this scale. The resolvable wavenumber is dependent on the size of the grid cells. The largest resolvable wavenumber is the cut-off wavenumber, this corresponds to a wavelength of $\frac{\Delta x}{2}$, due to the Nyquist limit. On a uniform grid, the cut-off wavenumber can be calculated by using eq. (6.4).

$$k_{cut-off} = \frac{\pi}{\Delta x} \tag{6.4}$$

The influence of the differences of the input spectrum is seen in the output spectrum of both methods. The energy spectrum is reconstructed from the velocity fluctuations for both methods, the results for the PFM and the AniPFM are shown in fig. 6.2a and fig. 6.2b respectively, with N = 64. Comparing fig. 6.2 with fig. 6.1, both methods closely replicate their respective input spectrum and the experimental spectrum, with the exception of the region near the cut-off wavenumber. Due to this, the PFM shows a slight underprediction for the larger wavelengths. Near the cut-off wavenumber, there is an increase in energy for both spectra. This is due to the fact that the generated velocity fluctuations are based on a spectrum that continues until the Kolmogorov wavenumber. Because of this, velocity fluctuations are created at higher wavenumbers than that can be reconstructed from the grid, due to mesh limitations. This causes an alias effect where the energy from the velocity fluctuations at the wavenumbers higher than the cut-off wavenumber is redistributed into the resolved part of the spectrum. This effect is most noticeable near the cut-off wavenumber. The effect of this will also translate to a similar effect in the pressure fluctuations, which is discussed in section 6.1.4.

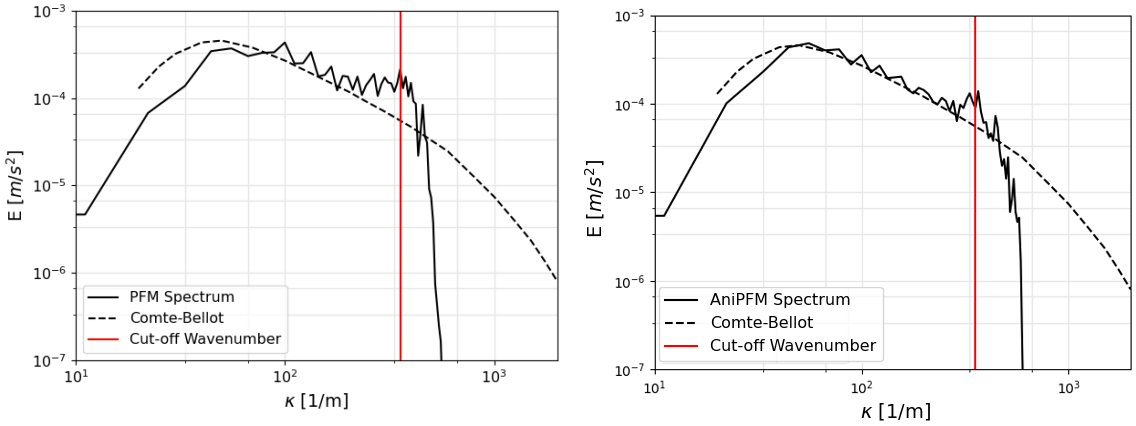

(a) PFM

(b) AniPFM.

Figure 6.2: The reproduction of the energy spectrum of both models, versus the spectrum from Comte-Bellot & Corrsin [11].

6.1.3. Velocity Time Correlation

The time correlation of the velocity and pressure fluctuations is of great importance for the application to FSI simulations of nuclear fuel rods. This is because the pressure fluctuations that have a frequency close to the eigenfrequency of the fuel rod, are expected to have the largest influence on the excitation of the fuel rods. Thus, it is important to model the distribution of the pressure fluctuations over the frequency domain correctly. For this reason, the time correlation is investigated. From the experiment of Comte-Bellot & Corrsin [11], the correlation of the velocity fluctuations in the x-direction are known, these are compared to the time correlation of the velocity fluctuations of the PFM and the AniPFM.

The method for determining the time correlation is shown in eq. (6.5). Here, τ is the time difference from t_0, and the indices i and j refer to the velocity components. For this comparison, the correlation between the velocity in x-direction is investigated, thus $R_{1,1}$ is calculated. The brackets denote an assemble average. In case of Comte-Bellot & Corrsin, a time-average of a single point was taken. However, for the simulations, a spatial average of a plane at $x = 0$ on the y-z plane was taken. The results for the comparison are shown in fig. 6.3.

$$R_{i,j}(x,\tau) = \frac{< u_i'(x,t_0)\,u_j'(x,t_0+\tau) >}{< u_i'(x,t_0)\,u_j'(x,t_0) >} \tag{6.5}$$

As can be seen, the PFM shows a much faster decorrelation than the experiment by Comte-Bellot & Corrsin, and the AniPFM. This is due to the fact that the PFM uses a convection velocity not based on the mean velocity, but rather on the wavenumber and the dissipation rate. Because of this, the convection velocity for each mode is not directly dependent on the mean velocity. As can be seen, this can lead to a fast decorrelation in the velocity fluctuations. Regarding the AniPFM, a much better approximation is shown, which a maximum error of 11.8% points. This verifies that using an exponential relation for the correlation is an improvement over the previous method, for isotropic turbulence.

6.1.4. Pressure Fluctuations

The variable that is passed from the AniPFM to the structural solver is p', so it is of utmost importance that it is verified that this can be replicated correctly. For this reason, the pressure spectrum is evaluated, and compared to both the results of the previous model of NRG, and to DNS results of Gotoh et al. [12]. The experiment of Comte-Bellot & Corrsin did not include the pressure spectrum, so the DNS data of Gotoh et al. is used for this reason. The set-up of the simulation of the case of Gotoh et al. is shown in section 6.1.1.

In previous work at NRG, it was shown that in the case of HIT, the pressure fluctuation spectrum was able to be approximately replicated, given that the velocity fluctuations replicated the energy spectrum [102]. However, it was shown that this was only possible for $Re_\lambda > 125$. This behaviour holds not only for PFM simulations, but also for LES simulations, and is thus not inherently due to the PFM. It was also noticed that

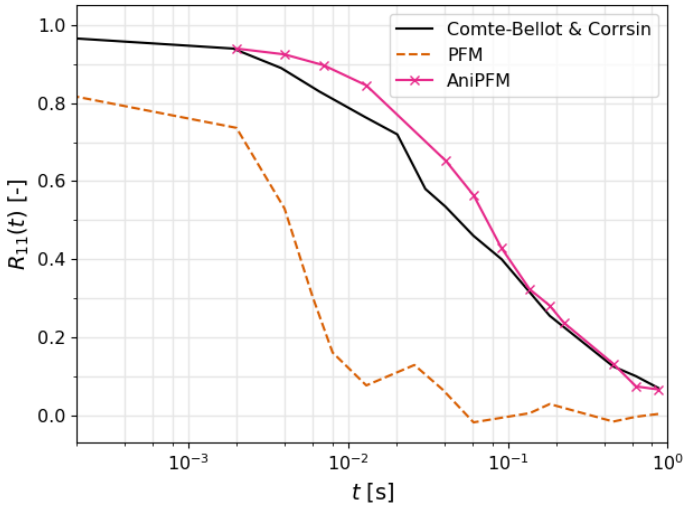

Figure 6.3: Comparison of the velocity time correlation between the PFM, AniPFM, and the experimental data from Comte-Bellot & Corrsin [11].

the pressure spectrum only adheres to universal scaling laws for $Re_\lambda > 125$. For this reason, the pressure spectra are compared at $Re_\lambda = 284$. The simulation was done with a mesh size of $128x128x128$, as to simulate up to 50% of the Kolmogorov length scale. This was done because the non-dimensional spectrum shows a decrease in magnitude in the range $0.1 < \kappa\eta < 1.5$, and it was investigated if this decrease could be accurately modelled. The results for both the PFM and the AniPFM are shown in fig. 6.4.

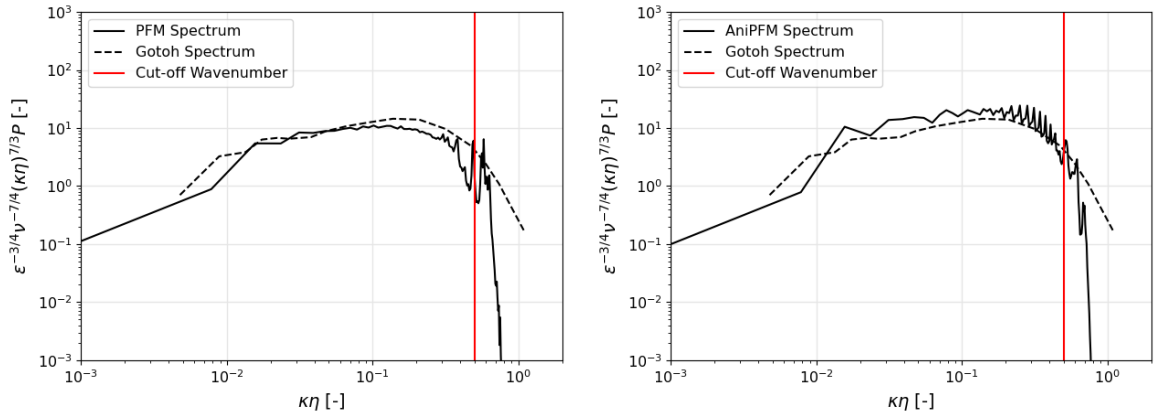

(a) PFM

(b) AniPFM.

Figure 6.4: The reproduction of the pressure spectrum of both models, versus the spectrum from Gotoh et al. [12].

As can be seen, both models show a similar result w.r.t. the DNS data from Gotoh et al. The PFM shows a small underprediction, which was expected due to the small underprediction of energy in the larger wavelengths. The AniPFM shows a slight overprediction. Due to the nature of HIT, the equation for the pressure fluctuations, eq. (3.31), can be simplified. The mean velocity is zero everywhere, and the Reynolds stresses are constant over the whole domain. Thus, the terms with the derivatives of the velocity and the Reynolds stresses are cancelled, as shown in eq. (6.6). From this it can be concluded that based on the pressure spectrum, the turbulence interaction term can be accurately modelled by the AniPFM.

$$\frac{\partial^2 p'}{\partial x_i \partial x_i} = -\rho \left[\frac{\partial^2}{\partial x_i \partial x_j} \left(u_i' u_j' \right) \right] \tag{6.6}$$

Next to the pressure spectrum, the root-mean-squared (RMS) pressure fluctuations were also calculated. This was done for several mesh sizes to determine how well the AniPFM approximates the pressure fluctu-

ations at coarser meshes. The results are shown in table 6.3. As can be seen, for a mesh of $16x16x16$, the results are still within 10% of the DNS results. This mesh study was also done in previous work at NRG [102], where it was shown that the PFM also predicts the root-mean-squared pressure fluctuations within 10% with a mesh of $16x16x16$. Lastly, as mentioned in chapter 4 and chapter 5, the divergence criterion is met exactly, but the discrete divergence criterion is not met exactly. In previous work of NRG, it was found that this did not affect the pressure fluctuations related to the turbulence-turbulence interaction term [102]. Since the formulation and the results for HIT are so similar for the PFM and the AniPFM, it is expected that this also does not influence the pressure fluctuations generated by the AniPFM.

Table 6.3: The p'_{rms} values of the AniPFM compared to DNS data of Gotoh et al. [12], for several mesh sizes.

Mesh	**p'_{rms}**	**Error w.r.t. DNS [%]**
16	0.02002	-9.6
64	0.0213	-3.7
128	0.0219	-1.1
DNS	0.0221	n/a

6.1.5. Cut-off Filter Effect

In section 6.1.2, it was found that simulating the velocity fluctuations up to the Kolmogorov length scale gave an unphysical peak in the energy distribution at wavenumbers near the cut-off wavenumber. This was due to the fact that the energy contained in the wavenumbers lower than the cut-off wavenumber can not be reconstructed, thus this is distributed over the rest of the spectrum. To prevent this unphysical behaviour, a cut-off filter can be employed. This cut-off filter was discussed in section 5.1.1, and here the effects on the HIT case are shown. As discussed in section 5.1.1, there are two options for the definition of the cut-off length. In this situation however, the definition is not relevant, as both method give the same cut-off length in case of a uniform grid. The effect of this adjustment in cut-off length formulation is discussed in section 6.2.

In fig. 6.5, the input energy spectrum with and without the cut-off filter is shown, for N = 64. As can be seen, in case the cut-off filter is employed, the energy distribution sees a sharp drop after the cut-off wavenumber. The resulting reconstructed energy spectrum from the velocity fluctuations can be seen in fig. 6.6. As can be seen, there is now no additional energy concentrated near the cut-off wavenumber. The cut-off filter was also applied to the case of Gotoh et al., to evaluate the effect on the pressure fluctuations, with N = 64. Here it was concluded that the filter had a similar effect in diminishing the unphysical heap of pressure fluctuations with a wavenumber near the cut-off wavenumber. From this, it was found that for N = 64, the error w.r.t. the DNS results reduced from 3.7% as given in table 6.3, to solely 2.4%.

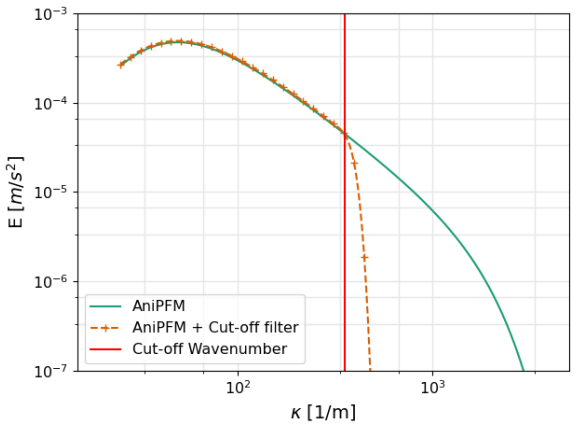

Figure 6.5: The input spectrum for the AniPFM both with and without the cut-off filter, for N = 64.

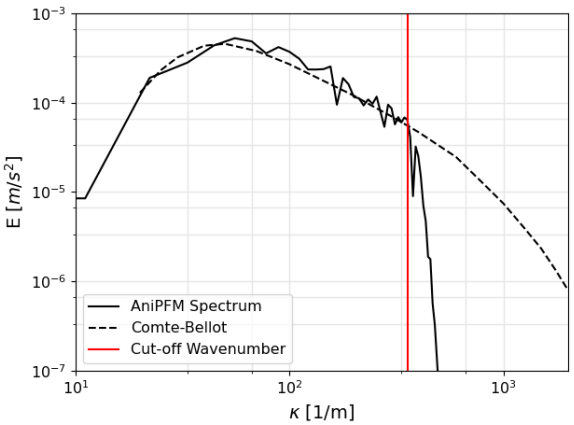

Figure 6.6: The resulting energy spectrum of AniPFM with the cut-off filter employed, compared to the experimental values of Comte-Bellot & Corrsin [11].

6.1.6. Summary

This concludes the simulation of homogeneous isotropic turbulence with the PFM and the AniPFM. It was found that both models produce similar results for isotropic turbulence. However, the peak of the energy spectrum is better predicted by the AniPFM, as well as the time correlation of the velocity fluctuations. Both models showed similar results for the pressure fluctuations. Finally, with the implementation of the cut-off filter, the non-physical accumulation of energy near the cut-off wavenumber was prevented, granting a more accurate energy and pressure spectrum for the AniPFM. It was expected that both models gave similar results, as they both should be able to predict isotropic turbulence. This case was mainly intended as a verification of the implementation of the AniPFM.

6.2. Turbulent Channel Flow

In this section, the simulations of a turbulent channel flow are discussed. The set-up for these simulations was discussed in a previous report from NRG [102]. Similarly to the HIT case, the set-up is repeated here. The results of the TCF are compared to the DNS results of Abe et al. [13], who performed a DNS simulation at several Reynolds numbers. The highest Reynolds number was equal to $Re_\tau = 640$, thus this Reynolds number is used for comparison. The DNS of Abe et al. [13] was chosen, as from this simulation, information was available about the mean flow characteristics along the wall-normal direction, such as the mean velocity and Reynolds stresses. It also contained spectral data about the pressure and velocity components, both near the wall and closer to the bulk of the flow.

The TCF case is used to verify several aspects of the AniPFM. Errors in the prediction of the pressure fluctuations can be introduced from several sources, here the effect of each source is discussed. The different sources of errors are the modelling error, the discretization error, and finally the input error. Furthermore, due to the fact that random numbers are used to construct the wavenumber and direction vector, an uncertainty in the results is introduced. It was also observed that the RMS pressure fluctuations changed slightly over time, introducing another uncertainty. After assessing these errors and uncertainties, the modelling choices are further investigated by evaluating the effects of certain individual model choices.

6.2.1. Methodology

In this case, the flow between two infinitely long and wide stationary plates is simulated. The simulation domain used is equal to $6\delta \times 2\delta \times 3\delta$, where δ is the mid-channel height. The mesh has a size of $N_x \times N_y \times N_z$, which are kept as variables. The mesh distribution is uniform in the x- and z-direction, and it is geometrically expanding from the wall to the mid-channel height in the y-direction. The mesh in the y-direction is configured such that $y^+ \approx 1$ for the first grid cell from the wall. The variable y^+ is the non-dimensionalised wall-normal distance, normalized by eq. (6.8), where u_τ is defined as in eq. (6.7). Similarly, u^+ can be defined as in eq. (6.9). The boundary conditions are as follows: periodic in the x- and z-direction, and a wall boundary condition at $y = 0$ and at $y = 2\delta$.

$$u_\tau = \sqrt{\frac{\tau_w}{\rho}} \tag{6.7}$$

$$y^+ = \frac{y u_\tau}{\nu} \tag{6.8}$$

$$u^+ = \frac{u}{u_\tau} \tag{6.9}$$

The results of this test case will be compared to the DNS of Abe et al. [13], at a Reynolds number of $Re_\tau = 640$, which is the Reynolds number based on the wall friction velocity, as shown in eq. (6.10). From Abe et al., it was found that this is equivalent to $Re_{bulk} = 24{,}228$, where Re_{bulk} is defined as in eq. (6.11), with the bulk velocity defined as in eq. (6.12). By using the same bulk Reynolds number as Abe et al., the results of both simulations can be compared. Since the boundary conditions are periodic, without imposing one, there would be no apparent pressure gradient and thus no flow. Thus, a pressure gradient must be imposed. This can be done by adding a momentum source to the Navier-Stokes equations. Specifically, in OpenFOAM, a bulk velocity force is imposed, meaning that the resultant flow will have this bulk velocity. By setting the viscosity and the mid-channel height, the bulk velocity is determined. The details of the set-up of the channel flow simulation are summarized in table 6.4. No wall model is used since the y^+-value of the first cell is roughly equal to 1, meaning that the flow is resolved up to the wall. A backward time scheme is used, giving second order accuracy in time. The time step is determined by the CFL number, which does not exceed the value of 0.7. The PISO-algorithm is used to solve the system of equations each time step. The settings for the AniPFM are varied for each performed simulation, and these details are mentioned in their

respective sections. Unless specified otherwise, the cubic-root-volume method for the cut-off length scale is used. As convergence criteria for the governing equations, an absolute criterion is used of $1e-6$ for all governing equations, including the pressure fluctuation equation.

Channel flow is inhomogeneous in the wall-normal direction, but it is statistically homogeneous in the streamwise and spanwise directions. For this reason, the results of channel flow are averaged over the stream- and spanwise directions if possible (unless otherwise specified), thus showing only a profile that varies with the wall-normal coordinate. This property of the channel flow also allows for the reconstruction of velocity and pressure spectra in both the stream- and spanwise directions. The results shown of one-dimensional spectra have been averaged in its other homogeneous direction, e.g., if a spectrum along the streamwise direction is shown, it has been averaged along the spanwise direction.

$$Re_\tau = \frac{u_\tau \delta}{\nu} \quad (6.10) \qquad Re_{Bulk} = \frac{U_{bulk} 2\delta}{\nu} \quad (6.11) \qquad U_{Bulk} = \frac{1}{\delta}\int_0^\delta < U > dy \quad (6.12)$$

Table 6.4: Details of the channel flow simulation set-up.

	URANS + PFM
Turbulence model	Variable
Wall model	n/a
Re_{bulk} [-]	24428
ν [m^2/s]	2e-5
δ [m]	1
U_{bulk} [m/s]	0.24428

6.2.2. Qualitative Results

While quantitative results such as root-mean-squared values and pressure spectra are absolutely necessary for evaluating the effectiveness of the AniPFM, qualitative results are as important. Without qualitative results, statistics such as mean or mean-squared values can sometimes be misleading. For this reason, qualitative results are shown in this subsection. The instantaneous pressure and velocity fluctuations are shown at an arbitrary moment in time, in fig. 6.7. In fig. 6.8, their RMS values are shown.

In fig. 6.7a and fig. 6.7b, the instantaneous pressure and velocity fluctuations respectively are shown for the top wall, the right periodic side, and the periodic outlet. It can be seen that mainly at the top wall the pressure fluctuations have a large magnitude, in the mid of the channel the fluctuations are much closer to zero. This is due to the fact that the highest velocity and Reynolds stress gradients are near the wall. For the instantaneous velocity fluctuations, it is clear that near the wall, the magnitudes are larger than in the mid-channel, but at the wall they are exactly zero. This is due to the no-slip condition. In both the pressure and velocity fluctuations, no apparent patterns are visible in the streamwise and spanwise directions.

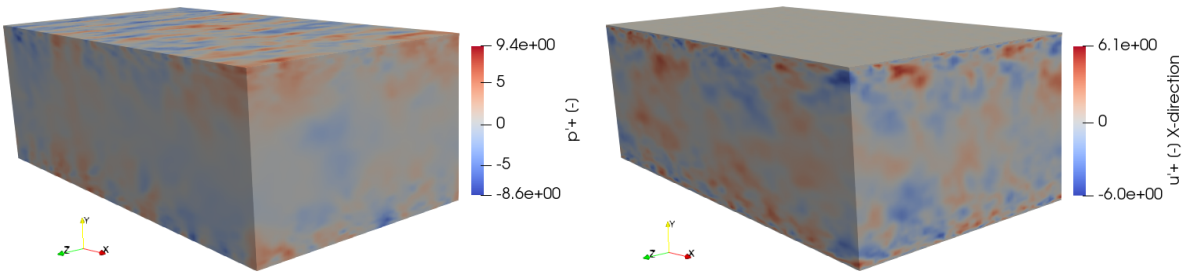

(a) Pressure fluctuations.

(b) Velocity fluctuations (x-component).

Figure 6.7: The instantaneous pressure and velocity fluctuations, taken from AniPFM.

The mean squared pressure and velocity fluctuations are shown in fig. 6.8. The mean is calculated by a time average over 16 flow-through times, which equates to 2000 samples at each point in space. As can be

seen, the variables are almost constant over the span and streamwise direction, with only small variations in these directions. This was as expected, as the channel flow case is supposed to be homogeneous in these directions. Since this is also the case for the AniPFM results, it is justified to collapse this data to a single profile as function of the wall-normal direction, which is done in the subsequent subsections.

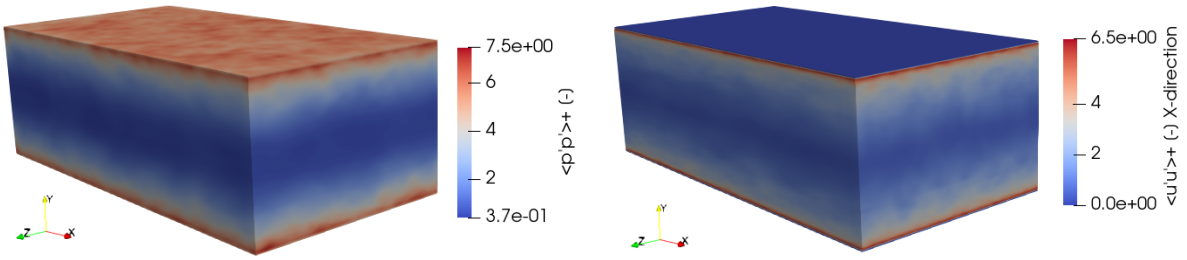

(a) Pressure fluctuations.

(b) Velocity fluctuations (x-component).

Figure 6.8: The mean squared pressure and velocity fluctuations, taken from AniPFM.

6.2.3. Uncertainty Sources

There are several numerical considerations that can affect the results of AniPFM simulations. These manifest in both uncertainties and errors. For example, there is an inherent uncertainty in statistical approaches like root-mean-squared variables. The AniPFM also uses a statistical approach in order to determine the direction of wavenumbers, which in turn introduces an uncertainty. In order to provide statistically meaningful results, these uncertainties are evaluated in this subsection.

Convergence Uncertainty

In theory, the RMS pressure fluctuations along the wall-normal direction of the channel should converge to a single profile. This also happens in practice, but it seems that the solution tends to oscillate around the converged value for a long time. The time that it takes to converge within a maximum difference of e.g., $1e-5$ during the last 5 flow-through times, is unfeasibly long for the larger computations that have been carried out. Solutions do seem to come within a slightly larger range relatively quickly. For this reason, the results of the RMS pressure fluctuations are denoted with an uncertainty range of 2 standard deviations, i.e., a 95.4% confidence interval, based on the RMS pressure fluctuation value at the wall over the last 5 flow-through times.

An example of the time history RMS pressure fluctuation at the wall is shown in fig. 6.9. This was obtained by performing an AniPFM simulation with a mesh of $35x64x25$, with 1024 wavenumber modes. The values are normalized by the average RMS pressure fluctuation over the last 5 flow-through times. From this simulation it was found that for the last 10 flow through times, the 95.4% confidence interval was equal to $\pm 0.0514\%$. However, when looking at a much earlier time interval, for example from 300 to 500 seconds, it was found that the uncertainty range with the same confidence interval was still only $\pm 0.236\%$. For this reason, simulations are performed until a feasible end time, and the uncertainty due to oscillations in the wall p'_{rms} is reported in the results.

Randomness Uncertainty

Next to the uncertainty due to oscillations in the time-averaged values of the RMS pressure fluctuations, there is also an uncertainty due to the use of random numbers in AniPFM. In fig. 6.10, the time history of the RMS pressure fluctuations are shown for 10 different runs that have used different random numbers. The amount of effect of random numbers is also varying per method of time correlation. For example, for the Convection & Exponential Correlation (C&EC) method every iteration new random numbers are used. However, for the pure convection method, one set of random numbers is used, as the turbulence is assumed to be frozen and convected with the mean flow. In fig. 6.10, the pure convection method is used.

As can be seen, even after a long period, there is still a difference between the individual simulations. From these performed simulations, an uncertainty range is again determined. It was found that these simulations were all within a $\pm 2.68\%$ range of the mean value with a confidence interval of 95.4%. From this value, it is also logical that the simulations are not run until the oscillation uncertainty is reduced to $1e-5$ levels, as the uncertainty is mainly dominated due to the uncertainty caused by the random numbers. If the convection

and correlation method for time correlation is used, then the uncertainty range reduces to ±0.249%. This is due to the fact that new random numbers are generated each timestep. Thus, this method would be preferred, given that it results in a much smaller uncertainty.

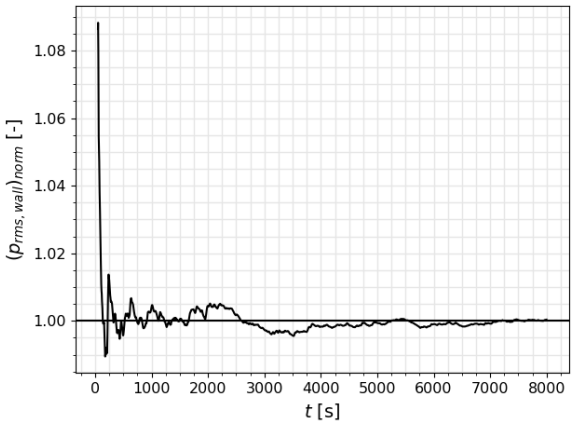

Figure 6.9: The normalized root-mean-squared pressure fluctuations at the wall, versus the simulation time.

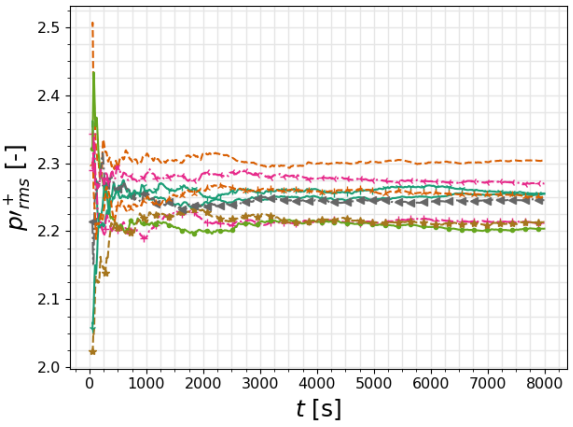

Figure 6.10: The root-mean-squared pressure fluctuations at the wall versus the simulation time, for various runs, with varying random seeds.

Since this type of evaluations are quite computationally expensive to perform, it is not possible to determine the uncertainty range of all simulations on a different mesh. Instead, it was solely performed on the $35x64x25$ mesh, as it is one of the coarsest meshes used for the evaluation of the AniPFM in channel flow. It was reasoned that the uncertainty ranges of finer meshes were likely to be smaller than that of the coarse mesh, as with larger sample size, the finer meshes show better statistical convergence. For this reason, the uncertainty w.r.t. the randomness added to AniPFM was extrapolated from the $35x64x25$ mesh to the other meshes.

This uncertainty range is only applicable if a different seed-number is used for the initialization of the random numbers, or if the amount of random numbers used is different between simulations. Thus, only when applicable, for example, when comparing the results of simulations with different numbers of modes, this uncertainty is applied to the uncertainty range.

6.2.4. Error Sources

There are several sources of errors that cause a discrepancy between the AniPFM results and experimental/DNS data. For example, the governing equations are discretized in small control volumes, which introduces a discretization error. In typical CFD simulations, this is purely due to the discretization of the fluid domain. However, in the case of the AniPFM, the energy spectrum is also discretized into modes, which introduces a discretization error as well. If the physics were perfectly described by the governing equations, then the discretization error would be the only error. However, both the URANS turbulence model and the AniPFM make assumptions which means that the physics are not perfectly described. Even if the AniPFM would receive the exact mean flow quantities, there would still be an error in the statistical quantities of the pressure fluctuations. This is referred to in this subsection as “modelling error”. Next to this, the input data from URANS is not perfectly in line with reality, meaning that this also introduces an error. First the discretization errors are discussed, and then effects of the modelling error and the URANS input error are elaborated upon in this subsection.

Mode Discretization Error

The energy spectrum is approximated by a finite number of modes, as shown in eq. (5.3). The number of modes used determines how well the spectrum is approximated, but it also heavily affects the computational time. For this reason, it is important to know how big of an effect the number of modes has on the accuracy of the final solution. In this subsection, only the RMS pressure fluctuations are evaluated, but the number of modes can also have an effect on the “smoothness” of the reproduced spectrum.

The RMS pressure fluctuations for various numbers of modes are shown in fig. 6.11. As can be seen, the

amount of modes does have an influence on the results, but there is not a clear trend. Excluding the 64 mode simulation, a maximum error of $4.04 \pm 2.86\%$ can be found near the wall, relative to the simulation with the highest number of modes. Thus, while there is a definite effect of the number of modes, the randomness uncertainty is mainly dominating. However, another effect of using fewer modes is that the amount of random numbers used also reduces. This is hypothesized to affect the randomness uncertainty. In particular, it is hypothesized that the uncertainty will grow with fewer modes being used.

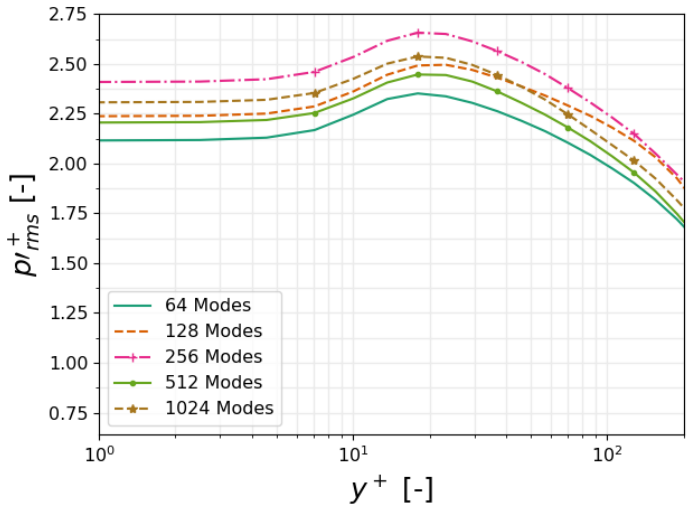

Figure 6.11: The root-mean-squared pressure fluctuations along the wall-normal coordinate for various numbers of modes.

Mesh Discretization Error

A mesh study on the convergence of the AniPFM w.r.t. the RMS pressure fluctuations is different from a normal RANS mesh study. This is because in RANS, the mesh fineness has mostly an effect on the wall modeling and the approximation of differential operators. However, in the AniPFM, the mesh fineness has both an effect on the approximation of differential operators, and an effect on how much energy of the flow is modelled. The amount of turbulent kinetic energy that is modelled has a direct effect on the magnitude of the pressure fluctuations, thus in theory a convergence study of the RMS pressure fluctuations would result in a finest mesh that is DNS-like.

For the mesh study simulations, the AniPFM was used with 1024 Fourier modes, and for time correlation method, pure convection was used, with a uniform convection velocity equal to the bulk velocity. The same seed number was used to initialize the random numbers in all simulations, to prevent any introduced uncertainty due to randomness. The value of y^+ for all simulations was equal to $y^+ = 0.8$, the expansion ratio was based on this accordingly.

The normalized RMS pressure fluctuations along the wall normal coordinate for several meshes are shown in fig. 6.12. Note that the x-axis is log-scaled. For clarity, the values at the wall are reported in table 6.5. As can be seen in table 6.5, for the finest two grids, the second-finest grid actually falls into the confidence interval of the finest grid. From this it was concluded that the RMS pressure fluctuations were converged, and that further refinement in the grid would result in negligible differences in the RMS pressure fluctuations.

This is interesting, as the finest grid does not fully resolve the velocity fluctuations. In fact, the grid is quite far from fully resolving the velocity fluctuations. In fig. 6.13, the cut-off wavenumber to Kolmogorov wavenumber ratio is given along the channel height. As can be seen, in the finest simulation, the velocity fluctuations are only resolved up to 6% of the Kolmogorov wavenumber, near the wall. From this it can be concluded that in channel flow, the largest contribution to the pressure fluctuations is from velocity fluctuations with large length scales.

It is also noted that by an increase of 25 times in total mesh elements, the RMS pressure fluctuations only differ by 7.68%. Thus, it is possible to use quite coarse meshes and still obtain RMS pressure fluctuations close to the result on very fine meshes. However, it must be kept in mind that the ultimate goal of AniPFM is not to model the total RMS pressure fluctuations, but rather to model the pressure fluctuations that will

excite fuel rods when subjected to axial flow. In this sense, it was earlier hypothesized that only the frequencies near the eigenfrequency of the fuel rods are important, which can be translated to spatial discretization requirements based on the convection velocity. To test this hypothesis, mesh dependency tests were done for the FSI calculations in chapter 7, where a focus is kept on which frequencies (and thus wavenumbers) are resolved.

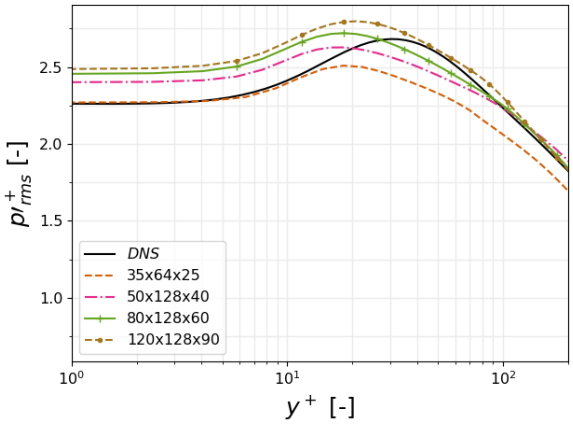

Figure 6.12: The root-mean-squared pressure fluctuations along the wall-normal coordinate for various meshes, versus the DNS results of Abe et al. [13].

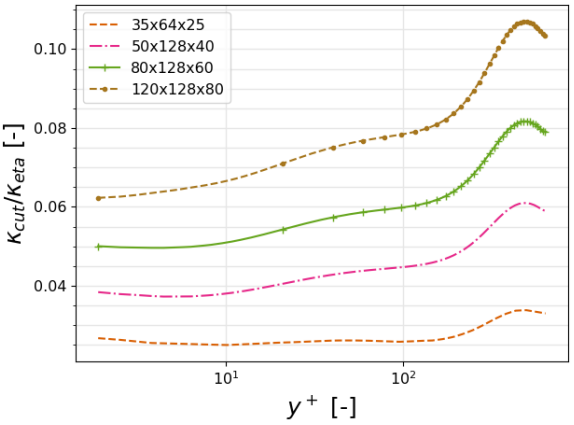

Figure 6.13: The cut-off wavenumber over the Kolmogorov wavenumber along the wall-normal direction, for various mesh sizes.

Table 6.5: The p'_{rms} values at the wall for the various grids.

Grid size	$\mathbf{p'_{rms}}$ [-]	**Error w.r.t. Finest Mesh** [%]
35x64x25	2.281 ± 0.00424	7.83 ± 0.17
50x128x40	2.406 ± 0.0131	2.79 ± 0.53
80x128x60	2.469 ± 0.00494	0.24 ± 0.20
120x128x90	2.475 ± 0.00688	± 0.28

The mesh study shown in fig. 6.12 was mainly focussed on the x- and z-direction, where only the coarsest mesh had a different resolution in the y-direction. In fig. 6.14, a mesh study in the y-direction is performed. The resolution of the first cell at the wall was again kept constant at $y^+ = 0.8$, and the expansion ratio was based on this and the total number of cells. This resulted in expansion ratios of 1.2 for the coarsest mesh, down to 1.05 for the finest mesh. As can be seen, the different grid sizes show very close results, and from $N_y = 64$ and onwards, the results can be deemed converged. This shows that as long as the first point at the wall is similar, the growth rate in the wall-normal direction has a small effect on the results.

Other tests were also performed with different y^+ values of the wall-adjacent cell. It was found that for an accurate prediction of the wall RMS pressure fluctuations, the first cell must have a y^+ value in the flat range near the wall, as shown in fig. 6.14. This gives a range of $0 < y^+ < 5$ for the value of the first cell. With y^+ values higher than that, the first cell is located in or near the peak shown in fig. 6.14, which causes a bad estimation of the pressure fluctuations at the wall. For this, it is not possible to use a wall-model, as the instantaneous pressure fluctuations are computed, not solely the Reynolds-averaged quantity. Thus, it is recommended to use meshes that will resolve the flow up to the wall, with a value of $0 < y^+ < 5$ for the first cell centre.

Modelling Error

It was found in section 6.1, that the AniPFM could accurately predict the root-mean-squared pressure fluctuations, with only roughly a 1% error w.r.t. DNS data. Thus, for the HIT case, the modelling error was very limited. This is because certain aspects of the AniPFM are based on isotropic turbulence. For example, the wavenumber vector is based on isotropy, as its direction is uniformly distributed over a unit sphere. Next to this, the energy spectrum formulation is based on isotropic turbulence, which is then later rescaled to match the Reynolds stresses of the URANS solution. The method of determining the wavenumber that contains the most energy is also based on isotropic turbulence. Thus, while the AniPFM can produce anisotropy in the

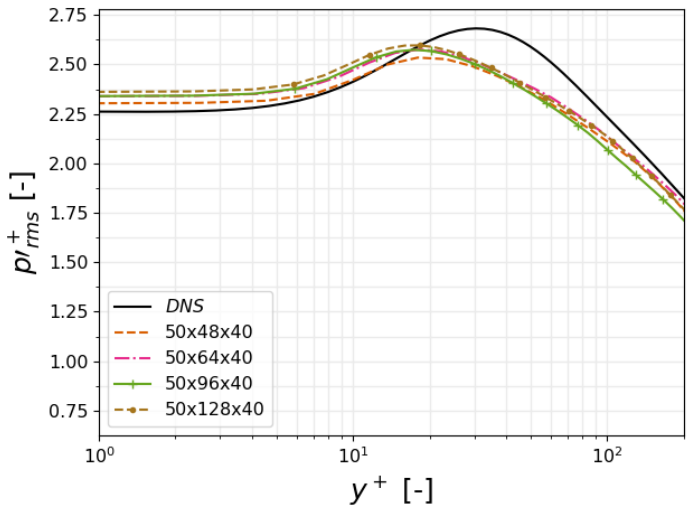

Figure 6.14: The root-mean-squared pressure fluctuations along the wall-normal coordinate for various meshes, versus the DNS results of Abe et al. [13].

Reynolds stresses, certain aspects of the model are still rooted in isotropy. This is expected to introduce a certain error in the prediction of the root-mean-squared pressure fluctuations, as well as in the spectra of the velocity and pressure fluctuations.

To evaluate the modelling error, the mesh is refined until the root-mean-squared pressure fluctuations are converged over the wall-normal direction of the channel. Furthermore, the mean velocity, Reynolds stress, kinetic energy and dissipation rate profiles of Abe et al.[13] are used as the input to the AniPFM, imitating a URANS solution. For this particular simulation, the AniPFM was used with 1024 Fourier modes, and for time correlation method, pure convection was used, with a uniform convection velocity equal to the bulk velocity. The same seed number was used to initialize the random numbers in all simulations, to prevent any introduced uncertainty due to randomness. It was found that at a mesh of $120x128x90$, the results only showed a small difference with respect to coarser meshes. The results for the root-mean-squared pressure fluctuations and the Reynolds stresses are shown in fig. 6.15 and fig. 6.16, respectively.

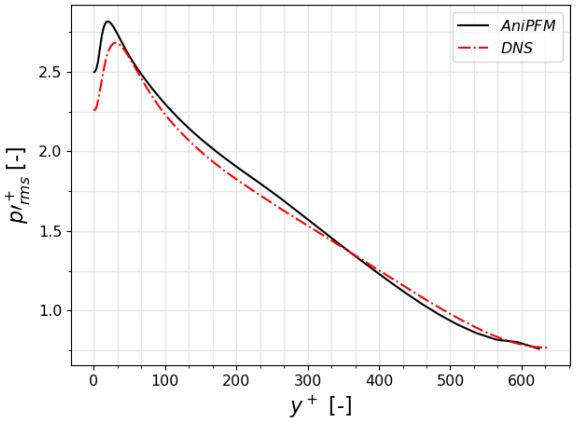

Figure 6.15: The root-mean-squared pressure fluctuations along the wall-normal coordinate, versus the DNS results of Abe et al. [13]. DNS data is used as input.

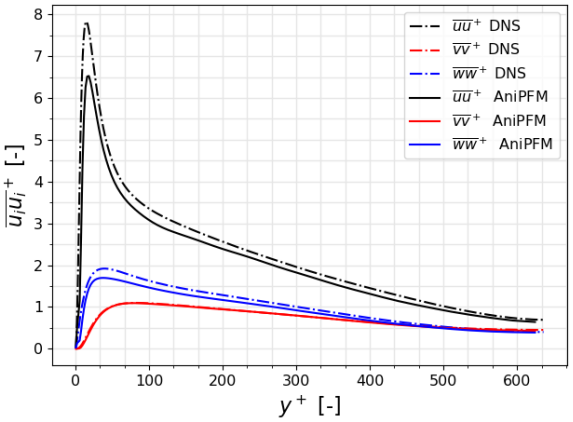

Figure 6.16: The Reynolds stress profiles along the wall-normal coordinate, versus the DNS results of Abe et al. [13]. DNS data is used as input.

As can be seen, the RMS pressure fluctuation at the wall is equal to 2.475 ± 0.0641. This uncertainty contains the uncertainties mentioned in the previous subsections. This gives an error of $9.22 \pm 2.83\%$ with respect to the DNS data. From the Reynolds stresses in fig. 6.16, it can be concluded that not all turbulent length

scales are resolved, as the total energy is not exactly replicated. However, it was found that these unresolved scales have a negligible effect on the pressure fluctuations, as for a slightly coarser mesh, the results remained unchanged. Since the mesh was converged, and the Reynolds stresses and mean velocity profiles are taken directly from DNS, the error in the pressure fluctuations presented here are purely due to model errors in the AniPFM. Further away from the wall, it can be seen that the predictions are much closer to the DNS data. This was expected, as the flow near the wall shows far more anisotropic behaviour than the flow in the bulk of the channel, thus the modelling error was expected to be larger here.

URANS Input error

From the previous section, it was found that given a converged grid solution and the Reynolds-Averaged inputs from DNS data, the AniPFM gave an error of $9.22 \pm 2.86\%$ with respect to the DNS solution of Abe et al. [13]. However, in real cases DNS data is not available, and actual URANS simulations have to be performed in order to utilize the AniPFM. This introduces an additional error that is caused by the differences between DNS results and URANS results. In this subsection, this error is evaluated, in terms of the RMS-value for the pressure fluctuations. But first, the URANS results for the mean flow variables are compared to DNS data.

For the URANS solution, the $k-\omega\ SST$ model is used as turbulence model. This model was chosen for several reasons. Namely, it was found in section 6.2.4 that the simulation has to be resolved up to the wall in order to give an accurate estimate of the pressure fluctuations at the wall, thus wall-model-only models were not applicable. This unfortunately meant that the available Reynolds stress models in OpenFOAM were not eligible to be used. The elliptic-blending RSM can be resolved up to the wall, but this model is not available in OpenFOAM. It is recommended for future work that this model is implemented in OpenFOAM, in order to evaluate if this model combined with the AniPFM gives a more accurate solution. Other URANS turbulence models that are implemented by third parties also exist, such as the Hellsten EARSM [126] and the Wallin & Johansson EARSM [68]. However, it was found that in the case of channel flow, the $k-\omega\ SST$ model gave very similar results to the previously mentioned EARSMs, especially when coupled with the Wilcox-correction shown in eq. (3.35) through eq. (3.37).

In eq. (6.13), the governing equation for the pressure fluctuations in channel flow is shown. This equation is derived from eq. (3.31), where the derivatives of the mean flow velocity and of the Reynolds stress tensor in the x and z-direction are equal to zero for channel flow. From this equation, it can be seen that especially the derivative of the Reynolds stress in the wall-normal direction is important. For this reason, the $k-\omega\ SST$ model was chosen over the $k-\varepsilon$ model, as the $k-\omega\ SST$ model combined with the Wilcox correction gave a closer estimation of the $<vv>$ component of the Reynolds stress.

$$\frac{\partial^2 p'}{\partial x_i \partial x_i} = -\rho\left(\frac{\partial U}{\partial y}\frac{\partial v'}{\partial x} - \frac{\partial \overline{v'v'}}{\partial y^2} + \frac{\partial}{\partial_i \partial_j} u_i' u_j'\right) \tag{6.13}$$

The URANS solution was run until steady state was achieved, after which the AniPFM was turned on. Steady state was determined by the value for Re_τ, the solution was run until this variable did not change any more. The URANS simulation converged to a value of $Re_\tau = 625$, which is 2.5% off of the DNS results of Abe et al. [13]. A small error was expected, as URANS has an inherent error due to turbulence modelling. This steady state was achieved after 600s, after which the AniPFM was turned on. The results for the mean velocity and Reynolds stress profiles are shown in fig. 6.17. As can be seen, the mean velocity profile is quite well approximated, with only a small overestimation between $50 < y^+ < 500$. The Reynolds stresses show less satisfactory results. For the yy-component of the Reynolds stress tensor, especially near the wall, it is overestimated. Since this component is predicted to have a large influence on the pressure fluctuations, this could also indicate an overestimation of the pressure fluctuations, Furthermore, the xx-component of the Reynolds stress tensor is highly underestimated.

The AniPFM simulation was run on a $120x128x90$ mesh, with 1024 wavenumber modes. In fig. 6.18, the results from the AniPFM are shown. As can be seen in fig. 6.18b, with the given mesh the kinetic energy is well-resolved, with only the energy of the smallest scales being unresolved. As predicted, the RMS pressure fluctuations are overpredicted with respect to the results of the AniPFM with DNS input, as shown in fig. 6.18a. The wall RMS pressure fluctuations are equal to 2.822 ± 0.0062. It is hypothesized that this is mainly due to the steep gradient of the yy-component of the Reynolds stress near the wall. It can be seen that the mean flow variables as predicted by URANS give an additional error of roughly $14.0 \pm 0.19\%$, with respect to the outcome of the AniPFM with DNS data as input. From a mesh study with URANS inputs, it was found that this error roughly holds for coarser meshes as well. In total, this gives an error of $24.86 \pm 3.05\%$ with respect to the DNS results of Abe et al. [13]. This is quite a large error, and a large component is due to the error from URANS

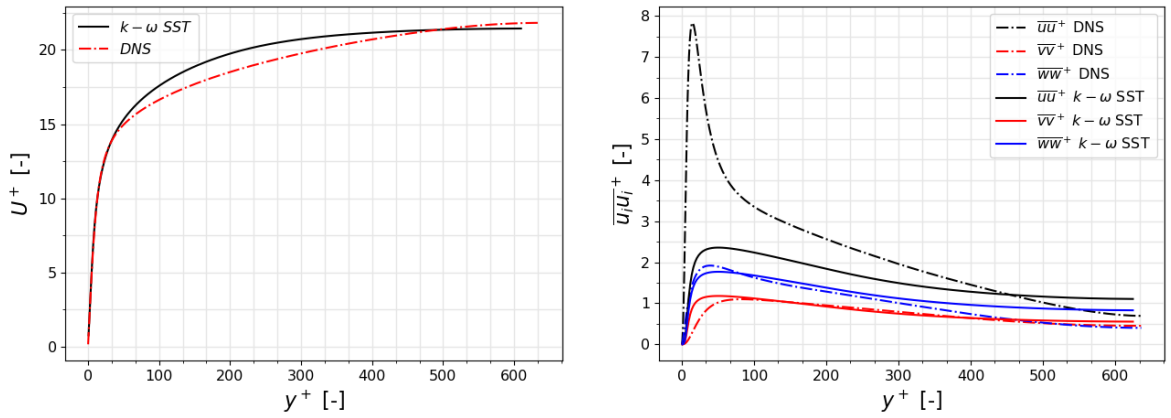

(a) Mean Velocity.

(b) Normal Reynolds stresses, with Wilcox correction.

Figure 6.17: URANS profiles versus the DNS data of Abe et al. [13].

input, thus for this reason it is recommended to implement a wall-resolved RSM that can better approximate the Reynolds stresses. For comparison, the previous PFM of Kottapalli et al. [14], showed an underestimation of roughly 47% with respect to the DNS data.

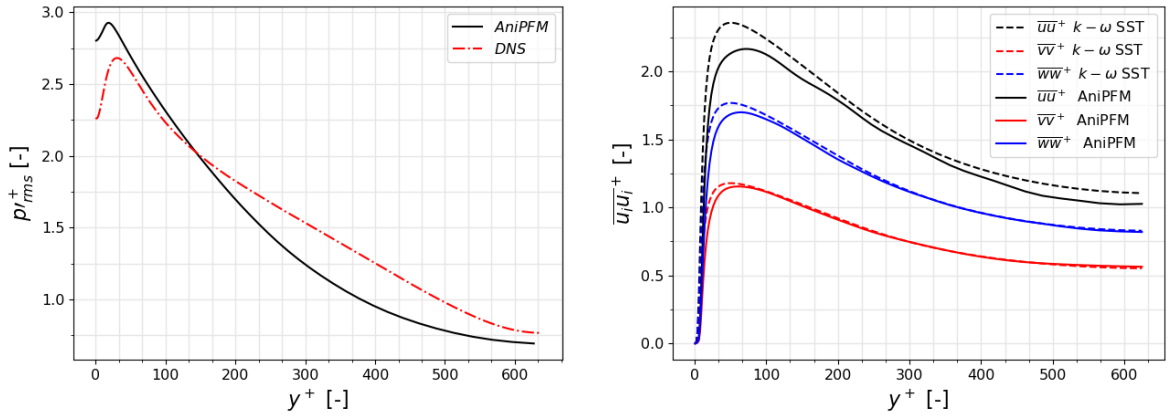

(a) RMS pressure fluctuations of the AniPFM with URANS inputs, versus the DNS results of Abe et al.[13]

(b) Normal Reynolds stresses with Wilcox correction, URANS versus AniPFM.

Figure 6.18: AniPFM results with URANS input from the $k-\omega$ SST model.

To further illustrate the effect of the input Reynolds stress tensor, the AniPFM simulation is rerun, but with the $k-\varepsilon$ model. The same mesh and settings are used as for the $k-\omega$ SST simulation, thus also the Wilcox correction is applied to the Reynolds stress tensor. The RMS pressure fluctuations and the Reynolds stresses are shown in fig. 6.19a and fig. 6.19b, respectively. As can be seen, the Reynolds stresses predicted by the $k-\varepsilon$ model are much higher than in fig. 6.17b, especially the yy-component of the Reynolds stress, and especially near the wall. This translates to a much higher RMS value for pressure fluctuations, as shown in fig. 6.19a. The wall RMS pressure fluctuations are equal to 4.164 ± 0.0065, which is almost 50% higher than the results of the $k-\omega$ SST model.

6.2.5. Wavenumber Spectra & Length Scales Effect

Several length scales are defined in the AniPFM that have an influence on how the energy spectrum is shaped, and how far it is resolved. These length scales are the length scale at which the maximum energy is stored, and the cut-off length scale. In this subsection, the definitions of these length scales are investigated, as well as the influence they have on the wavenumber spectra. First, l_e, the length scale with maximum energy is discussed.

As discussed in section 5.1.1, the definition of l_e was chosen to differ from Shur et al. [9]. Shur et al. use

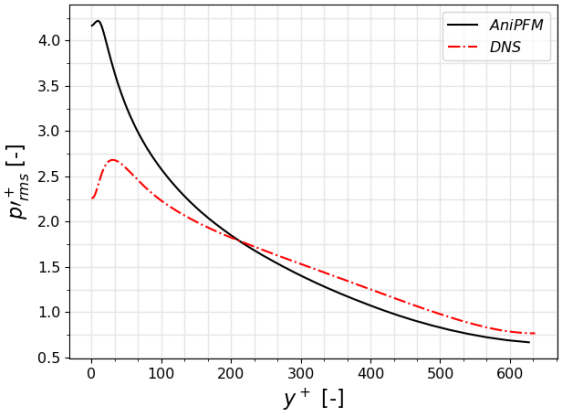

(a) RMS pressure fluctuations of the AniPFM with URANS inputs, versus the DNS results of Abe et al.[13]

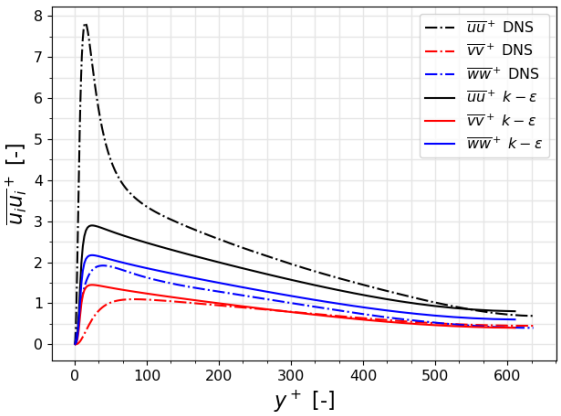

(b) Normal Reynolds stresses with Wilcox correction, DNS versus AniPFM.

Figure 6.19: AniPFM results with URANS input from the $k-\varepsilon$ model.

the wall distance d_w in their definition, whereas in the definition of the AniPFM, this is not used. In fig. 6.20, the wall distance and the URANS length scale are compared to each other, for channel flow at $Re_\tau = 640$. Note that the wall distance length scale is always smaller than $3l_t$. However, at the mid-channel the turbulence is very close to isotropy, as shown in fig. 6.17b. So while the length scale should be close to $3l_t$ in the mid-channel, this is not the case with the method of Shur et al. [9]. This leads to an underestimation in the energy of the lowest wavenumbers, which in turn also leads to an underestimation in the RMS pressure fluctuations. This is not only true at the mid-channel, but also near the wall. Next to this, it was found that the method of eq. (5.8) also underestimates the correct value for l_e near the wall. This can be seen in appendix A.1. However, the method of Shur et al. leads to a larger underestimation.

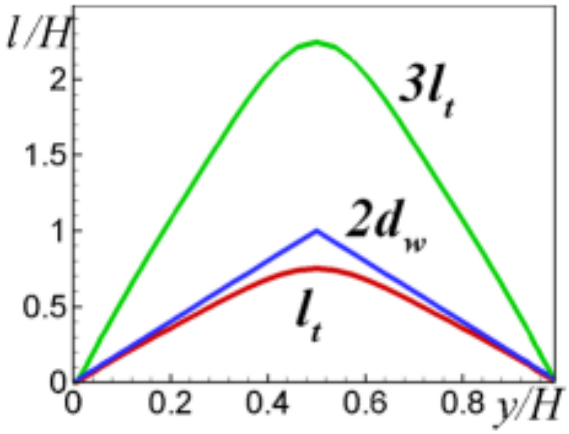

Figure 6.20: The different length scales for channel flow, taken from Shur et al. [9]

This underestimation can be seen when comparing fig. 6.21a with fig. 6.21b. As can be seen, the lower wavenumbers are especially underrepresented. As found in section 6.2.4, the lower wavenumbers have a significant impact on the pressure fluctuations. This is very noticeable when comparing fig. 6.22a with fig. 6.22b. With the length scale used by Shur et al., the pressure fluctuations are very underestimated for the lower wavenumbers, and overestimated for higher wavenumbers. While the method from eq. (5.8) still underestimates l_e, it shows quite good results for the pressure spectrum. The reduction in magnitude for higher wavenumbers is predicted, as well as the relative magnitude of the lower wavenumbers.

Next to the eddy length scale, there were also different options for the cut-off length scale. Namely, the cubic-root-volume method and the method of Shur et al. [9]. The determination of the cut-off length scale is important as it determines how much energy of the energy spectrum is resolved. However, this task is not trivial, as the cut-off length and the energy spectrum are represented with scalars, whereas in reality the cut-off

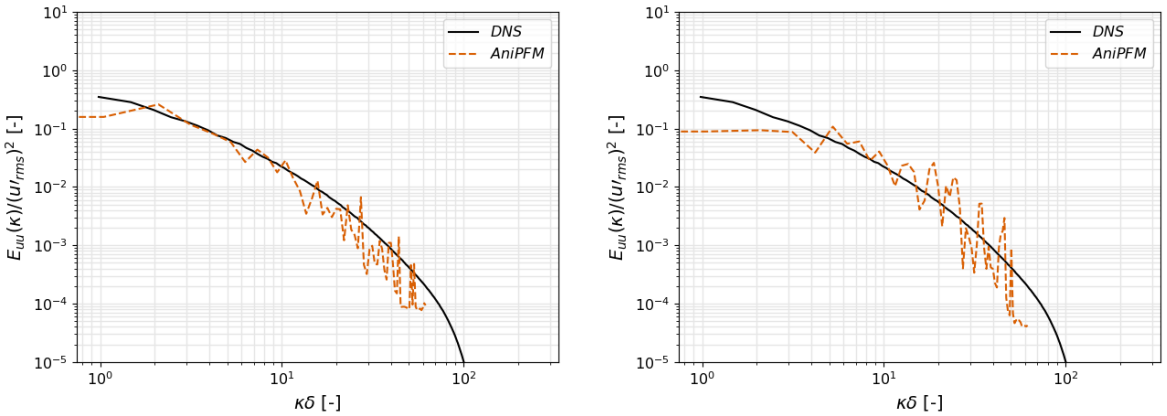

(a) l_e as defined in eq. (5.8)

(b) l_e as defined by Shur et al. [9]

Figure 6.21: The energy wavenumber spectrum with different definitions for l_e, at $y^+ = 300$.

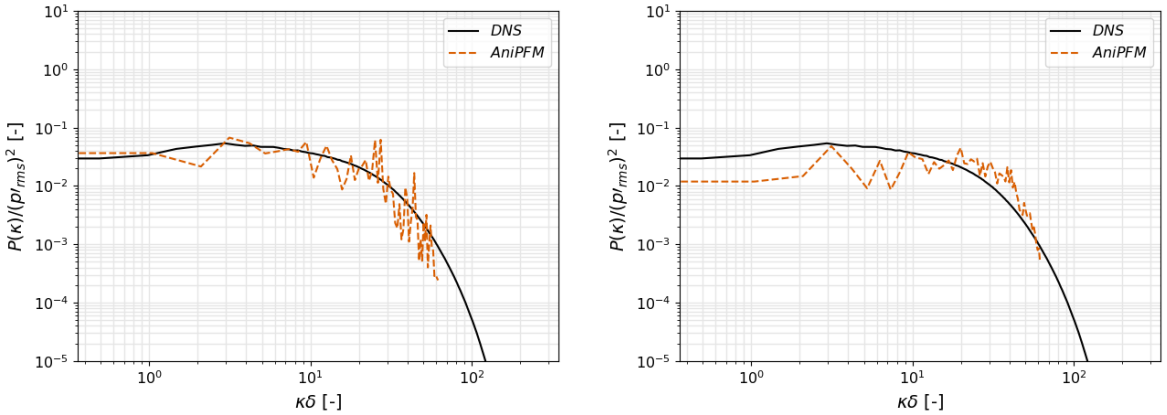

(a) l_e as defined in eq. (5.8)

(b) l_e as defined by Shur et al. [9]

Figure 6.22: The streamwise pressure wavenumber spectrum with different definitions for l_e, at $y^+ = 10$

length varies in three dimensions. This is most noticeable in areas where the mesh is highly anisotropic, such as near the wall. Namely, at the wall, the cell height in the wall-normal direction is much smaller than the length in the span- and streamwise directions. Thus, a much smaller cut-off length could be used in the wall-normal direction than in the span- and streamwise direction. If the cut-off length of the wall-normal direction was used, the resolved energy in the span and streamwise direction would be overestimated, whereas if the cut-off length of the span- or streamwise direction would be used, the resolved energy in the wall-normal direction would be underestimated. For this reason, it is recommended that in the future, a pressure fluctuation model should be researched where the velocity fluctuations are defined by three separate one-dimensional energy spectra, such that the energy in each spatial direction can be captured accurately.

An example of the cut-off length for the different methods is shown in fig. 6.23. As can be seen, the cubic root method gives a cut-off length more than twice as small as Shur et al.'s method (eq. (4.44)), near the wall. Near the mid-channel the values are closer, as the mesh cells are less anisotropic. From this, it can be expected that the RMS pressure fluctuations will be lower when using Shur et al.'s method, as less energy is resolved. The differences in the captured energy are quite large for the cubic-root-volume method and Shur et al.'s method. This is noticed in the root-mean squared pressure fluctuations, which are shown in fig. 6.24. For this simulation, the $80x128x60$ mesh was used, with 1024 wavenumber modes. As can be seen, the method of Shur et al. shows much lower RMS pressure fluctuations than the cubic-root-volume method on the same mesh. Interestingly, it also shows a very fine approximation of the pressure spectrum at $y^+ = 10$, as shown in fig. 6.25.

From this analysis, it was shown that the choice of cut-off length has a large effect on the amount of

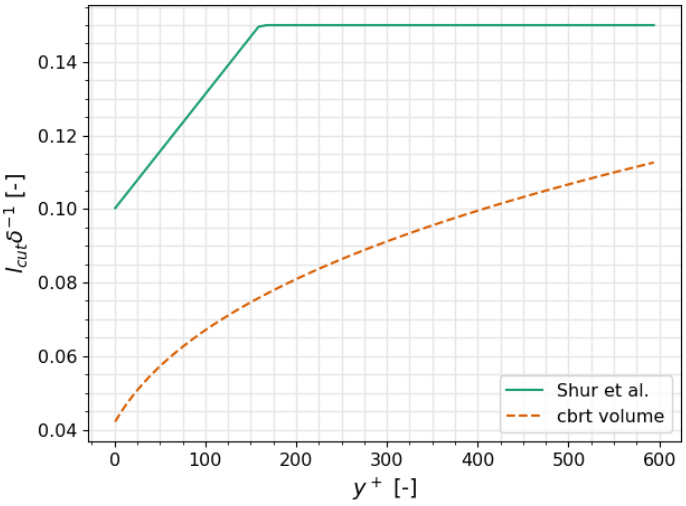

Figure 6.23: The cut-off length for both the cubic-root-volume and Shur et al.'s method, given a $80x128x60$ mesh.

energy that is resolved, and thus also on the RMS pressure fluctuations. However, it is not clear which method is better, as the actual cut-off length is not known. For this reason, the effect of the cut-off length on the RMS amplitude of a vibrating fuel rod is investigated in chapter 7. While it is expected for the RMS pressure fluctuations to differ on coarser meshes, it is expected to converge to a single value for finer meshes, as this would mean that the pressure fluctuations are fully resolved. However, even for the finest mesh, a discrepancy can be found between the two methods. On the mesh that was used in section 6.2.4, the AniPFM with Shur et al.'s cut-off length shows only -4.4% error with respect than the DNS results, for the root-mean-squared pressure fluctuations. When using a URANS model, it showed an error of roughly +10% w.r.t. the DNS results, showing closer results than with the cubic root cut-off method.

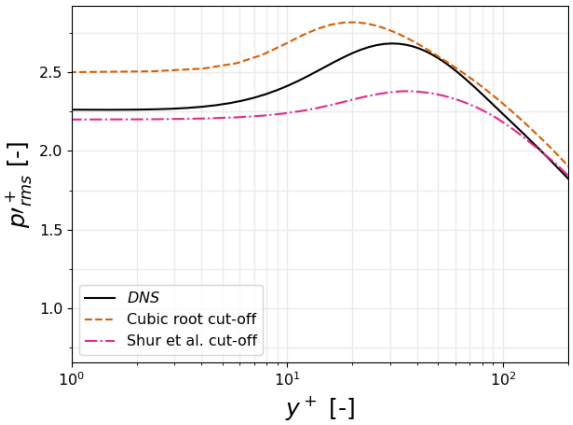

Figure 6.24: The RMS pressure fluctuations with different cut-off length definitions, compared to the DNS data of Gotoh et al. [12].

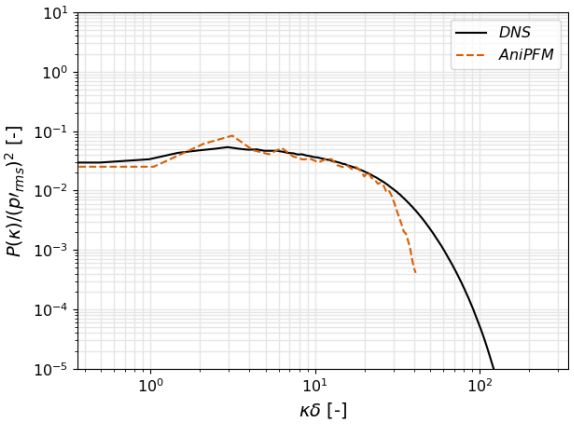

Figure 6.25: The streamwise pressure spectrum of AniPFM with the cut-off filter defined by Shur et al.[9], compared to the DNS data of Gotoh et al. [12].

6.2.6. Inlet/Outlet Boundary conditions

To solve the pressure fluctuation equation eq. (3.31), boundary conditions are necessary around the domain. In the HIT and channel flow case, most boundaries could be set by using periodic boundaries. However, in other cases this is not necessarily true. For this reason, the other boundary condition options are evaluated in this subsection. The main reason why this is done is because the pressure fluctuations equation requires a realistic boundary field in order to give realistic pressure fluctuations. Thus, the boundaries can not be set to a fixed uniform value such as with typical URANS variables.

In section 5.2.2, the possible options for inlet/outlet boundary conditions were given. It was recom-

mended that only fixed value boundary conditions were used, as opposed to fixed gradient boundary conditions. For this reason, only the periodic condition, the mapped condition and the calculated condition (the condition where eq. (5.27) is used) are compared, for the inlet and outlet. This is done on a $40x64x30$ grid, with 256 wavenumber modes, and with DNS data as URANS input.

In fig. 6.26, the RMS pressure fluctuations for the the different boundary condition types are shown. It can be seen that there is a miniscule difference between the different boundary condition types. In fact, the values at the wall are within a range of ±0.098%, whereas the uncertainty of the periodic case is equal to ±0.11%. From this, it can be concluded that the different methods give the same statistical results, and thus these methods are valid to use for future simulations. In particular, the calculated boundary condition is recommended. This is because for the mapped boundary condition, the location that is mapped must be chosen by hand, and this location must have the same mean flow variables as the inlet or outlet in order for the mapping to be accurate. With the calculated boundary condition, this is not the case, thus it is easier to use and less error prone.

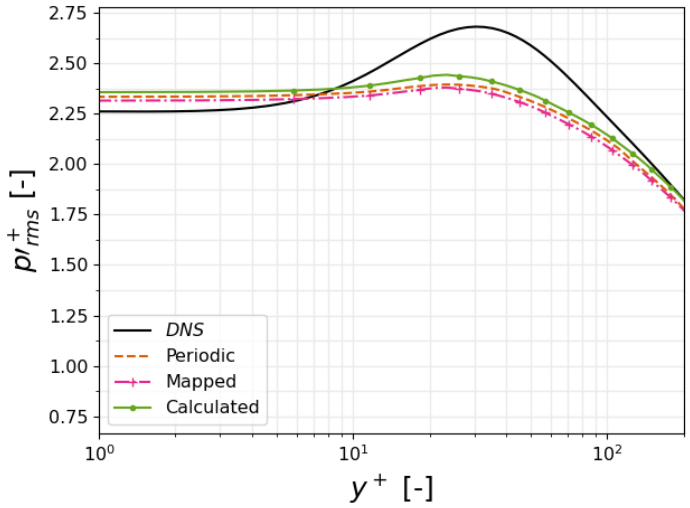

Figure 6.26: The RMS pressure fluctuations for various inlet/outlet boundary conditions.

6.2.7. Time Correlation

In section 5.1.3, four different methods were elaborated upon that could be chosen to introduce time correlation into the velocity fluctuations. In this subsection, the methods are evaluated based on the RMS pressure fluctuations, the Reynolds stresses, and the pressure frequency spectra. All simulations have been carried out with a mesh of $80x128x60$, with 1024 wavenumber modes, and the same seed number for the random number generator. As this is purely about the time correlation, and not other impending factors, the DNS Reynolds stress and velocity profiles are used as input "URANS" solution. First, the replicated Reynolds stresses are discussed, which are then linked to the RMS pressure fluctuations. Finally, the pressure fluctuation spectra are evaluated.

In fig. 6.27, the Reynolds stress profiles are shown for the different time correlation methods. Several of the effects of the methods that were mentioned in section 5.1.3 can be seen. In fig. 6.27a, it can be seen that the turbulent kinetic energy is not approximated as good when using both C&EC as in the pure convection case. This is due to the numerical diffusion that is introduced by solving for the convection equation. In fig. 6.27b, it can be seen that the rescaled velocity fluctuations follow a different profile than the prescribed profile, with a slightly higher prediction in the mid-channel than the pure convection case, and a slightly lower prediction near the wall. This is because the fluctuations are rescaled with the total lost energy, but the amount of lost energy varies over the channel height. However, as can be seen, the prediction of the Reynolds stresses near the wall is actually better than for the C&EC case. Because of the loss of energy in the convection and exponential correlation case, it is expected that the RMS pressure fluctuations will also be underpredicted, with respect to the pure convection case. In the case of the Rescaled Convection & Exponential Correlation (RE&EC) method, it is expected that the results near the wall will be close to that of the pure convection method, but near the mid-channel it is expected that the RMS pressure fluctuations will show a

slight overestimation.

Using pure exponential correlation or pure convection, the Reynolds stress profiles are slightly underestimated, as shown in fig. 6.27c and fig. 6.27d, respectively. It is noticed that the reproduced Reynolds stresses in fig. 6.27d clearly follow the same profile as the prescribed input, and only the magnitude is different. The same holds for the pure exponential correlation case. Note that while the pure exponential correlation and pure convection methods have no loss in energy due to diffusion, the Reynolds stresses are not exactly met. This is because not all energy can be resolved on the grid used for these simulations. From section 6.2.4 it was found that the RMS pressure fluctuations can be approximated within 10% with the AniPFM using pure convection. As the Reynolds stress profiles in the pure exponential correlation case are very similar to those of the pure convection case, it is expected that the RMS pressure fluctuations will also not differ by much.

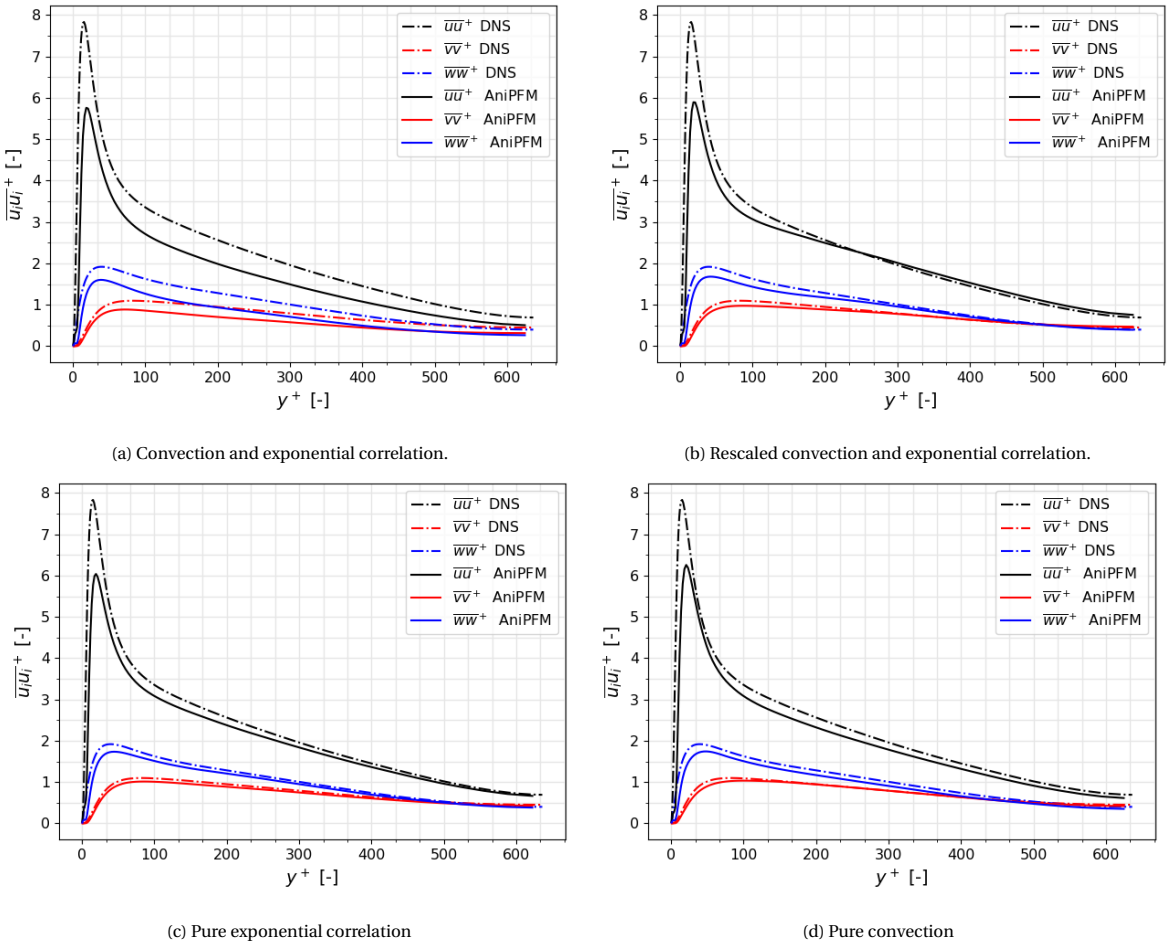

(a) Convection and exponential correlation.

(b) Rescaled convection and exponential correlation.

(c) Pure exponential correlation

(d) Pure convection

Figure 6.27: Reynolds stress profiles for different methods of time correlation.

In fig. 6.28, the RMS pressure fluctuations for the different time correlation methods are shown. As can be seen, the predictions based on the Reynolds stresses were quite correct. Indeed, the RMS pressure fluctuations in fig. 6.28a show an underprediction near the wall w.r.t. the other methods, due to dissipated energy of the flow. The rescaled case shows quite close results near the wall, but nearing the mid-channel the RMS pressure fluctuations are slightly overpredicted, similarly to the Reynolds stresses. The RMS pressure fluctuations using pure exponential correlation are quite similar to the pure convection case. In conclusion, the different methods for time correlation can affect the replication of the Reynolds stresses, and this translates to differences in the RMS pressure fluctuations. It is also noted that the time correlation methods do not have a direct effect on the RMS pressure fluctuations.

In fig. 6.29, the pressure frequency spectra are shown for the different time correlation methods. The frequency spectrum can be computed similarly to the wavenumber spectrum as shown in eq. (6.3), except now, the frequency domain is used, not the wavenumber domain. To do this, the pressure is sampled at a given location with a certain constant frequency. This procedure is done for a plane of points, from which

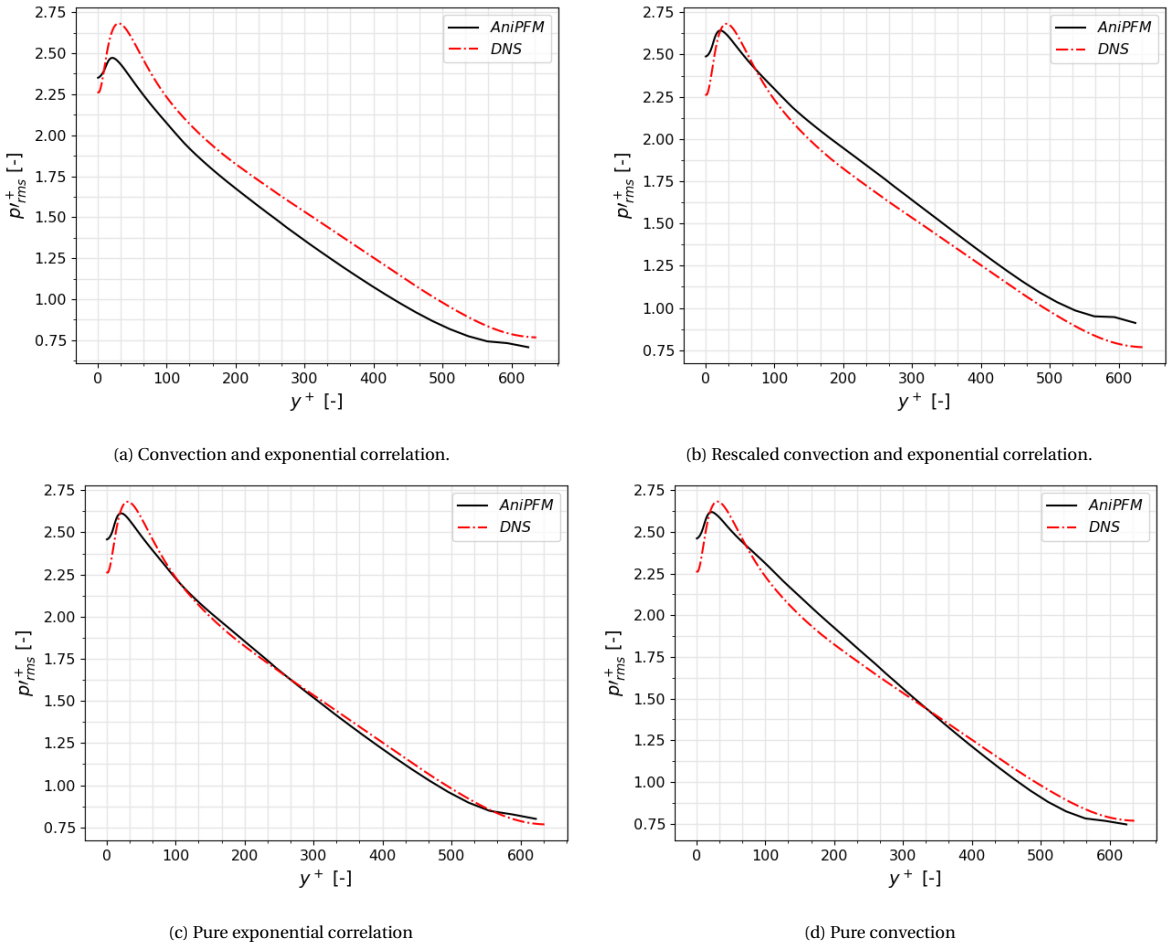

(a) Convection and exponential correlation.

(b) Rescaled convection and exponential correlation.

(c) Pure exponential correlation

(d) Pure convection

Figure 6.28: RMS pressure fluctuation profiles for different methods of time correlation.

the average is taken. From Abe et al. [13], no data was available for the frequency spectrum. Instead, the data was taken from the DNS data of Hu et al. [127] and the experimental data of Brungart et al. [128], similarly to previous work in NRG [102].

In order to match the DNS data and the experimental data, the frequency spectra were evaluated at $y^+ = 10$, which gave a value of $Re_\theta \approx 800$, where θ is equal to the momentum thickness. The experimental data from Brungart et al. [128] was obtained from a channel flow case at $Re_\theta = 1120$, so this is not exactly matched. However, For this range of Reynolds numbers it was found that the pressure spectra collapse to a single spectrum if properly non-dimensionalised. This is also the case for the DNS data of Hu et al. [127]. This simulation was performed at $Re_\tau = 720$, whereas the shown simulations were performed at $Re_\tau = 640$. Again, the frequency spectra overlap with the correct non-dimensionalization.

To understand the results in fig. 6.29a and fig. 6.29b, first fig. 6.29c must be examined. In section 6.1.3, it was found that the exponential time correlation method gave substantially better results than the previous PFM in terms of time correlation for the velocity fluctuations. However, in fig. 6.29c it can be seen that the frequency spectrum is not accurately represented with the exponential time correlation. This is because the exponential correlation is based on the decay of homogeneous isotropic turbulence, and a general modification factor was used, instead of a fine-tuned factor. Because of this, it shows an overestimation at the lower frequencies, and an underestimation at the higher frequencies. This effect is carried over to the C&EC case, and the rescaled case as well. However, due to the added convection, the over- and underprediction is reduced, but, all three methods do not show the characteristic drop-off in intensity around $2 \cdot 10^{-1} \cdot 2\pi f \nu / u_\tau^2$. Finally, the pure convection case, shown in fig. 6.29d seems to be much more spurious. This could be due to the lack of variation in the random numbers input. It does follow the DNS data quite well, but also this method can not fully predict the previously mentioned drop-off near the higher frequencies.

In conclusion, the different time correlation methods show only small differences in the RMS pressure

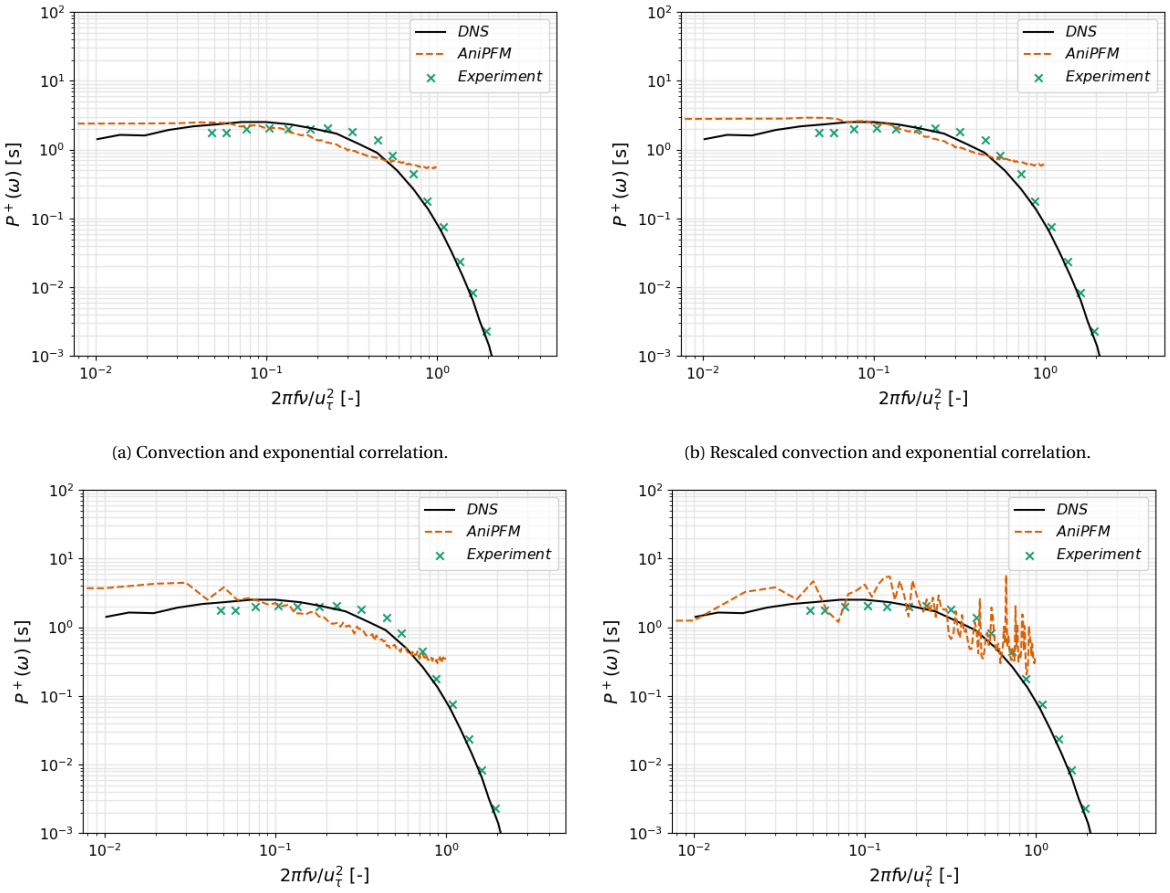

(a) Convection and exponential correlation.

(b) Rescaled convection and exponential correlation.

(c) Pure exponential correlation

(d) Pure convection

Figure 6.29: Pressure frequency spectra for different methods of time correlation.

fluctuations and the pressure frequency spectra. The most notable differences are that the C&EC case shows lower values for the RMS pressure fluctuations compared to the other methods, and the pure convection case shows more spurious results in the frequency spectrum. From these tests, it seems that the rescaled convection and exponential correlation method and the pure convection method produce the best results, in the FSI cases the effect of these methods on the RMS amplitude is evaluated. Note that while the pure convection method gives good results for the frequency spectrum, it was also found that this method has a larger uncertainty than the convection and correlation method, since only one set of random numbers is used throughout the simulation.

6.2.8. Computational Resources Evaluation

The main goal of the AniPFM is to use it in combination with URANS for fluid-structure simulations of nuclear fuel rods. The motivation is that LES simulations are typically computationally too expensive to use for these cases, due to the strict mesh requirements. Thus, for the AniPFM to be actually successful, the computational resources must still be in the order of magnitude of typical URANS simulations. For this reason, several simulations were timed and evaluated for the time spent on URANS and AniPFM calculations.

For these simulations, a mesh of $35x64x25$ is used, with the base case having 128 modes, and the pressure fluctuation equation is solved up to a residuals level of $1e-6$. In table 6.6, the relative resource allocation for several use-cases is shown. Each case is run three times, and the averages are reported. The resource allocation of the AniPFM is divided into the generation of the velocity fluctuations and the subsequent calculation of the pressure fluctuations. Here, the min. iterations case uses optimized settings in the solver for the pressure fluctuation equation, in order to minimize the number of iterations necessary.

Table 6.6: The relative resource allocation during an AniPFM+URANS simulation, for different use-cases.

	128 modes	**256 modes**	**1024 modes**	**Min. Iterations**
u' generation [%]	42.9	47.0	68.5	35.3
p' solving [%]	28.8	27.8	17.5	27.6
URANS [%]	28.3	25.2	14.0	37.1

As can be seen, the total simulation time (including URANS) can be anywhere from 2.7 to 7.1 times as long as the typical URANS time. However, the typical time is roughly 3.5 times as long as the typical URANS time. Given these values, the AniPFM would thus be effective if the equivalent LES mesh for the case is more than 3.5 times as large as the URANS mesh, which is typically the case. Thus, these values indicate that the AniPFM could indeed be a viable alternative to LES, given that the results of the AniPFM are within the required error-margin. However, these values are only an indication based on a simple geometry. Since the AniPFM is only turned on after the URANS simulation has converged to steady state, the number of URANS iterations are significantly smaller than they would be in an actual unsteady case. Thus, in case of an unsteady case, it could be that the increase in time due to the AniPFM is smaller than indicated in table 6.6. For this reason, another evaluation is done with a fluid-structure interaction case, as shown in chapter 7.

From this study on computational resources, a few recommendations emerged regarding the computational set-up of a URANS + AniPFM problem. When generating the velocity fluctuations, the number of modes logically have a large effect on the total computational time. However, in section 6.2.4, it was found that increasing the number of modes only has a small effect on the RMS pressure fluctuations, compared to other error sources. Thus, it is recommended to use an amount of modes that is on the lower end of the tested values. For the pressure fluctuations, it was found that the quality of the mesh had a very large impact on the number of iterations needed for solving eq. (3.31). In particular, the aspect ratio of the cells has a very large impact, with larger aspect ratios causing the solver to need more iterations in order to converge. This is something to take in consideration when generating the mesh.

6.2.9. Summary

In this section, the channel flow case was discussed. In particular, the results of the AniPFM for various meshes and settings were investigated. It was found that given the correct mean flow characteristics, the AniPFM could correctly estimate the RMS pressure fluctuations with an error of less than 10%. When using the $k-\omega$ SST model with the Wilcox correction, an additional error of roughly 15% is found. This is mainly due to the differences in the Reynolds stresses, especially in the wall-normal component. There was also certain uncertainty in the results, that was caused by the use of random numbers, and due to the slowly varying nature of the RMS pressure fluctuations. All errors and uncertainties are summarized in table 6.7. In order to give an overview, the flowchart as presented in chapter 5 is repeated in fig. 6.30, with indicators where the various errors originate from. Note that the pressure fluctuation equation also brings an uncertainty error, but this error is mesh dependent. Furthermore, this error is not exactly known because this error can not be separated from the error that originates from under-resolving the domain.

Table 6.7: All evaluated errors and uncertainties of the AniPFM, with respect to the DNS data of Gotoh et al.[12].

	Error/Uncertainty [%]
Model Error	4.4-9.22
URANS Error	14.0
Time uncertainty	0.1 [1]
Randomness uncertainty (pure convection)	2.86
Randomness uncertainty (convection and correlation)	0.24

Certain modelling choices also affected the outcome of the AniPFM. The choice for both the cut-off length and l_e can influence the results. In the case of determining l_e, it was clear that using the relation from eq. (5.8) gave superior results. However, for the cut-off length scale, this was not clear, and the effect of this parameter is tested in the FSI cases in chapter 7. In both cases, the wavenumber spectrum of the AniPFM closely matched that of the DNS data of Gotoh et al. [12]. The effect of using different boundary conditions was

negligible. However, the method for time correlation did affect the outcome of AniPFM, mainly in terms of the frequency spectrum. The difference caused by these methods is also evaluated in chapter 7.

It was found that the increase in the necessary computational resources for the AniPFM is limited to roughly 2.7-4.0 times that of the URANS simulation, given that the number of wavenumber modes is chosen wisely. This, together with the given accuracy range, in terms of the RMS pressure fluctuations and the wavenumber/frequency spectra, gives a positive perspective on the applicability of the AniPFM for FSI simulations of nuclear fuel rods in axial flow.

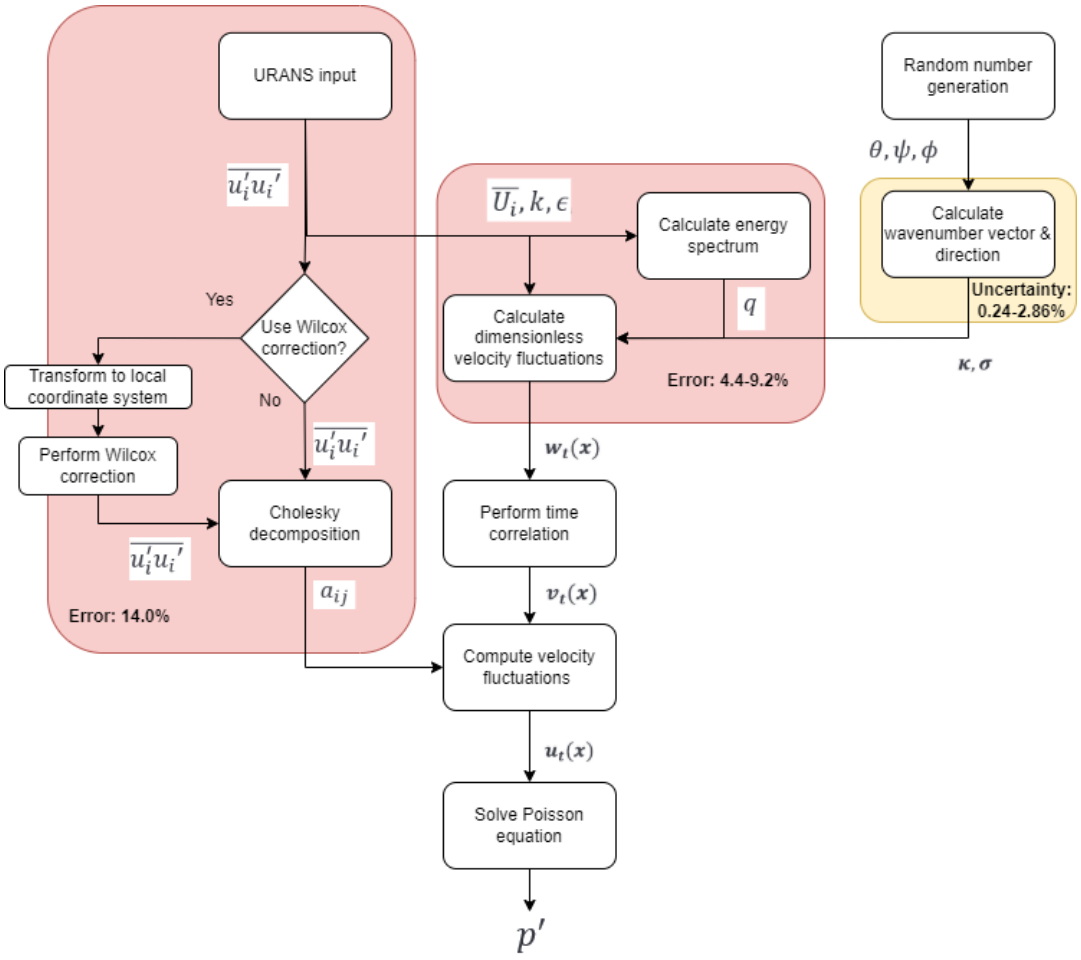

Figure 6.30: A flow-chart of the different computational steps of the proposed AniPFM, with the sources of the various errors, for turbulent channel flow.

[1] This is a typical value, the actual value differs for each simulation.

7

Flexible Brass Beam in Turbulent Water

The results from chapter 6 gave confidence in the capabilities of the AniPFM to model turbulent pressure fluctuations, which also gave an optimistic outlook for fluid-structure interaction simulations. In this chapter, this is put to the test by performing an FSI test case. The test case is a flexible brass beam in turbulent water, which was chosen due to the vast comparison material available and the relatively simple set-up. The displacement history and RMS values, as well as the vibration frequencies, are investigated. In this chapter, first, the set-up of previous physical and numerical experiments of the brass beam in water, and the current simulation set-up are elaborated upon. After this, several simulations are discussed. Namely, first a pure URANS-FSI approach is discussed; after this, the results of the AniPFM are evaluated. Finally, an AniPFM-FSI approach is used, and the results are compared to the experiment.

7.1. Experimental & Previous FSI Set-ups

Chen & Wambsganss [15] performed an experiment of a flexible brass beam in turbulent water, which has subsequently often been used as a validation case for FSI problems with applications to nuclear fuel rods [14, 16, 17]. This is due to its simple geometry, and because it permits comparison with other simulations as well. Moreover, the experiment established both data about the modal frequencies for several flow cases, and the root-mean-squared vibration amplitudes. The flexible brass beam is enclosed in a rigid steel cylinder, and it is clamped on both sides. The discretized geometry as used by Kottapalli et al. [14] is shown in fig. 7.1. The diameter of the brass beam is $D_c = 0.0127m$, the enclosing cylinder has a diameter of $D_o = 0.0254m$, and the beam has a length of $L = 1.19m$. This gives an L/D-ratio of 93.7. The level of turbulent intensity and the turbulent length scale at the inlet of the domain were not mentioned by Chen & Wambsganss [15]. Several studies [14, 16, 17] assumed a turbulence intensity of 5% and a turbulent length scale of 0.1 cm. The experiment was conducted for various mean inlet velocities, in the range of 8-33 m/s. This gives a range of Reynolds numbers from 101,600-419,100. The rod has a density of 8400 kg/m^3, giving a density ratio of $\frac{\rho_s}{\rho_l} = 8.4$. The Poisson ratio was not mentioned in the experiment, but a nominal value of 0.33 was taken, based on previous simulations [14]. Finally, a Young's modulus of $E = 107GPa$ was specified [15].

De Ridder et al. [16] simulated the experiment through means of an FSI simulation, where an initial displacement was given to calculate the natural frequency of the fundamental mode. In the simulation, a partitioned approach was taken, where the fluid dynamics were solved through a URANS $k-\omega$ SST turbulence model. The structural mechanics were solved through Abaqus 6.10, a finite element solver. The solvers were coupled through the IQN-ILS method, where the Jacobian was approximated based on previous iterations. Interestingly, it was found that the finite element solver accounts for less than 1% of the computational time. De Ridder et al. [16] computed the modal frequencies for all three flow cases, both with no pre-stress and with a pre-stress of $648N$ added. The modal frequencies were found to be within 4.5% of the experimental frequencies. With the added pre-stress, this was lowered to 3.5%, however, no pre-stress is mentioned in the original experiment [15]. The simulations were performed at 10, 20 and 30 m/s.

In addition, De Ridder also performed wall-resolved large-eddy simulations of the same set-up [18]. These simulations were purely LES, so no fluid-structure interaction was modelled. However, the root-mean squared amplitude of the beam was calculated by computing the force spectrum from the LES data, and using this with an analytical relation that was introduced by Chen & Wambsganss [15]. The simulations were performed

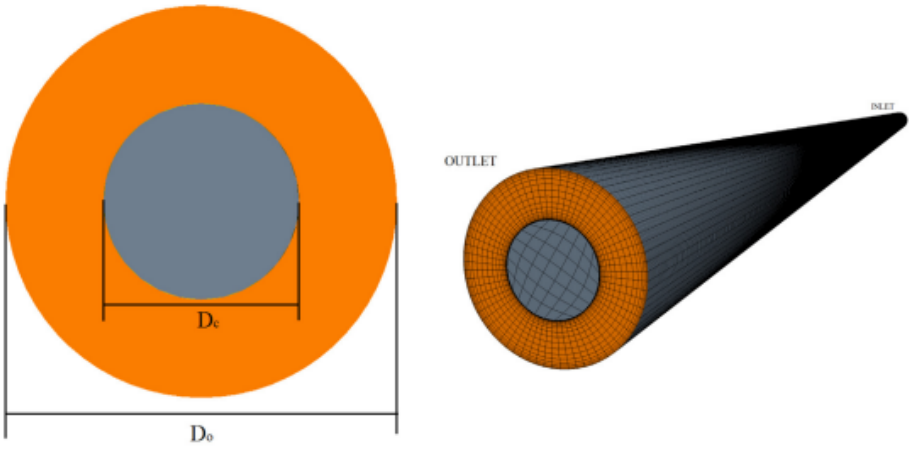

Figure 7.1: Discretized geometry of Kottapalli et al. [14], representing the experiment of Chen & Wambsganss [15].

on a rod with a smaller total length, in order to reduce the required computational power. From a mesh study, De Ridder concluded that with a mesh of 76.8 million cells and a length over diameter ratio of 10, the mean flow velocity and the force spectrum were converged. Extrapolating this to the full length of the beam means that the mesh would have had 720 million cells. These simulations were solely performed at 10 m/s.

Kottapalli et al. [14] used a similar approach to that of De Ridder et al. [16]. Similarly, a partitioned approach was taken, where the IQN-ILS coupling method was used to couple a URANS $k-\omega$ CFD simulation with a finite element structural solver. However, in addition to simulation with a given initial displacement, Kottapalli et al. [14] also simulated the rod without a given initial displacement, but with a pressure fluctuation model to provide the excitation. This was done at 10 m/s as well.

Finally, Nazari et al. [17] simulated the experiment with a partitioned approach, using both URANS and LES for the calculations of the fluid domain. The fluid domain was modelled with the $k-\omega$ SST turbulence model for the URANS case, a finite element solver was used to solve the structural domain, it is not clear what coupling method was used. In the case of the LES simulation, the Dynamic Smagorinsky-Lilly model is used to model the sub-grid stress tensor.

7.2. Current Simulation Set-up

The current configuration is quite similar to the previous cases. The geometry is kept the same, and again a turbulence intensity of 5% and a turbulent length scale of 0.1 cm are assumed. De Ridder et al. [16] found that these quantities did not have a large effect on the results [16] for URANS simulations. From preliminary tests, this was confirmed. The flow is fully developed for the majority (roughly 90%) of the domain, and here the kinetic energy profiles are independent of the inlet conditions. This also holds for the pressure fluctuations, in the developed flow region, they are shown to be independent of the kinetic energy at the inlet. Only near the inlet is a variation noticeable; however, the impact of this region on the structural vibration is hypothesized to be considerably less than the developed flow region of the domain.

Several authors [14, 16, 17] have simulated the case with a uniform inlet velocity, and in the current setup this is also the case. This set-up has been chosen in order to match previous simulations. However, from the original article of Chen & Wambsganns [15], it is not clear how accurate this assumption is. The flow enters the test-section through a V-shaped channel, but it is not clear what the effect of this is on the uniformity of the flow at the inlet. In section 7.3, the possible effect of this assumption on the quantities of interest is investigated.

The outer steel cylinder is kept rigid, whereas the inner brass beam is modelled as a moving wall. The brass beam is clamped at both ends, and it is assumed that the beam can be modelled with a linear elastic solver. For this, the relative displacements must be $\frac{A_{rms}}{L} << 1$, which can be found to be true based on the displacement values from the experiment of Chen & Wambsganss [15].

For the CFD side, URANS is used with the $k-\omega$ SST model. Contrary to previous simulations, these simulations are resolved up to the wall, which means that finer grids are necessary. An example of a mesh is shown in fig. 7.2, along with the used axis convention. Several fluid meshes are used to compare the results to the experiment and the simulations from previous papers. In these meshes, the axial and radial elements

are varied to study its effects. The discretization in the tangential direction is fixed to 40 cells, which was found to be sufficient from a preliminary mesh study of pure CFD calculations. For the structural mesh, quadratic elements are used. From a preliminary mesh study, documented in appendix A.2, it was found that the results were converged for a structural mesh that has 25 elements in the x-y plane, and 50 elements in the axial direction. For both the solid and the fluid models, a second-order time scheme is used.

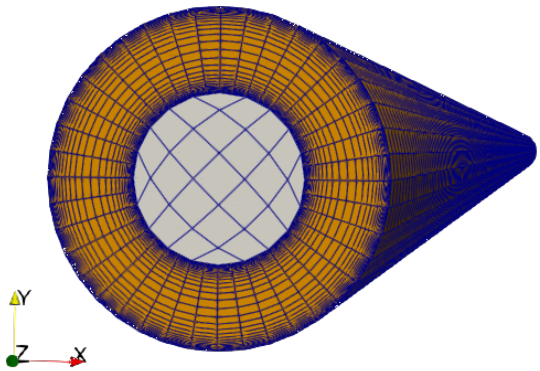

Figure 7.2: Discretized geometry of the brass beam case, representing the experiment of Chen & Wambsganss [15].

Due to the small density ratio, an implicit coupling scheme is used, namely IQN-ILS. In regard to mapping, local radial basis functions are used. These are used because due to the quadratic elements, the structural mesh in the axial direction is quite coarse, thus a higher-order mapping method is necessary. It was found that global radial basis function take too much computational effort for fluid grids with more than 32,000 interface faces, thus local radial basis functions are used. It was found that by using a support radius that encapsulates 5 elements of both the fluid and the structural mesh, the difference in FSI results is negligible in comparison to global radial basis functions, while severely reducing the computational costs.

An FSI calculation is done with a purely URANS approach for an inlet velocity of 10 m/s. This calculation serves as validation of the set-up with respect to the results from previous papers. For this calculation, the brass beam is subjected to an initial distributed force for 0.015 s. This is the excitation mechanism, because without pressure fluctuations, the rod would not vibrate.

Next to this, FSI calculations are done with a URANS + aniPFM approach. These calculations are done for 10, 15 and 20 m/s, with several meshes, as well as several aniPFM settings. For these simulations, 256 modes are used, with a maximum wave length equal to the spacing between the brass beam and the surrounding steel cylinder. Pure convection is used as time correlation in the initial grid study, however other time correlation methods are also investigated. Similarly, the cubic-root cut-off method is used, but the method of Shur et al. [9] is also investigated. For the pressure fluctuations, eq. (5.28) is used as boundary condition for the in- and outlet. The velocity fluctuations are mapped to the inlet, and they have a zero gradient outlet condition. Finally, the Wilcox correction is also used. These settings are summarized again for all fluid-structure interaction simulation in section 7.5.

7.3. Results of the URANS FSI Simulation

As mentioned in section 7.2, the URANS FSI simulation only serves to verify that the FSI set-up, i.e., the mapping method, the structural mesh and boundary conditions, and the coupling algorithm, are correct. This is done by verifying that the FSI simulation can accurately predict the fundamental natural frequency. For this reason, the simulation is done solely for the case with a mean inflow velocity of 10 m/s. However, it was noticed that in previous articles, solely a wall-modelled approach was taken. In this thesis, a wall-resolved method was chosen. As it was expected that this could influence the results, a wall-modelled simulation was also performed in order to compare the results. Since in this section, it is purely about verifying the FSI set-up, only simulations with a similar set-up are compared. For example, the LES results of Nazari et al. [17] are

not compared in this section.

Due to the long legacy of the original paper of Chen & Wambsganss [15], articles often retrieve the experimental results indirectly, instead of through the original article. This is because the original article only exists online in less than ideal conditions. This has caused some discrepancies in the results over time, and for this reason, the original experimental results are retrieved from Chen & Wambsganss [15], and the figures for this particular case have been digitized.

The behaviour of an oscillating beam is known, and it can be represented with an exponentially damped sinusoid. In order to retrieve the natural frequency and the damping ratio, the displacements obtained from the FSI simulation are fitted to the function eq. (7.1). Here the natural frequency and the damping ratio can be obtained from eq. (7.2) and eq. (7.3), respectively. The displacement of the centre of the brass beam at $z = 0.595m$ for the wall-resolved simulations is shown in fig. 7.3. As can be seen, it indeed follows the exponentially damped sinusoid shape. The function shows to be a great fit, with the largest relative standard deviation of any fitting parameter being 0.044%.

$$D(t) = y(t) = A \cdot e^{-\lambda t} \cdot \cos(\omega t - \phi) + \psi \tag{7.1}$$

$$f = \frac{\omega}{2\pi} \tag{7.2}$$

$$\zeta = \frac{\lambda}{\sqrt{\lambda^2 + \omega^2}} \tag{7.3}$$

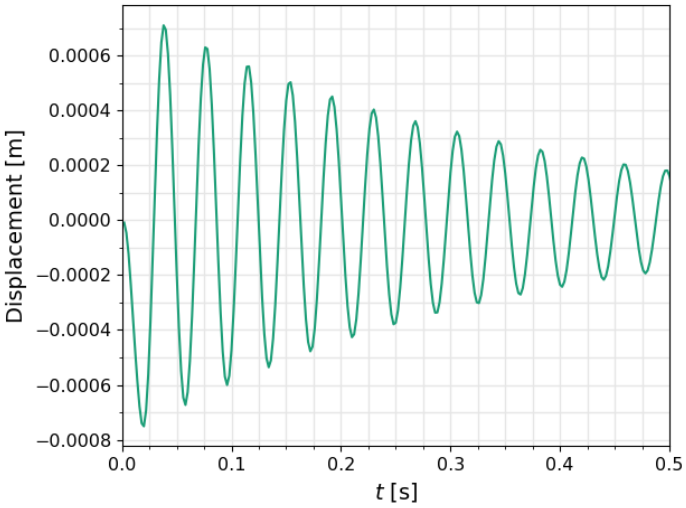

Figure 7.3: The displacement of the wall-resolved FSI simulation, at mid-beam, for 0.5 s of simulated time.

In fig. 7.4a, the fundamental natural frequency is compared with the experiment of Chen & Wambsganss [15], as well as other simulations taken from literature. Note that the non-pre-stressed data is taken from De Ridder et al. [16], in order to ensure a fair comparison. Furthermore, the experimental data from Chen & Wambsganss [15] is denoted by the dots, whereas the line shows the theoretical results. Note that the experimental data goes no further than 24 m/s for the frequencies, this is due to the fact that this data could not be retrieved from the original paper, due to the available quality. For other quantities however, there is data available up to 30 m/s. As can be seen from fig. 7.4a, the frequency is a close match to the experiments and the other simulations. There is an error of 5.7% w.r.t. the analytical value, and an error of 5.4% w.r.t. the closest experimental value. The results are comparable to other published results, within the error range of 3.6%-7.1% of the previous results. Furthermore, from an independent check, it was found that the results of Nazari et al. for a flow velocity of 10 m/s were closer to $f = 26.3Hz$ than the reported $f = 26.9Hz$, based on the published displacement figure.

In fig. 7.4b, the computed damping ratio is compared to the experiment of Chen & Wambsganss [15], as well as other simulations taken from literature. It was found that the results are similar to those of Kottapalli et al. [14], but it shows a large error with respect to the experiment of Chen & Wambsganss. It shows that the damping is overestimated by 28.6%. The same error was found for Kottapalli et al. [14].

As mentioned in section 7.2, a uniform inlet velocity was used as boundary condition, similar to other simulations replicating this experiment. There is however some uncertainty with how uniform the velocity

was in the experiment at the inlet of the test-section. It is likely that the inlet velocity was non-uniform, with a distribution profile inbetween a uniform and a fully developed profile. To quantify how much of an influence this could have on the natural frequency and damping ratio, the same simulation was done with the flow fully developed at the inlet. This gave a 0.045% difference in the natural frequency, compared to a uniform velocity inlet. However, it also gave a 2.92% reduction in the damping ratio, which is a significant discrepancy. In reality, the flow is onlikely to be fully developed at the inlet, thus the actual difference w.r.t. the experiment lies inbetween the two presented extremes. Thus, this does not fully explain the discrepancy between the currently performed simulations and the experiment.

The damping ratio found by De Ridder et al. is much closer to the experiment. A possible explanation for this is the used software packages for the FSI simulations. While De Ridder et al. used ANSYS for the fluid domain and Abaqus for the structural domain, the current simulations are done with OpenFOAM for the fluid domain and Deal.II for the structural domain. Kottapalli et al. saw a similar discrepancy in the damping ratio, and used the same software packages as the current simulations. Furthermore, Chouchoulis found that OpenFOAM coupled to Deal.ii also gave overprediction in damping ratios with respect to the same simulations performed in Star-CCM+[45]. From this, it seems that there is an inherent overprediction in damping when coupling OpenFOAM with Deal.ii through preCICE.

Thus, while the values for both the frequency and the damping ratio are consistent with results from other simulations taken from literature, it shows that there is a clear deficiency in the prediction of the damping ratio. The mesh dependency and time step dependency were investigated. It was found that both wall modelled and wall resolved approaches gave a similar frequency and damping ratio, and the given results were independent of mesh fineness and time step size, this is documented in appendix A.2. The final used mesh had a resolution of 50x40x400, with $y^+ \approx 1.1$ at the wall. Here, the mesh directions are stated in the Radial by Azimuthal by Axial convention. This means that there is a fundamental error, either due to URANS, or due to slight differences with respect to the experimental set-up. This error in the damping ratio can have a large effect on the subsequent simulations.

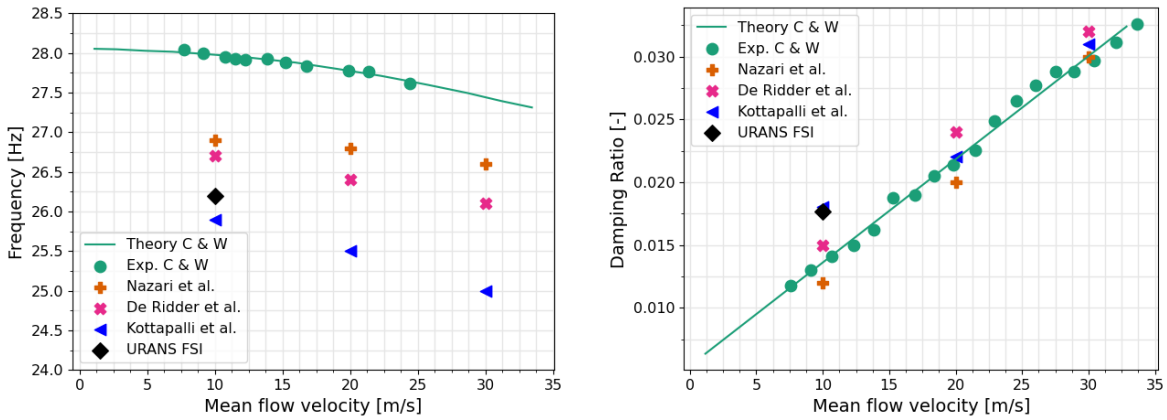

(a) Natural frequency.

(b) Damping ratio.

Figure 7.4: The calculated frequencies and damping ratios of the current work, compared to various simulations as well as experimental results. [14–17]

7.4. Results of the Pure AniPFM Simulation

Before simulating the fluid-structure interaction of the brass beam with the AniPFM, the brass beam is first simulated as a rigid structure. This is done to investigate the results of the AniPFM at higher Reynolds numbers than the channel flow simulations. The simulation is done with a mesh of 50x40x400. Due to its symmetry, the statistical results are axisymmetric. The profiles shown in subsequent figures are taken at mid-beam, and start at the inner wall, and end at the outer cylindrical wall. The width of the channel between the inner and outer wall is equal to 6.35 mm.

In fig. 7.5 the resolved Reynolds stresses are plotted versus the input Reynolds stresses. Note that the Wilcox correction is used. As can be seen, the Reynolds stress are far from fully resolved, this is due to the fact that grid size requirements for fully resolving the smallest length scales increase dramatically with increasing

Reynolds number. In fig. 7.6, the resolved turbulent kinetic energy is shown. At mid-channel, the energy is resolved up to roughly 65%, but the resolved energy goes down quickly towards the wall. The percentage of resolved energy near the wall is slightly lower than that of the coarsest channel flow mesh.

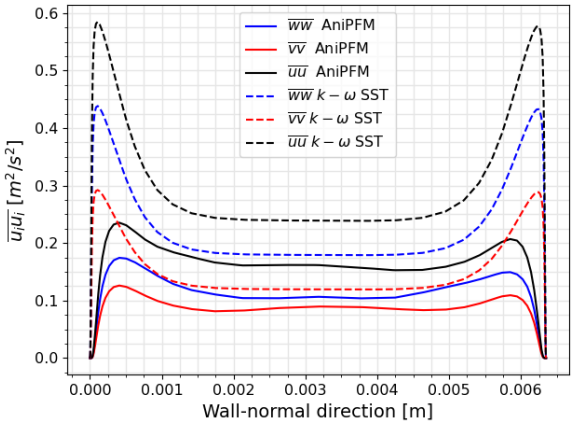

Figure 7.5: The URANS Reynolds stresses versus the AniPFM Reynolds stresses.

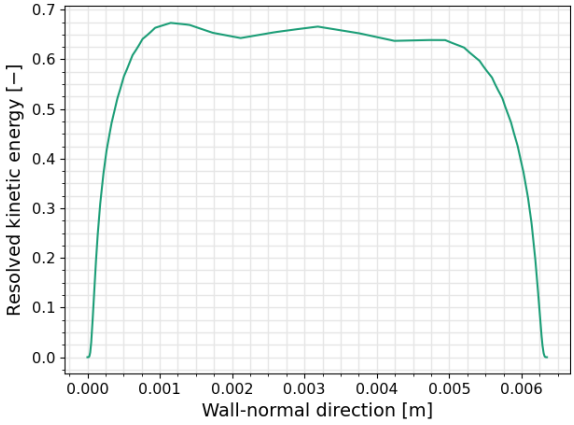

Figure 7.6: The ratio of resolved turbulent kinetic energy by the AniPFM.

A cut-out of the fluid domain at mid-beam is shown in fig. 7.7, presenting the root-mean-squared pressure fluctuations. It shows that the solution indeed converges to a symmetric steady-state result, similar to the channel flow. It also shows a similar pattern, with higher RMS pressure fluctuations near the walls than in the middle of the channel. The frequency spectrum of the pressure fluctuations at the inner wall is shown in fig. 7.8, where it is overlaid on the LES results from De Ridder [18]. The lower frequencies are of interest for the fluid-structure interaction simulations, as the natural frequency of the beam is with 27.9 Hz at the lower end of the spectrum.

Compared to the LES results, the pressure fluctuations at the lower frequencies seem to be overestimated. Furthermore, the AniPFM spectrum is not able to capture the increase that is shown in the LES results near the higher frequencies. However, such a peak was also not witnessed in experiments [18]. The pressure spectrum does agree nicely with the empirical spectrum of Wilson, which was based on experimental data of a similar set-up [129]. Furthermore, the spectrum shows lower values in comparison to the emperical spectrum of Chen & Wambsganns, which indicates that the RMS amplitude values predicted by the AniPFM will likely be lower than the values predicted by the analytical model of Chen & Wambsganns.

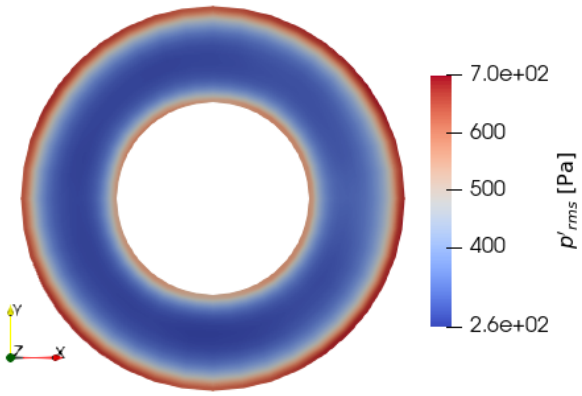

Figure 7.7: A cut-out of the fluid domain showing the root-mean-squared pressure fluctuations.

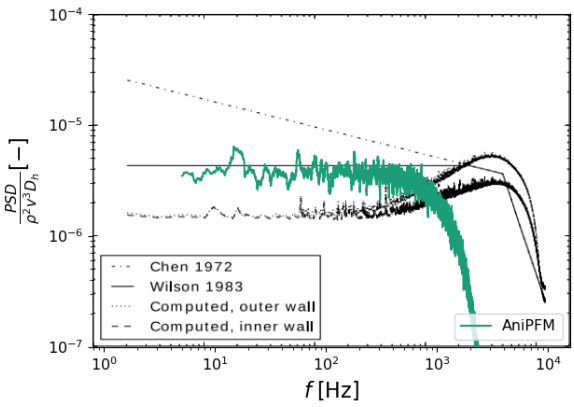

Figure 7.8: The frequency spectrum of the pressure fluctuations at the inner wall overlaid on the results of De Ridder [18], converted from the Strouhal number to frequency.

7.5. Results of the AniPFM FSI Simulation

From the previous results, it was found that the general FSI set-up is in line with previously published articles, and thus that the AniPFM could be added to this set-up. In this section, the results of the FSI simulations that have been done with the AniPFM are discussed. First, the effect of the different cut-off lengths are discussed, along with the effect of the different time correlation methods. After this, the mesh dependency is investigated. These simulations are only done at 10 m/s. Finally, the best set-up is chosen, which is applied to the 15 and 20 m/s testcases. A summary of the different AniPFM settings for all simulations of this section are shown in table 7.1. For all simulations, the $k-\omega$ SST model is used.

Table 7.1: The used AniPFM options for the various fluid-structure interaction simulations.

Mean Flow Velocity	Subsection	Nr. of modes	Time Correlation Method	Cut-off Method	Wilcox Correction
10 m/s	section 7.5.3	256	Pure Convection	Cubic-root	used
	section 7.5.1	256	Pure Convection	Both methods	used
	section 7.5.2	256	Pure Convection, C&EC and RC&EC	Shur et al.	used
15 m/s	section 7.5.4	256	Pure Convection	Shur et al.	used
20 m/s	section 7.5.4	256	Pure Convection	Shur et al.	used

7.5.1. Effect of Cut-Off Length Method

In section 6.2.5, it was shown that a different choice for the determination of the cut-off length, had a large influence on the root-mean-squared pressure fluctuations. The cubic-root-volume method gave a larger estimate, whereas the method by Shur et al. [9], gave a lower estimate. However, from the initial tests, it was not clear which cut-off length was the most suitable. For this reason, both methods are tested and compared to each other. For these cases, a pure uniform convection is used as time correlation, and a mesh of 50x40x200 is used for the simulations. This mesh in the radial direction was chosen because it was seen that a resolution of $y^+ = 1$ was needed at the wall, which is further elaborated upon in section 7.5.3. The mesh in the axial direction was chosen because this problem size still allowed fast simulation times, which gave a smaller uncertainty range in the obtained results.

The simulations for both methods are run for 8 seconds of simulated time, which is equivalent to roughly 70 flow-through times, and more than 200 fundamental periods based on the natural frequency. From these simulations, the results are processed, and various properties are calculated. In particular, attention is paid to the displacements of the centre of the beam, which is located at $x = 0, y = 0, z = 0.595\ m$. Next to this, the pressure fluctuations on the wall at the middle of the beam are also evaluated. In fig. 7.9a and fig. 7.9b the pressure fluctuations at the wall are shown for the simulations with the different cut-off methods. Note that the specific pressure fluctuations are displayed, i.e., $\frac{p'}{\rho}$. As can be seen, the pressure fluctuations for both cases look quite similar, however, the pressure fluctuations with Shur et al.'s cut-off length is slightly smaller. This is better evaluated by comparing the RMS pressure fluctuations. For the cubic root method, $p'_{rms} = 0.61$ $[m^2/s^2]$, whereas Shur et al.'s method gives $p'_{rms} = 0.52$ $[m^2/s^2]$, which is a difference of 14.8%. This is in accordance with earlier obtained results from section 6.2.5. Both methods show a moving average that is close to zero, indicating that the requirement of $\bar{p}' = 0$ is correctly enforced.

In fig. 7.10a the displacements in y-direction are shown for 0.5s of simulation time with the different cut-off methods. The different frequency modes of the brass beam can already be recognized. Furthermore, from this short period it is already hinted that the cubic-root cut-off method gives higher displacements. This is more clear from fig. 7.10b, where the amplitude-frequency spectrum is shown for both cut-off methods, over the whole simulated time. Here it can be seen that the cubic-root cut-off method produces higher amplitudes than the method of Shur et al. [9]. Apart from this, both methods predict the natural frequency at 25.9 Hz, which is similar to the results obtained from the pure URANS FSI simulation. Furthermore, it can be seen that the higher modes f_2 and f_4 are correctly predicted as well, which should be at $f_2 = 5.40\,f_0$ and $f_4 = 13.34\,f_0$ [130]. The odd-numbered modes do not appear in the amplitude spectrum, as the data is taken exactly at the centre of the beam. For odd-numbered modes, the centre of the beam is exactly at a node, meaning that these modes can not be captured.

In order to quantitatively compare the different methods, the root-mean-squared displacements are calculated. These are calculated over the full 8 seconds of simulation time. In order to assess how the root-mean-squared displacements vary in time, its standard deviation is calculated during the last 20 flow-through times of simulation time. From this, an uncertainty range is given that encloses a confidence interval of 95%.

It was found that the simulation with the cubic-root volume cut-off method gave an RMS amplitude of

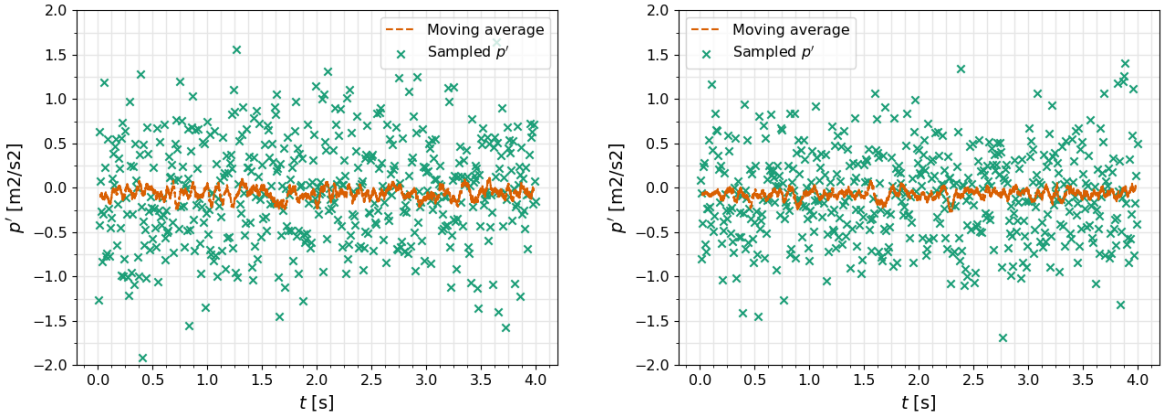

(a) Cubic-root-volume cut-off method.

(b) Cut-off method from Shur et al. [9]

Figure 7.9: The sampled specific pressure fluctuations at mid-beam for the FSI simulations with different cut-off methods, for the initial 4 seconds. The orange line indicates the moving average.

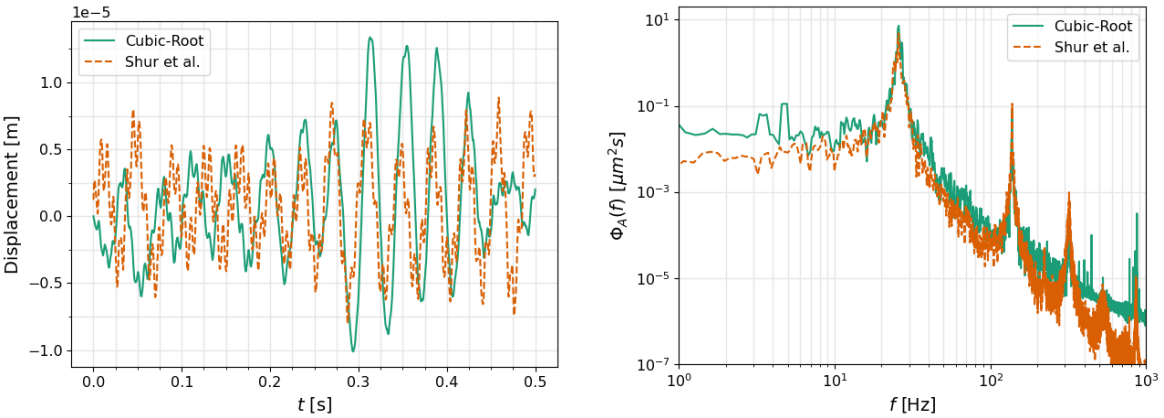

(a) Displacement in y-direction for 0.5s of simulation time.

(b) Amplitude spectrum from the full 8s of simulation time.

Figure 7.10: The amplitude in the temporal and frequency domain, for different cut-off length definitions.

$1.09e-5$ $[m]$ ±7.98%, whereas the simulation with the cut-off method taken by Shur et al. gave an RMS amplitude of $7.80e-6$ $[m]$ ±6.42%. Interestingly, there is indeed a difference between the two methods. In this particular case, the difference might be this big due to the extreme difference between the fineness of the mesh in the wall-normal and streamwise directions. The cut-off filter of Shur et al. is not very influenced by this, as it bases the cut-off length on the maximum of the characteristic cell lengths. The cubic-root volume method is very sensitive to the wall normal direction, which causes this large discrepancy. From these results, it seems that the cubic-root volume method overpredicts the amount of energy that can actually be resolved by the mesh, and thus in turn overpredicts the root-mean-square pressure fluctuations as well as the amplitude. From this point on, the cut-off filter of Shur et al. will be used for subsequent simulations. It also became clear that a very large time frame is necessary to accurately assess the RMS amplitude. For example, it was found that after 4 seconds of simulation time, the RMS amplitudes were very different, with values of $6.74e-6$ $[m]$ and $6.09e-6$ $[m]$ for the cubic-root and Shur et al.'s method, respectively. In particular, the cubic-root method shows a much larger difference, which is also reflected in the final confidence interval. This is another reason why the cut-off filter of Shur et al. seems to be more favourable than the cubic-root method.

7.5.2. Effect of Time Correlation Method

In section 6.2.7, a preliminary investigation was done on the effects of the time correlation method for the modelling of the velocity fluctuations. It was found that there were slight differences in terms of p'_{rms}, as well

as in the frequency spectra of the pressure fluctuations. In this subsection, the investigation is elaborated by comparing the different time correlation methods in fluid-structure interaction simulations.

The comparison was done again at a mean flow velocity of 10 m/s. The method of convection & exponential correlation, as well as its rescaled version were compared to the pure convection method. Interestingly, the convection & exponential correlation method showed results very close to the pure convection method. However, the rescaled method showed an overestimation compared to the other methods. For the pure convection case, the simulation gave a root-mean-square amplitude of $A_{rms} = 7.80\ \mu m$ ±6.42%. In comparison, the convection & exponential correlation method gave $A_{rms} = 7.64\ \mu m$ ±2.50% and its rescaled version simulated a root-mean-square amplitude of $A_{rms} = 9.33\ \mu m$ ±2.59%.

The difference between the C&EC and the RC&EC method is mainly due to the coarseness of the mesh that is used. In section 6.2.7, the different methods were compared with a fine mesh, as it had to be able to resolve a relatively high amount of turbulent kinetic energy of the flow. In the current case, a relatively coarser mesh is used. In this situation, the rescaling method is not effective. This is due to the fact that the velocity fluctuations are rescaled with the total lost energy, but the amount of lost energy varies over the domain. In turn, this causes a redistribution of kinetic energy along the wall-normal direction. The same phenomenon was also found in section 6.2.7, however, with a finer mesh this was less pronounced, as less diffusion occurred.

While the RC&EC method showed higher amplitudes, it was able to correctly predict the modal frequencies. This is shown in fig. 7.11, The three spectra almost overlap perfectly. The main difference can be found at the natural frequency, predicted to be at 25.9 Hz. Here, the RC&EC method shows a higher peak than both the convection & exponential correlation method, and the pure convection method.

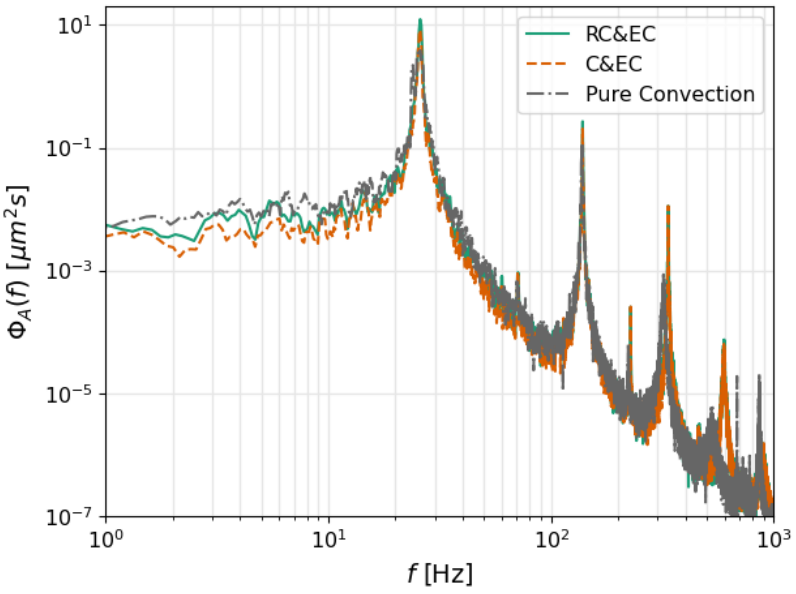

Figure 7.11: The amplitude spectra for the various time correlation methods.

From the results, it seems that the use of the C&EC method or the pure convection method have no differentiable effect on the eventual root-mean-squared amplitude. The different methods could however have an effect on the confidence intervals of the results. From section 6.2.3 it was found that the pure convection method has larger confidence intervals due to the fact that fewer random numbers are used. For the simulated channel flow, it was found that the pure convection method gave a confidence interval for the RMS pressure fluctuations of ±2.68% vs ±0.24% for the C&EC method. However, these confidence intervals are in the similar order of the confidence intervals introduced by the variation in the RMS amplitude over time. Thus, it was hypothesized that this would not have a large influence on the results.

Another element to consider is the computational resource requirements. The C&EC method needs to solve for three extra equations, as it solves the advection equation numerically, thus making it more computationally expensive. Next to this, it was found that the C&EC method had stricter Courant number restrictions, which meant that it needed a smaller timestep than the pure convection method. For this reason, the

pure convection method was used in subsequent simulations.

In fig. 7.12, the amplitude spectrum and pressure spectrum, both sampled at the inner wall mid-beam, of the simulation with the pure convection method are shown together. The pressure spectrum is very similar as the one shown in fig. 7.8. From fig. 7.12, it becomes clear that espescially the lower frequencies must be resolved accurately. From the various simulations done, it was found that the RMS amplitude consists for 97% out of the frequencies up to and including the natural frequency. Up to f_2, 99.7% of the RMS amplitude is accounted for. To resolve the lower frequencies accurately, the simulation time must be sufficiently long. From experiments, it was found that for lower Strouhal numbers ($St < 2.5$), the pressure fluctuation spectrum is relatively level [129]. Thus, next to looking at the variance in the RMS amplitude, one should also look at the pressure spectrum to determine if the simulation is converged. This is qualitatively determined by judging how "flat" the pressure fluctuation spectrum at the lower frequencies is. If there are large bumps or valleys at frequencies in the region upto f_2, the simulation is not fully converged yet, and the simulation should be run further untill these bumps and valleys flatten out.

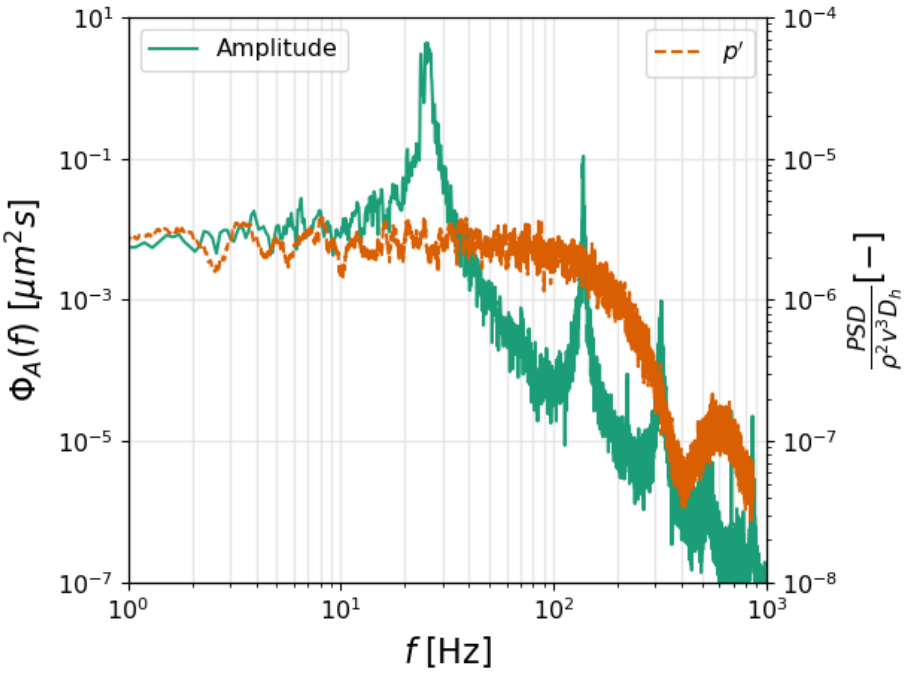

Figure 7.12: The amplitude and pressure fluctuation spectra, overlapped, for the pure convection method.

7.5.3. Effect of Mesh Size & Initial Randomness

Mesh dependency studies are a given in any study that focusses on CFD. With RANS simulations, the mesh dependency is mostly related to the discretization of the governing equations. However, with simulations done with the AniPFM, the amount of energy that is resolved also depends on the fineness of the mesh. There is no sub-grid model that models the effect of the unresolved velocity fluctuations on the pressure fluctuations. Thus, as found in section 6.2.4, the statistics of the pressure fluctuations only converge if a large part of the velocity fluctuations is resolved. However, the goal of the AniPFM is to provide a computationally less expensive method than LES that can be used for FSI simulations, thus it is not possible to resolve the bulk of the velocity fluctuations. Since the root-mean squared amplitude is the quantity of interest, this quantity is evaluated for several meshes. In addition to this, the effect of the initialization of the random numbers is evaluated by using two different seed numbers for the same mesh.

The mesh study is done on a limited amount of meshes, and the azimuthal mesh fineness is kept constant. This is done because the azimuthal direction already required a high level of fineness in order to accurately discretize the geometry of the beam. Even for the highest refinement level in the axial direction, the cell size in azimuthal direction is smaller than in the axial direction. For the axial direction, three steps are taken, with meshes of 200, 300 and 400 axial elements. For the radial direction, two meshes are used, one with $y^+ = 1.05$, and one with $y^+ = 2.08$. These meshes have 50 and 40 radial elements respectively, and they both have 200

axial elements. The reason for this is to see how close to the wall the fluid needs to be resolved. For the mesh with 300 axial elements, a second simulation is done with a different seed number for the random number generator. The time step of all simulations is limited by the Courant number set at 0.8. This gives roughly 100-200 time steps per fundamental period, depending on the axial resolution. Only for the fluid domain a mesh study is done, as for the structural domain it was already found in section 7.3 that the structural mesh was converged with 50 axial quadratic elements. The results of the mesh study are shown in fig. 7.13. The mesh size is shown on the x-axis. The error bars represent the 95% confidence interval of the RMS amplitudes over the last 20 flow-through times.

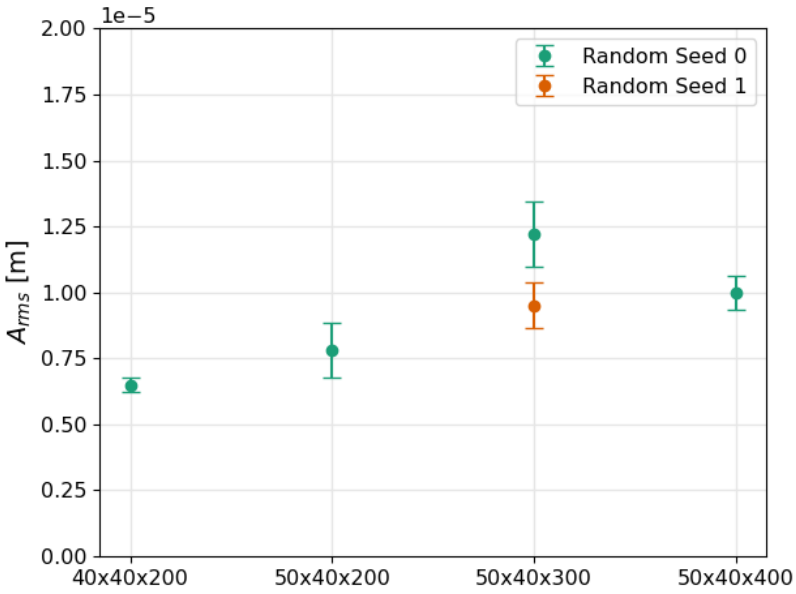

Figure 7.13: The RMS amplitudes of the coupled AniPFM FSI simulations for various meshes and random seed numbers.

The mesh with $y^+ \approx 2$ shows a considerable lower RMS amplitude than the equivalent mesh with $y^+ \approx 1$, indicating the necessity to accurately resolve the flow up to the wall with $y^+ = 1$. For the finer meshes with $y^+ \approx 1$, it can be seen that the results are in the same ballpark with several overlapping confidence intervals, but still show significant differences between the meshes. Furthermore, the simulations with the same mesh but different random numbers show a significant difference in the RMS amplitude as well. This difference is much larger than what was estimated based on the turbulent channel flow results. This suggests that although in all meshes the essential scales are resolved, there is a large uncertainty when tweaking the mesh. Note that part of this uncertainty could be due to the simulation time not being long enough. In section 7.5.1, results varied massively for a simulation time of 4 seconds versus 8 seconds. This indicates the necessity to perform simulations with a long simulated time.

7.5.4. Comparison with Experiment

The investigation into the influence of AniPFM parameters and the mesh has given confidence in the choice of set-up and the mesh size. In this section, the RMS amplitudes are compared to those of the experiment by Chen & Wambsganss, in order to investigate the accuracy of the AniPFM. Simulations were performed at 10, 15, and 20 m/s. The final set-up of the 10 m/s simulation was used for tests at 15 and 20 m/s. Note that not the same mesh is used in each simulation, but an equivalent mesh such that $y^+ = 1$ for all simulations.

The results for the various flow velocities are shown in fig. 7.14. Here, again the dots indicate the experimental values of Chen & Wambsganss, whereas the line indicates the values calculated by their analytical model. The error bars again note the 95% confidence interval over the last 20 flow-through times. The results of the simulations with different seed numbers are shown at 10 m/s. Although the effect of different seed numbers was not tested for higher velocities, the results at 10 m/s should give an indication of the uncertainty that higher flow velocities would experience as well. Note that the results of Nazari et al. [17] are not included, as they are one order of magnitude larger than all other data points.

Most of the comparison material is available at 10 m/s. Here, it can be seen that there is a wide spread

in the results of the different methods. The AniPFM shows a clear overestimation of the RMS amplitude, whereas the results of Kottapalli et al. and De Ridder show an underestimation. Note that the simulation performed by De Ridder is a pure LES simulation, not an FSI simulation. The RMS amplitude was obtained using the force frequency spectrum as input of the theoretical model of Chen & Wambsganns. The results of Kottapalli et al. are obtained with a URANS FSI methodology combined with a pressure fluctuation model, similar to the method presented in this thesis.

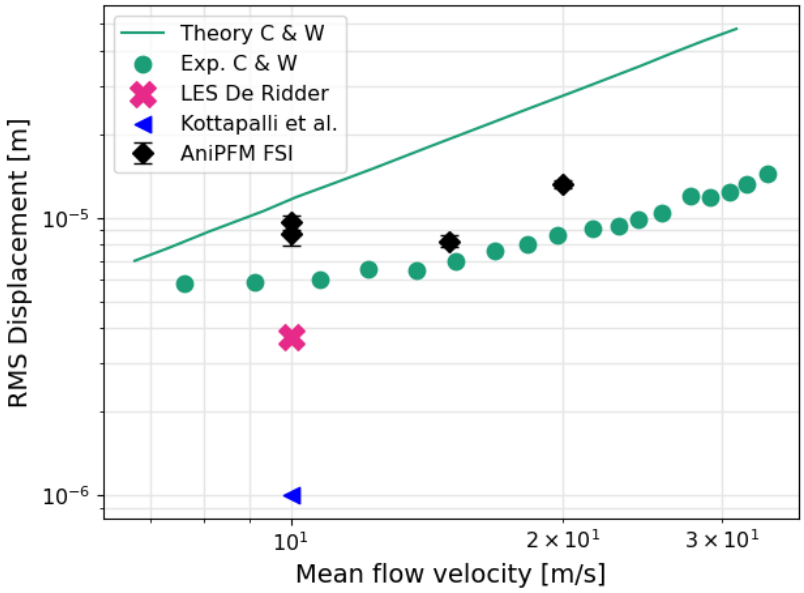

Figure 7.14: The RMS vibration amplitudes of the brass beam of the current work, compared to various simulations as well as experimental results. [14, 15, 18]

From channel flow simulations, it was expected that the AniPFM would overpredict the RMS amplitude, as the AniPFM showed an overestimation of the RMS pressure fluctuations as well, which is positively correlated with the RMS amplitude in FSI simulations. The results of Kottapalli et al. confirms this. Their proposed pressure fluctuation model showed an underestimation in the pressure fluctuations, and this is also translated to the RMS amplitude. However, in the channel flow simulation, the pressure fluctuations were not as overpredicted as the amplitudes in the FSI simulation. One possible explanation for this is that the Reynolds number of the brass beam in axial flow is an order of magnitude larger than the Reynolds number of the channel flow. It could be that the pressure fluctuations are further overestimated at higher Reynolds numbers. However, from fig. 7.8 it was found that while the AniPFM showed higher pressure fluctuations than the LES of De Ridder, the lower frequencies were in great agreement with established experimental results. From this, it seems more likely that the overestimation is partly due to the differences in modal properties of the FSI simulations versus the experiment.

While the theoretical model of Chen & Wambsganns shows a large discrepancy with the experimental results in fig. 7.14, in other performed experiments it showed good agreement at higher flow velocities. The reason for the large discrepancy in the shown experiment is that a pressure-spectrum of a beam with a different hydraulic diameter is used as input for the model. Due to its relatively good agreement with experiments given the correct input, it would be very interesting to see the predicted RMS amplitude of Chen & Wambsganns theoretical model with the input taken from the AniPFM. This would isolate the error of the AniPFM, which could then be compared to the LES results of De Ridder.

At 10 m/s, the AniPFM shows an error of 27-60% depending on the time correlation method, seed initialization and mesh size. This is a large range, and it is hypothesized that this is mainly due to the pure convection method for time correlation. This showed a larger than expected uncertainty range due to its use of a small set of random numbers. The convection & exponential correlation method should show a smaller uncertainty in this regard, as it uses new random numbers at every timestep. For this reason, it is recommended that for future use, the convection & exponential correlation method is used in FSI simulations, at the cost of higher computational requirements.

In comparison, the result obtained by De Ridder shows an error of 38.3% w.r.t. the closest experimental value. This is in the same order of magnitude as the AniPFM method, but it requires much more computational resources. Compared to the results of the PFM of Kottapalli et al., the new method also gives results closer to that of the experiment.

The AniPFM FSI simulations show similar results at higher velocities. However, the closest result w.r.t. the experiment is found at a mean flow of 15 m/s. A RMS amplitude of $8.26e-6$ μm $\pm 3.62\%$ is found, whereas the experiment gives a value of $7.0e-6$ μm. This gives an error of $18.0 \pm 3.62\%$. At a mean flow of 20 m/s, a RMS amplitude of $1.32e-5$ μm $\pm 3.24\%$ was found, the experiment showed a RMS amplitude of $8.6e-6$ μm. This level of overestimation is similar to that at 10 m/s. Note that, for these velocities, no simulations have been done to quantify the effect of different initializations for the random numbers used. For greater confidence in the results, the simulations should also be performed with C&EC as time correlation method, and/or with more wavenumber modes.

In conclusion, the use of the proposed AniPFM has shown an improvement in the prediction of the root-mean-squared amplitude, compared to the previous pressure fluctuation model proposed by Kottapalli et al. [14]. Although the AniPFM showed a similar error w.r.t. the RMS amplitude as the large-eddy simulation of De Ridder at 10 m/s, due to lack of data at other mean flow velocities, no conclusions can be made about the general accuracy of the AniPFM versus large-eddy simulations. The main drawback of the AniPFM at this moment is the discrepancy between simulations with different mesh sizes and random number initialization. This could be reduced by using the convection & exponential correlation method for time correlation. Mesh and seed sensitivity studies must be done for this time correlation method to confirm that it indeed reduces the size of the confidence interval. The AniPFM shows a better agreement with respect to the experimental values at high mean flow velocities, but other testcases must be simulated to further validate the use of the AniPFM.

7.5.5. Computational Resources

In section 6.2.8, the distribution of the computational resources was investigated for the turbulent channel flow case. While the initial results seemed promising, it was not possible to extrapolate this to FSI simulations, as the URANS calculations for the channel flow were relatively fast due to the fact that the simulation was already converged to a steady state. The fluid solver takes the last timestep as initial guess for the current timestep, thus in a steady solution, the solver will need very few iterations to converge. In FSI, the solution changes dynamically, which means that the URANS solver will likely take longer per timestep.

For this reason, the distribution of computational resources was again evaluated, but this time for the FSI simulation. This was done with a 50x40x400 mesh, with the settings of the AniPFM as discussed in section 7.2. Since the runtime is the important metric, the computational resources are evaluated by looking at the total run time of each component of the FSI simulation. Due to the use of the IQN-ILS coupling scheme, it was possible for the fluid solver and the structural solver to be coupled in parallel, i.e., both solvers were computing a timestep at the same time, instead of sequentially. Due to the domain decomposition, the fluid solver took slightly longer than the structural solver for each iteration. Since they are run in parallel, only the run time of the fluid solver is of importance, and thus the computational resources of the structural solver are not included in the comparison. The distribution of run time is shown in fig. 7.15.

As can be seen, the URANS calculations take 49.8% of the total run time, whereas the total AniPFM runtime is equal to 44.5% of the total run time. Furthermore, communication and mapping between the structural and fluid solver took roughly 5.7% of the runtime. Thus, the total runtime is roughly doubled by adding the AniPFM calculations. These results are quite different from the results in section 6.2.8, and they show a more accurate distribution of an actual FSI simulation.

Thus, to have a decrease in computational time with respect to large-eddy simulations, the mesh must be at least twice as small. This does not take into account the fact that with finer meshes, the timestep must also decrease, thus further increasing the computational time. For comparison, De Ridder [18] performed a LES of the same geometry and inlet conditions. For this, an equivalent mesh of 720 million cells was necessary, when having the same length-to-diameter ratio as the current case. With the current URANS simulations, the cell count has been kept below 1 million for even the finest simulations. Thus, it can be concluded that the AniPFM provides a computationally more efficient method than LES.

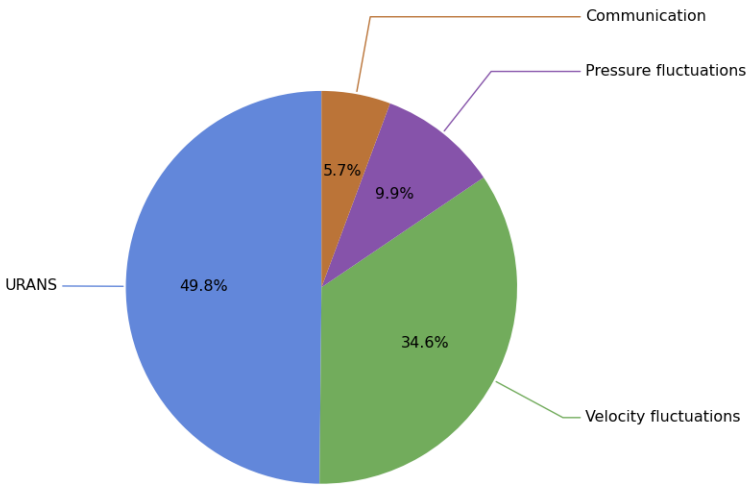

Figure 7.15: The distribution of the computational resources for an FSI case with a 50x40x400 mesh.

7.6. Summary

After the validation and verification of the AniPFM for purely CFD cases, a fluid-structure interaction case is simulated. Namely, a flexible brass beam in turbulent water. This case is from an experimental set-up of Chen & Wambsganss [15], and several authors have published simulations with the same set-up. After an initial verification of the FSI set-up, the AniPFM was used to simulate the pressure fluctuations on the brass beam. It was confirmed that the cut-off method introduced by Shur et al. showed superior results for the RMS amplitudes, compared to the cubic-root cut-off method. It was also found that the random number initialization gives a larger confidence interval for the RMS vibration amplitude than expected. This could be attributed to the time correlation method utilized in the simulations. Further research needs to be done to confirm this.

The results were compared to both previous simulations and experimental results. The AniPFM showed a great improvement compared to the previous pressure-fluctuation model of NRG. Furthermore, it showed a similar discrepancy with respect to the experiment as a previous large-eddy simulation performed by De Ridder [18], although this was not an FSI simulation. More data-points are needed to conclude the effectiveness of the AniPFM versus LES. The method showed similar results at higher mean flow velocities, which further demonstrated the validity of the AniPFM. The AniPFM roughly doubles the run-time of a typical URANS simulation, and it does require the mesh to be wall-resolved. However, compared to a full LES FSI simulation, the run-time is still greatly reduced with more than an order of magnitude, while still showing results in the same order of magnitude as the experiment.

8

Conclusion & Recommendation

In previous chapters, all relevant theory and performed numerical simulations were elaborated upon. In this chapter, the findings from the thesis are concluded, and the research objectives that were discussed in the introductory chapter are reflected upon. Next to this, recommendations are given for further research. This includes recommendations on the improvement of the AniPFM and the NRG-FSIFOAM framework, as well as recommendations on possible extra test cases to further validate the model.

8.1. Conclusion

Turbulence-Induced Vibrations (TIV) on nuclear fuel rods subjected to a coolant with axial flow have a large impact on nuclear safety and the lifetime of fuel rods. The vibrations induced by turbulence create small but significant vibration amplitudes in the case of axial flow. These vibrations in turn cause structural effects such as fatigue problems, fretting wear, and stress corrosion cracking. This gives a good motivation for studying and being able to predict the effects of TIV, and it has been studied extensively by the use of experiments, where prediction methods have been made based on semi-empirical relations. As these semi-empirical methods have not shown the desired accuracy, and it is not possible to use them for more complex configurations, using FSI simulations are a more suitable replacement. While DNS and LES can predict pressure fluctuations, these simulations are typically too expensive for industrial applications. Instead, NRG has developed a numerical framework for the simulations of flow-induced vibrations, called NRG-FSIFOAM. NRG-FSIFOAM uses a URANS approach coupled with a Pressure Fluctuation Model (PFM), to capture the effect of pressure fluctuations caused by turbulence. While this PFM showed promising initial results, it uses several assumptions that could limit its performance. In this thesis, a new pressure fluctuation model is introduced, called AniPFM, which aims to address certain assumptions of the original PFM.

The pressure fluctuations can be computed solely from the mean velocities and the velocity fluctuations, thus rather than modelling the pressure fluctuations, the velocity fluctuations are modelled. This is also known as modelling synthetic turbulence. From the Navier-Stokes equations, it was found that the synthetic turbulence eddies should be approximately convected by the local mean flow velocity. The energy spectrum must be accurately approximated, as it determines the amount of energy the different scales have, and it implicitly determines the spatial correlations between the velocity fluctuations. In order to accurately portray the energy spectrum, the Reynolds stress tensor must be replicated, as it directly influences the size and skewness of the energy spectrum. Lastly, due to the production and dissipation of turbulence, velocity fluctuations show a decorrelation in time. Thus, next to convection, this decorrelation must also be modelled. The new model that follows these principles is called the AniPFM.

Even though the old and the new pressure fluctuation model are both based on the Random Flow Generation method, the AniPFM has several differences with respect to the PFM. With the AniPFM, the velocity fluctuations are based on the individual Reynolds stresses as opposed to the turbulent kinetic energy. Furthermore, only the resolved velocity fluctuations are modelled. This especially gives a large difference in the magnitude of the pressure fluctuations, and reduces unphysical correlations between scales near the cut-off wavenumber. The method for calculating the wavenumber direction has also been adjusted, which previously was not truly isotropic. Finally, several time correlation methods are available, such as a pure convection method, as well as a method that models both the convection and the decorrelation due to production

and dissipation.

To verify and validate the AniPFM, two CFD testcases were performed. From the homogeneous isotropic turbulence case, it was found that the PFM and the AniPFM gave similar results in terms of the RMS pressure fluctuations, and the pressure spectrum. However, it was concluded that the peak of the energy spectrum is better predicted by the AniPFM, as well as the time correlation of the velocity fluctuations. Finally, with the implementation of the cut-off filter, the non-physical accumulation of energy near the wavenumber was prevented, granting a more accurate energy and pressure spectrum for the AniPFM. It was expected that both models gave similar results, as they both should be able to predict isotropic turbulence.

In the second test case, a turbulent channel flow was simulated. Here, distinct differences could be found between the two models. In particular, the root-mean-squared pressure fluctuations showed a large difference. It was found that given the correct mean flow characteristics, the AniPFM could correctly estimate the RMS pressure fluctuations with an error of -4 to 10%, depending on the modelling choices. When using the $k-\omega$ SST model with the Wilcox correction, an additional error of roughly 15% is found. This gave an total overestimation of 10% or 28%, depending on the chosen cut-off length method. With the previous PFM, the RMS pressure fluctuations were underestimated by 47%. Several aspects of the AniPFM were evaluated. It was concluded that the pressure wavenumber spectrum is accurately reconstructed from the AniPFM, with respect to DNS data. Furthermore, the pressure frequency spectrum is dependent on the chosen time correlation method, but all methods show agreeable behaviour for the lower frequencies. The finite numbers of wavenumbers also cause an uncertainty in the pressure fluctuations, but this is small in comparison to the model error and the error induced by URANS input. From these results, it can be concluded that the first research objective, shown below, was met.

> **To improve the current pressure fluctuation model, in particular the accuracy of the root-mean-squared pressure fluctuations and the pressure fluctuation wavenumber spectrum in the near wall vicinity, by using more realistic assumptions regarding (an)isotropy, the energy spectrum and time correlation.**

Finally, fluid-structure interaction simulations were done of a flexible brass beam in turbulent water. These simulations replicated the experiment of Chen & Wambsganss. First, simulations were done without the AniPFM, from this it was found that the natural frequency and damping ratio were in accordance with previously performed simulations, thus verifying the FSI set up. Simulations were done at 10, 15, and 20 m/s, where several meshes and AniPFM settings were tested at 10 m/s. It was found that the coarsest mesh of 50x40x200 resolved enough energy to be able to predict the vibrations, but it was also concluded that there is a large uncertainty in results with varying meshes and settings.

From the simulations, best practices could be established for future simulations. It was found that the cut-off length as proposed by Shur et al. [9] showed superior results to the cubic-root cut-off method, and thus this method is recommended for further use. The $k-\omega$ SST model together with the Wilcox correction showed the closest results to DNS data. For the mesh, a wall-distance of $y^+ = 1$ is recommended, the mesh in the other directions is restricted by ensuring an aspect ratio conforming to traditional CFD standards. Finally, in the performed simulations, pure convection is used as time correlation method. However, for future use, the convection & exponential correlation is recommended, as this shows a smaller uncertainty w.r.t. the initialization of the random numbers.

The use of the proposed AniPFM has shown an improvement in the prediction of the root-mean-squared amplitude, with respect to the previous pressure fluctuation model proposed by Kottapalli et al. While the AniPFM showed a similar error in the RMS amplitude as the large-eddy simulation of De Ridder at 10 m/s, due to lack of data at other mean flow velocities, no conclusions can be made about the general accuracy of the AniPFM versus large-eddy simulations. Furthermore, other testcases must be simulated to further validate the use of the AniPFM. Next to this, the use of the convection & exponential correlation function and its effect on the confidence interval must be further researched. The AniPFM showed promising results in predicting the RMS amplitudes at high mean velocities, as it showed errors of under 20% for the 15 m/s simulation, and at 20 m/s it showed a similar error as the simulations at 10 m/s. From this, it can be concluded that the second research objective, shown below, was also successfully met.

> **To improve the FSI modelling of nuclear fuel rods in axial flow using URANS, in particular the RMS amplitude and the amplitude frequency spectrum, by utilizing a more accurate pressure fluctuation model.**

8.2. Recommendations

Over the span of the thesis, many interesting directions are open to follow, but in the end only one direction can be taken. This leaves a main road with many side paths left unexplored. For this reason, some of these interesting side paths are noted here, that are worthy of exploration.

With the simulation of the flexible brass beam, several extra steps can be taken to increase the validity of the results. At the moment, only LES results were available at 10 m/s, which showed an underestimation in both LES results and AniPFM results, compared to the experiment. It would be interesting to see the difference in error of the AniPFM and LES at higher velocities. The used LES results were not actual fluid-structure interaction calculations, but rather were based on an analytical model using LES results. A full large-eddy FSI simulation would be better comparison material for the results shown in this thesis. Next to this, it would also be interesting to use the AniPFM with the same analytical model, to compare its results to that of the LES and the experiment. This would provide a more fair comparison, and it would eliminate the errors introduced by FSI coupling. Finally, it is recommended to further research the use of the convection & exponential correlation method in FSI simulations, as this could potentially reduce the uncertainty introduced by the initialization of the random numbers. This uncertainty is regarded as the largest flaw in the current method, and improving this could further improve the confidence in the obtained results.

It is also recommended to perform simulations of other cases in order to further validate the AniPFM. The cantilever beam case of Cioncolini et al. [131] would be a good candidate. It is still a simple geometry, but the structural response is quite different from a clamped-clamped beam, due to its end that is free to vibrate. From the paper, RMS displacements are available for several flow velocities. Next to this, it is recommended to perform simulations of rod bundles. The performed simulations of the clamped brass beam were ideal for the investigation of a new model, due to its simplicity. However, the eventual use case would be for rod bundles in axial flow, where the flow physics are much more complicated, due to the influence the rods have on each other. For this reason, it is essential to validate the use of the AniPFM in rod bundle flows.

The AniPFM showed close agreement with DNS and experimental data for the performed testcases, and it is recommended for future work to put the focus on the further validation of its use in FSI simulations. However, there are also several points of improvement for the AniPFM, which could be necessary if a more accurate model is necessary. The recommendations are elaborated in the subsequent paragraphs.

From the thesis it followed that the mesh requirements are dominated by the requirements of the AniPFM. This causes relatively fine meshes for URANS simulations. For the specific case of the flexible brass beam, this meant that the timestep size was dominated by maintaining stability for the fluid solver, rather than the actual physical phenomena. For reference, in the performed simulations, there are roughly 100-200 time steps per period, depending on the mesh. It would be possible to perform the URANS simulation on a coarser (perhaps wall-modelled) mesh, while the pressure fluctuations are solved on a finer wall-resolved mesh. Since the governing equation for the pressure fluctuations does not have a temporal derivative, its stability is not dependent on the timestep. This would allow for larger time steps and thus much shorter run times. Note that this would only be possible if the pure convection method is used, as the convection & exponential correlation method solves the convection equation numerically, and then the stability is dependent on the timestep.

As was seen in the performed simulations, the quality, and the refinement of the mesh is integral to getting good results with the AniPFM. Due to the simple nature of the simulated fluid domains, structured meshes could be used in all cases. The effects of using unstructured meshes has not been investigated in this thesis, but it would be interesting to see the results of the AniPFM on geometries where it is not possible to create a structured mesh.

The AniPFM, like many models, relies on simplifications and assumptions. Some of these assumptions can have a larger impact than others. One particular assumption is about the governing equation of the pressure fluctuations. The governing equation takes the velocity fluctuations as input. But in reality, only the resolved velocity fluctuations are inputted, i.e., the 'filtered' velocity fluctuations. This effect of the unresolved turbulence is not accounted for in the current AniPFM, and it was assumed to be negligible. From the current work it seems that modelling the resolved pressure fluctuations gives a good approximation in the used testcases, and it seems that the sub-grid fluctuations do not need to be modelled. However, it is recommended to more accurately establish the effects of this assumption, and if necessary to propose a sub-grid model that can take these effects into account.

Another assumption is that the energy spectrum can be modelled as isotropic, after which it is scaled and rotated such that it models the anisotropy of the input Reynolds stress tensor. A problem with this method is that this also means that the cut-off length is a scalar value. This is a crude assumption because mesh cells

near wall are typically anisotropic, as the wall-normal direction is more refined. Castro et al. [72] proposed a synthetic turbulence model based on a defined energy spectrum for each principal axis, which allows the definition of a cut-off length along those axes. It is recommended to investigate how this different method of modelling the velocity fluctuations affects the pressure fluctuations. Next to this, the length scale that contains the maximum energy is closely resembled in isotropic turbulence, but near walls the length scale is underestimated. This could be one of the factors that results in the overestimation of the RMS pressure fluctuations. It is recommended to evaluate the expression for the length scale, and adjust it such that it more closely resembles the results of DNS data.

Finally, from the channel flow simulations, it was found that a large part of the error in the RMS pressure fluctuations was attributed to the error in the URANS input, in particularly the Reynolds stresses. For the majority of the simulations, the $k-\omega$ SST model was used, together with the Wilcox correction. For future work, it is recommended to implement and use a wall-resolved (Algebraic-Explicit) Reynolds Stress model, such as the elliptic blending RSM. This model provides a more accurate representation of the Reynolds stresses, while still being able to resolve the flow up to the wall.

Bibliography

[1] Sarah Harman. Pressurized water reactors. U.S. Department of Energy, 2021.

[2] Paul Flowers, William R. Robinson, Richard Langley, and Klaus Theopold. *Chemistry*. OpenStax, 2015.

[3] Bernhard Gatzhammer. *Efficient and Flexible Partitioned Simulation of Fluid-Structure Interactions*. PhD thesis, Technische Universitat Munchen, 2014.

[4] Dante De Santis and Afaque Shams. An advanced numerical framework for the simulation of flow induced vibration for nuclear applications. *Annals of Nuclear Energy*, 130:218–231, aug 2019. doi: 10.1016/j.anucene.2019.02.049.

[5] Eric Lillberg, Kristian Angele, and Gustav Lundqvist. Tailored experiments for validation of CFD with FSI for nuclear applications. In *NURETH-16*, 2015.

[6] Chunyuan Liu. *Fluid-Structure Interaction for a Cantilever Rod in Axial Flow: An Experimental Study*. PhD thesis, University of Manchester, 2017.

[7] Nityanand Sinha. *Towards RANS Parameterization of Vertical Mixing by Langmuir Turbulence in Shallow Coastal Shelves*. PhD thesis, University of South Florida, 2013.

[8] Pierre Sagaut, Sebastien Deck, and Marc Terracol. *Multiscale and Multiresolution Approaches in Turbulence - Les, Des and Hybrid Rans/Les Methods: Applications and Guidelines (2nd Edition)*. Imperial College, May 2013. ISBN 1848169868.

[9] Michael L. Shur, Philippe R. Spalart, Michael K. Strelets, and Andrey K. Travin. Synthetic turbulence generators for RANS-LES interfaces in zonal simulations of aerodynamic and aeroacoustic problems. *Flow, Turbulence and Combustion*, 93(1):63–92, may 2014. doi: 10.1007/s10494-014-9534-8.

[10] Mattias Billson, Lars-Erik Eriksson, and Lars Davidson. Jet noise modeling using synthetic anisotropic turbulence. In *10th AIAA/CEAS Aeroacoustics Conference*. American Institute of Aeronautics and Astronautics, may 2004. doi: 10.2514/6.2004-3028.

[11] Geneviève Comte-Bellot and Stanley Corrsin. Simple eulerian time correlation of full-and narrow-band velocity signals in grid-generated, 'isotropic' turbulence. *Journal of Fluid Mechanics*, 48(2):273–337, jul 1971. doi: 10.1017/s0022112071001599.

[12] Toshiyuki Gotoh and Daigen Fukayama. Pressure spectrum in homogeneous turbulence. *Physical Review Letters*, 86(17):3775–3778, apr 2001. doi: 10.1103/physrevlett.86.3775.

[13] Hiroyuki Abe, Hiroshi Kawamura, and Yuichi Matsuo. Direct numerical simulation of a fully developed turbulent channel flow with respect to the reynolds number dependence. *Journal of Fluids Engineering*, 123(2):382–393, feb 2001. doi: 10.1115/1.1366680.

[14] S. Kottapalli, A. Shams, A.H. Zuijlen, and M.J.B.M. Pourquie. Numerical investigation of an advanced u-RANS based pressure fluctuation model to simulate non-linear vibrations of nuclear fuel rods due to turbulent parallel-flow. *Annals of Nuclear Energy*, 128:115–126, jun 2019. doi: 10.1016/j.anucene.2019.01.001.

[15] Shoei sheng Chen and Martin W. Wambsganss. Parallel-flow-induced vibration of fuel rods. *Nuclear Engineering and Design*, 18(2):253–278, feb 1972. doi: 10.1016/0029-5493(72)90144-6.

[16] Jeroen De Ridder, Joris Degroote, Katrien Van Tichelen, Paul Schuurmans, and Jan Vierendeels. Modal characteristics of a flexible cylinder in turbulent axial flow from numerical simulations. *Journal of Fluids and Structures*, 43:110–123, nov 2013. doi: 10.1016/j.jfluidstructs.2013.09.001.

[17] Tooraj Nazari, Ataollah Rabiee, and Hossein Kazeminejad. Two-way fluid-structure interaction simulation for steady-state vibration of a slender rod using URANS and LES turbulence models. *Nuclear Engineering and Technology*, 51(2):573–578, apr 2019. doi: 10.1016/j.net.2018.10.011.

[18] Jeroen de Ridder. *Computational analysis of flow-induced vibrations in fuel rod bundles of next generation nuclear reactors*. PhD thesis, 2015.

[19] WNA. World nuclear performance report 2020. Technical report, World Nuclear Association, 2020.

[20] Anil Markandya and Paul Wilkinson. Electricity generation and health. *The Lancet*, 370(9591):979–990, sep 2007. doi: 10.1016/s0140-6736(07)61253-7.

[21] Benjamin K. Sovacool, Rasmus Andersen, Steven Sorensen, Kenneth Sorensen, Victor Tienda, Arturas Vainorius, Oliver Marc Schirach, and Frans Bjørn-Thygesen. Balancing safety with sustainability: assessing the risk of accidents for modern low-carbon energy systems. *Journal of Cleaner Production*, 112:3952–3965, jan 2016. doi: 10.1016/j.jclepro.2015.07.059.

[22] M.P. Païdoussis. Real-life experiences with flow-induced vibration. *Journal of Fluids and Structures*, 22 (6-7):741–755, aug 2006. doi: 10.1016/j.jfluidstructs.2006.04.002.

[23] K. H. Luk. Boiling-water reactor internals aging degradation study. Technical report, Oak Ridge National Laboratory, 1993.

[24] D. S. Weaver, S. Ziada, M. K. Au-Yang, S. S. Chen, M. P. Paı¨doussis, and M. J. Pettigrew. Flow-induced vibrations in power and process plant components—progress and prospects. *Journal of Pressure Vessel Technology*, 122(3):339–348, apr 2000. doi: 10.1115/1.556190.

[25] R.D. Blevins. Flow-induced vibration in nuclear reactors: A review. *Progress in Nuclear Energy*, 4(1): 25–49, jan 1979. doi: 10.1016/0149-1970(79)90008-8.

[26] D. Basile, J. Fauré, and E. Ohlmer. Experimental study on the vibrations of various fuel rod models in parallel flow. *Nuclear Engineering and Design*, 7(6):517–534, jun 1968. doi: 10.1016/0029-5493(68)90102-7.

[27] H.G.D. Goyder. Flow-induced vibration in heat exchangers. *Chemical Engineering Research and Design*, 80(3):226–232, apr 2002. doi: 10.1205/026387602753581971.

[28] M. P. Paidoussis. An experimental study of vibration of flexible cylinders induced by nominally axial flow. *Nuclear Science and Engineering*, 35(1):127–138, jan 1969. doi: 10.13182/nse69-a21121.

[29] M.W. Wambsganss and S.S. Chen. Tentative design guide for calculating the vibration response of flexible cylindrical elements in axial flow. Technical report, Argonne National Lab, jan 1971.

[30] Z.G. Liu, Y. Liu, and J. Lu. Fluid–structure interaction of single flexible cylinder in axial flow. *Computers & Fluids*, 56:143–151, mar 2012. doi: 10.1016/j.compfluid.2011.12.003.

[31] Z.G. Liu, Y. Liu, and J. Lu. Numerical simulation of the fluid–structure interaction for an elastic cylinder subjected to tubular fluid flow. *Computers & Fluids*, 68:192–202, sep 2012. doi: 10.1016/j.compfluid.2012.08.010.

[32] Z.G. Liu, Y. Liu, and J. Lu. Numerical simulation of the fluid–structure interaction for two simple fuel assemblies. *Nuclear Engineering and Design*, 258:1–12, may 2013. doi: 10.1016/j.nucengdes.2013.01.029.

[33] Mark A. Christon, Roger Lu, Jozsef Bakosi, Balasubramanya T. Nadiga, Zeses Karoutas, and Markus Berndt. Large-eddy simulation, fuel rod vibration and grid-to-rod fretting in pressurized water reactors. *Journal of Computational Physics*, 322:142–161, oct 2016. doi: 10.1016/j.jcp.2016.06.042.

[34] A.M. Elmahdi. Flow induced vibration forces on a fuel rod by les cfd analysis. *International Topical Meeting on Nuclear Reactor Thermalhydraulics*, 2011.

[35] Jeroen De Ridder, Olivier Doaré, Joris Degroote, Katrien Van Tichelen, Paul Schuurmans, and Jan Vierendeels. Simulating the fluid forces and fluid-elastic instabilities of a clamped–clamped cylinder in turbulent axial flow. *Journal of Fluids and Structures*, 55:139–154, may 2015. doi: 10.1016/j.jfluidstructs.2015.03.001.

[36] S. Sharma. Numerical study of turbulence induced vibrations using synthetic fluctuation field modeling in nuclear reactor applications. Master's thesis, Delft University of Technology, 2018.

[37] M.J. Pettigrew, C.E. Taylor, N.J. Fisher, M. Yetisir, and B.A.W. Smith. Flow-induced vibration: recent findings and open questions. *Nuclear Engineering and Design*, 185(2):249–276, 1998. ISSN 0029-5493. doi: https://doi.org/10.1016/S0029-5493(98)00238-6.

[38] Thomas Richter. *Numerical Methods for Fluid-Structure Interaction Problems*. PhD thesis, Heidelberg University, 2010.

[39] D. J. Acheson. *Elementary Fluid Dynamics*. Oxford University Press, March 1990. ISBN 0198596790.

[40] Ted Belytschko. *Nonlinear finite elements for continua and structures*. Wiley, Chichester New York, 2000. ISBN 9780471987734.

[41] Joris Degroote. Partitioned simulation of fluid-structure interaction. *Archives of Computational Methods in Engineering*, 20(3):185–238, jul 2013. doi: 10.1007/s11831-013-9085-5.

[42] H. G. Weller, G. Tabor, H. Jasak, and C. Fureby. A tensorial approach to computational continuum mechanics using object-oriented techniques. *Computers in Physics*, 12(6):620, 1998. doi: 10.1063/1.168744.

[43] A. de Boer, A.H. van Zuijlen, and H. Bijl. Radial basis functions for interface interpolation and mesh deformation. In *Advanced Computational Methods in Science and Engineering*. Springer-Verlag GmbH, October 2009. ISBN 3642033431.

[44] Hans-Joachim Bungartz, Florian Lindner, Bernhard Gatzhammer, Miriam Mehl, Klaudius Scheufele, Alexander Shukaev, and Benjamin Uekermann. preCICE – a fully parallel library for multi-physics surface coupling. *Computers & Fluids*, 141:250–258, dec 2016. doi: 10.1016/j.compfluid.2016.04.003.

[45] Jeremy Chouchoulis. An advanced fluid-structure interaction software package for industrial problems in nuclear reactor applications. Master's thesis, TU eindhoven, 2018.

[46] Stefan Turek and Jaroslav Hron. Proposal for numerical benchmarking of fluid-structure interaction between an elastic object and laminar incompressible flow. In *Lecture Notes in Computational Science and Engineering*, pages 371–385. Springer Berlin Heidelberg, 2006. doi: 10.1007/3-540-34596-5_15.

[47] P. A. Davidson. *Turbulence : an introduction for scientists and engineers*. Oxford University Press, Oxford, UK New York, 2004. ISBN 9780191589850.

[48] John L. Lumley Henk Tennekes. *A first course in turbulence*. The MIT Press, Cambridge, Massachusetts, 1972. ISBN 9780262536301.

[49] A. Tsinober. *An Informal Introduction to Turbulence*. Springer Netherlands, November 2001. ISBN 1402001665.

[50] Lewis Fry Richardson and Peter Lynch. *Weather Prediction by Numerical Process*. Cambridge University Press, 1922. doi: 10.1017/cbo9780511618291.

[51] Stephen B. Pope. *Turbulent Flows*. Cambridge University Press, March 2000. ISBN 0521598869.

[52] Andrei Nikolaevich Kolmogorov. The local structure of turbulence in incompressible viscous fluid for very large reynolds numbers. *Proceedings of the Royal Society of London. Series A: Mathematical and Physical Sciences*, 434(1890):9–13, jul 1941. doi: 10.1098/rspa.1991.0075.

[53] S. J. Hulshof. Cfd ii part 2:computation and modelling of turbulence. TU Delft, 2015.

[54] Andrei Nikolaevich Kolmogorov. Dissipation of energy in the locally isotropic turbulence. *Proceedings of the Royal Society of London. Series A: Mathematical and Physical Sciences*, 434(1890):15–17, jul 1941. doi: 10.1098/rspa.1991.0076.

[55] Robert D. Moser, John Kim, and Nagi N. Mansour. Direct numerical simulation of turbulent channel flow up to re_τ=590. *Physics of Fluids*, 11(4):943–945, apr 1999. doi: 10.1063/1.869966.

[56] Joel H. Ferziger, Milovan Peric, Robert L. Street, and Milovan Peri'. *Computational Methods for Fluid Dynamics*. Springer International Publishing, August 2019. ISBN 3319996916.

[57] David Wilcox. *Turbulence modeling for CFD*. DCW Industries, Inc, La Canada, CA, 1993. ISBN 9780963605108.

[58] W.P Jones and B.E Launder. The prediction of laminarization with a two-equation model of turbulence. *International Journal of Heat and Mass Transfer*, 15(2):301–314, feb 1972. doi: 10.1016/0017-9310(72)90076-2.

[59] David C. Wilcox. Reassessment of the scale-determining equation for advanced turbulence models. *AIAA Journal*, 26(11):1299–1310, nov 1988. doi: 10.2514/3.10041.

[60] F. Menter. Zonal two equation k-w turbulence models for aerodynamic flows. In *23rd Fluid Dynamics, Plasmadynamics, and Lasers Conference*. American Institute of Aeronautics and Astronautics, jul 1993. doi: 10.2514/6.1993-2906.

[61] T.J. Craft, B.E. Launder, and K. Suga. Development and application of a cubic eddy-viscosity model of turbulence. *International Journal of Heat and Fluid Flow*, 17(2):108–115, apr 1996. doi: 10.1016/0142-727x(95)00079-6.

[62] Y. Hassan. An overview of computational fluid dynamics and nuclear applications. In *Thermal-Hydraulics of Water Cooled Nuclear Reactors*. Woodhead Publishing, 2017.

[63] Farzad Bazdidi-Tehrani, Akbar Mohammadi-Ahmar, Mohsen Kiamansouri, and Mohammad Jadidi. Investigation of various non-linear eddy viscosity turbulence models for simulating flow and pollutant dispersion on and around a cubical model building. *Building Simulation*, 8(2):149–166, oct 2014. doi: 10.1007/s12273-014-0199-y.

[64] Bart J. Daly and Francis H. Harlow. Transport equations in turbulence. *The Physics of Fluids*, 13(11):2634–2649, 1970. doi: 10.1063/1.1692845.

[65] B. E. Launder, G. J. Reece, and W. Rodi. Progress in the development of a reynolds-stress turbulence closure. *Journal of Fluid Mechanics*, 68(3):537–566, apr 1975. doi: 10.1017/s0022112075001814.

[66] Charles G. Speziale, Sutanu Sarkar, and Thomas B. Gatski. Modelling the pressure–strain correlation of turbulence: an invariant dynamical systems approach. *Journal of Fluid Mechanics*, 227:245–272, jun 1991. doi: 10.1017/s0022112091000101.

[67] D. Wilcox and M. W. Rubesin. Progress in turbulence modeling for complex flow fields including effects of compressibility. 1980.

[68] Stefan Wallin and Arne V. Johansson. An explicit algebraic reynolds stress model for incompressible and compressible turbulent flows. *Journal of Fluid Mechanics*, 403:89–132, jan 2000. doi: 10.1017/s0022112099007004.

[69] Y. Egorov F. R. Menter, A. V. Garbaruk. Explicit algebraic reynolds stress models for anisotropic wall-bounded flows. *Progress in Flight Physics*, 2012.

[70] Robert H. Kraichnan. Pressure fluctuations in turbulent flow over a flat plate. *The Journal of the Acoustical Society of America*, 28(3):378–390, may 1956. doi: 10.1121/1.1908336.

[71] Chenhui Geng, Guowei He, Yinshan Wang, Chunxiao Xu, Adrián Lozano-Durán, and James M. Wallace. Taylor's hypothesis in turbulent channel flow considered using a transport equation analysis. *Physics of Fluids*, 27(2):025111, feb 2015. doi: 10.1063/1.4908070.

[72] Hugo G. Castro and Rodrigo R. Paz. A time and space correlated turbulence synthesis method for large eddy simulations. *Journal of Computational Physics*, 235:742–763, feb 2013. doi: 10.1016/j.jcp.2012.10.035.

[73] Romain Laraufie and Sébastien Deck. Assessment of reynolds stresses tensor reconstruction methods for synthetic turbulent inflow conditions. application to hybrid RANS/LES methods. *International Journal of Heat and Fluid Flow*, 42:68–78, aug 2013. doi: 10.1016/j.ijheatfluidflow.2013.04.007.

[74] Gary J. Kunkel and Ivan Marusic. Study of the near-wall-turbulent region of the high-reynolds-number boundary layer using an atmospheric flow. *Journal of Fluid Mechanics*, 548(-1):375, feb 2006. doi: 10.1017/s0022112005007780.

[75] A. Smirnov, S. Shi, and I. Celik. Random flow generation technique for large eddy simulations and particle-dynamics modeling. *Journal of Fluids Engineering*, 123(2):359–371, feb 2001. doi: 10.1115/1.1369598.

[76] L. di Mare, M. Klein, W. P. Jones, and J. Janicka. Synthetic turbulence inflow conditions for large-eddy simulation. *Physics of Fluids*, 18(2):025107, feb 2006. doi: 10.1063/1.2130744.

[77] N. Jarrin, S. Benhamadouche, D. Laurence, and R. Prosser. A synthetic-eddy-method for generating inflow conditions for large-eddy simulations. *International Journal of Heat and Fluid Flow*, 27(4):585–593, aug 2006. doi: 10.1016/j.ijheatfluidflow.2006.02.006.

[78] A.M. Kempf, S. Wysocki, and M. Pettit. An efficient, parallel low-storage implementation of klein's turbulence generator for LES and DNS. *Computers & Fluids*, 60:58–60, may 2012. doi: 10.1016/j.compfluid.2012.02.027.

[79] R. Poletto, T. Craft, and A. Revell. A new divergence free synthetic eddy method for the reproduction of inlet flow conditions for LES. *Flow, Turbulence and Combustion*, 91(3):519–539, jul 2013. doi: 10.1007/s10494-013-9488-2.

[80] Yusik Kim, Ian P. Castro, and Zheng-Tong Xie. Divergence-free turbulence inflow conditions for large-eddy simulations with incompressible flow solvers. *Computers & Fluids*, 84:56–68, sep 2013. doi: 10.1016/j.compfluid.2013.06.001.

[81] Torsten Auerswald, Axel Probst, and Jens Bange. An anisotropic synthetic turbulence method for large-eddy simulation. *International Journal of Heat and Fluid Flow*, 62:407–422, dec 2016. doi: 10.1016/j.ijheatfluidflow.2016.09.002.

[82] Mattias Billson, Lars-Erik Eriksson, Lars Davidson, and Peter Jordan. Modeling of synthesized anisotropic turbulence and its sound emission. In *10th AIAA/CEAS Aeroacoustics Conference*. American Institute of Aeronautics and Astronautics, may 2004. doi: 10.2514/6.2004-2857.

[83] Christophe Bailly and Daniel Juve. A stochastic approach to compute subsonic noise using linearized euler' s equations. In *5th AIAA/CEAS Aeroacoustics Conference and Exhibit*. American Institute of Aeronautics and Astronautics, may 1999. doi: 10.2514/6.1999-1872.

[84] Walid Bechara, Christophe Bailly, Philippe Lafon, and Sebastien M. Candel. Stochastic approach to noise modeling for free turbulent flows. *AIAA Journal*, 32(3):455–463, mar 1994. doi: 10.2514/3.12008.

[85] R. Ewert, J. Dierke, J. Siebert, A. Neifeld, C. Appel, M. Siefert, and O. Kornow. CAA broadband noise prediction for aeroacoustic design. *Journal of Sound and Vibration*, 330(17):4139–4160, aug 2011. doi: 10.1016/j.jsv.2011.04.014.

[86] Fernando Gea Aguilera, James R. Gill, Xin Zhang, Xiaoxian Chen, and Thomas Node-Langlois. Leading edge noise predictions using anisotropic synthetic turbulence. In *22nd AIAA/CEAS Aeroacoustics Conference*. American Institute of Aeronautics and Astronautics, may 2016. doi: 10.2514/6.2016-2840.

[87] Paul Batten, Uriel Goldberg, and Sukumar Chakravarthy. Interfacing statistical turbulence closures with large-eddy simulation. *AIAA Journal*, 42(3):485–492, mar 2004. doi: 10.2514/1.3496.

[88] L. Davidson and M. Billson. Hybrid LES-RANS using synthesized turbulent fluctuations for forcing in the interface region. *International Journal of Heat and Fluid Flow*, 27(6):1028–1042, dec 2006. doi: 10.1016/j.ijheatfluidflow.2006.02.025.

[89] Lars Davidson and Shia-Hui Peng. Embedded large-eddy simulation using the partially averaged navier–stokes model. *AIAA Journal*, 51(5):1066–1079, may 2013. doi: 10.2514/1.j051864.

[90] N. Jarrin, R. Prosser, J.-C. Uribe, S. Benhamadouche, and D. Laurence. Reconstruction of turbulent fluctuations for hybrid RANS/LES simulations using a synthetic-eddy method. *International Journal of Heat and Fluid Flow*, 30(3):435–442, jun 2009. doi: 10.1016/j.ijheatfluidflow.2009.02.016.

[91] Dmitry Adamian and Andrey Travin. An efficient generator of synthetic turbulence at RANS–LES interface in embedded LES of wall-bounded and free shear flows. In *Computational Fluid Dynamics 2010*, pages 739–744. Springer Berlin Heidelberg, 2011. doi: 10.1007/978-3-642-17884-9_94.

[92] S. Senthooran, Dong-Dae Lee, and S. Parameswaran. A computational model to calculate the flow-induced pressure fluctuations on buildings. *Journal of Wind Engineering and Industrial Aerodynamics*, 92(13):1131–1145, nov 2004. doi: 10.1016/j.jweia.2004.07.002.

[93] Jürgen Schmiegel, Jochen Cleve, Hans C. Eggers, Bruce R. Pearson, and Martin Greiner. Stochastic energy-cascade model for (1+1)-dimensional fully developed turbulence. *Physics Letters A*, 320(4):247–253, jan 2004. doi: 10.1016/j.physleta.2003.11.025.

[94] D. Kleinhans, R. Friedrich, A. P. Schaffarczyk, and J. Peinke. Synthetic turbulence models for wind turbine applications. In *Springer Proceedings in Physics*, pages 111–114. Springer Berlin Heidelberg, 2009. doi: 10.1007/978-3-642-02225-8_26.

[95] T. Kitagawa and T. Nomura. A wavelet-based method to generate artificial wind fluctuation data. *Journal of Wind Engineering and Industrial Aerodynamics*, 91(7):943–964, jun 2003. doi: 10.1016/s0167-6105(03)00037-0.

[96] G.R. Tabor and M.H. Baba-Ahmadi. Inlet conditions for large eddy simulation: A review. *Computers & Fluids*, 39(4):553–567, apr 2010. doi: 10.1016/j.compfluid.2009.10.007.

[97] Xiaohua Wu. Inflow turbulence generation methods. *Annual Review of Fluid Mechanics*, 49(1):23–49, jan 2017. doi: 10.1146/annurev-fluid-010816-060322.

[98] Pierre Sagaut. *Large Eddy Simulation for Incompressible Flows*. Springer-Verlag GmbH, September 2005. ISBN 3540263446.

[99] Adrian Sescu and Ray Hixon. Generation of divergence-free synthetic turbulent velocity fields for LES/CAA applications. In *50th AIAA Aerospace Sciences Meeting including the New Horizons Forum and Aerospace Exposition*. American Institute of Aeronautics and Astronautics, jan 2012. doi: 10.2514/6.2012-466.

[100] S. Senthooran. *A Computational Model to Calculate the Flow-induced Pressure Fluctuations on a Bluff Body*. PhD thesis, Texas Tech University, 2002.

[101] Tony Saad, Derek Cline, Rob Stoll, and James C. Sutherland. Scalable tools for generating synthetic isotropic turbulence with arbitrary spectra. *AIAA Journal*, 55(1):327–331, jan 2017. doi: 10.2514/1.j055230.

[102] Nout van den Bos. Validation study of pressure fluctuation modelling for nuclear reactor applications. 2021.

[103] Robert H. Kraichnan. Diffusion by a random velocity field. *Physics of Fluids*, 13(1):22, 1970. doi: 10.1063/1.1692799.

[104] Fluent Inc. Fluent 12 user's guide, 2010.

[105] S.H. Huang, Q.S. Li, and J.R. Wu. A general inflow turbulence generator for large eddy simulation. *Journal of Wind Engineering and Industrial Aerodynamics*, 98(10-11):600–617, oct 2010. doi: 10.1016/j.jweia.2010.06.002.

[106] Ugo Piomelli, Jean-Louis Balint, and James M. Wallace. On the validity of taylor's hypothesis for wall-bounded flows. *Physics of Fluids A: Fluid Dynamics*, 1(3):609–611, mar 1989. doi: 10.1063/1.857432.

[107] Philippe R. Spalart, Kirill V. Belyaev, Andrey V. Garbaruk, Mikhail L. Shur, Mikhail Kh. Strelets, and Andrey K. Travin. Large-eddy and direct numerical simulations of the bachalo-johnson flow with shock-induced separation. *Flow, Turbulence and Combustion*, 99(3-4):865–885, jul 2017. doi: 10.1007/s10494-017-9832-z.

[108] James R. Wright, Riccardo Balin, John W. Patterson, John A. Evans, and Kenneth E. Jansen. Direct numerical simulation of a turbulent boundary layer on a flat plate using synthetic turbulence generation. October 2020.

[109] M. Klein, A. Sadiki, and J. Janicka. A digital filter based generation of inflow data for spatially developing direct numerical or large eddy simulations. *Journal of Computational Physics*, 186(2):652–665, apr 2003. doi: 10.1016/s0021-9991(03)00090-1.

[110] M. Fathali, M. Klein, T. Broeckhoven, C. Lacor, and M. Baelmans. Generation of turbulent inflow and initial conditions based on multi-correlated random fields. *International Journal for Numerical Methods in Fluids*, 57(1):93–117, 2008. doi: 10.1002/fld.1627.

[111] Zheng-Tong Xie and Ian P. Castro. Efficient generation of inflow conditions for large eddy simulation of street-scale flows. *Flow, Turbulence and Combustion*, 81(3):449–470, apr 2008. doi: 10.1007/s10494-008-9151-5.

[112] Dirk Dietzel, Danny Messig, Federico Piscaglia, Andrea Montorfano, Gregor Olenik, Oliver T. Stein, Andreas Kronenburg, Angelo Onorati, and Christian Hasse. Evaluation of scale resolving turbulence generation methods for large eddy simulation of turbulent flows. *Computers & Fluids*, 93:116–128, apr 2014. doi: 10.1016/j.compfluid.2014.01.013.

[113] R.I. Issa. Solution of the implicitly discretised fluid flow equations by operator-splitting. *Journal of Computational Physics*, 1986.

[114] Roland Ewert. RPM - the fast random particle-mesh method to realize unsteady turbulent sound sources and velocity fields for CAA applications. In *13th AIAA/CEAS Aeroacoustics Conference (28th AIAA Aeroacoustics Conference)*. American Institute of Aeronautics and Astronautics, may 2007. doi: 10.2514/6.2007-3506.

[115] Malte Siefert and Roland Ewert. Sweeping sound generation in jets realized with a random particle-mesh method. In *15th AIAA/CEAS Aeroacoustics Conference (30th AIAA Aeroacoustics Conference)*. American Institute of Aeronautics and Astronautics, may 2009. doi: 10.2514/6.2009-3369.

[116] A. Wohlbrandt, N. Hu, S. Guérin, and R. Ewert. Analytical reconstruction of isotropic turbulence spectra based on the gaussian transform. *Computers & Fluids*, 132:46–50, jun 2016. doi: 10.1016/j.compfluid.2016.03.023.

[117] Nan Hu, Nils Reiche, and Roland Ewert. Simulation of turbulent boundary layer wall pressure fluctuations via poisson equation and synthetic turbulence. *Journal of Fluid Mechanics*, 826:421–454, aug 2017. doi: 10.1017/jfm.2017.448.

[118] Nan Hu, Christina Appel, Stefan Haxter, Sören Callsen, and Alexander Klabes. Simulation of wall pressure fluctuations on airbus-a320 fuselage in cruise flight condition. In *25th AIAA/CEAS Aeroacoustics Conference*. American Institute of Aeronautics and Astronautics, may 2019. doi: 10.2514/6.2019-2728.

[119] Jae Wook Kim and Sina Haeri. An advanced synthetic eddy method for the computation of aerofoil–turbulence interaction noise. *Journal of Computational Physics*, 287:1–17, apr 2015. doi: 10.1016/j.jcp.2015.01.039.

[120] Yuma Fukushima. Efficient jet noise prediction using synthetic eddy method and block-structured cartesian mesh. In *29th International council of aeronautical sciences*. Unpublished, 2014. doi: 10.13140/2.1.2679.4243.

[121] Shiku Hirai, Yuma Fukushima, Shigeru Obayashi, Takashi Misaka, Daisuke Sasaki, Yuya Ohmichi, Masashi Kanamori, and Takashi Takahashi. Influence of turbulence statistics on stochastic jet-noise prediction with synthetic eddy method. *Journal of Aircraft*, 56(6):2342–2356, nov 2019. doi: 10.2514/1.c035465.

[122] Michael Goody. Empirical spectral model of surface pressure fluctuations. *AIAA Journal*, 42(9):1788–1794, sep 2004. doi: 10.2514/1.9433.

[123] Yannick Rozenberg, Gilles Robert, and Stéphane Moreau. Wall-pressure spectral model including the adverse pressure gradient effects. *AIAA Journal*, 50(10):2168–2179, oct 2012. doi: 10.2514/1.j051500.

[124] Seongkyu Lee. Empirical wall-pressure spectral modeling for zero and adverse pressure gradient flows. *AIAA Journal*, 56(5):1818–1829, may 2018. doi: 10.2514/1.j056528.

[125] J. O. Hinze. *Turbulence*. McGraw-Hill, New York, 1975. ISBN 9780070290372.

[126] A. Hellsten. New two-equation turbulence model for aerodynamics applications. 2004.

[127] Z. W. Hu, C. L. Morfey, and N. D. Sandham. Wall pressure and shear stress spectra from direct simulations of channel flow. *AIAA Journal*, 44(7):1541–1549, jul 2006. doi: 10.2514/1.17638.

[128] Timothy A. Brungart, Gerald C. Lauchle, Steven Deutsch, and Eric T. Riggs. Outer-flow effects on turbulent boundary layer wall pressure fluctuations. *The Journal of the Acoustical Society of America*, 105(4):2097–2106, apr 1999. doi: 10.1121/1.426815.

[129] R. J. Wilson and B. G. Jones. Turbulent Pressure-Velocity Measurements in a Fully Developed Concentric Annular Air Flow. *Journal of Vibration, Acoustics, Stress, and Reliability in Design*, 105(3):345–354, 07 1983. ISSN 0739-3717. doi: 10.1115/1.3269112. URL https://doi.org/10.1115/1.3269112.

[130] John A. Cafeo, Martin W. Trethewey, and III Sommer, H. Joseph. Beam Element Structural Dynamics Modification Using Experimental Modal Rotational Data. *Journal of Vibration and Acoustics*, 117(3A):265–271, 07 1995. ISSN 1048-9002. doi: 10.1115/1.2874446. URL https://doi.org/10.1115/1.2874446.

[131] Andrea Cioncolini, Jorge Silva-Leon, Dennis Cooper, Mark Kenneth Quinn, and Hector Iacovides. Axial-flow-induced vibration experiments on cantilevered rods for nuclear reactor applications. *Nuclear Engineering and Design*, 338:102–118, nov 2018. doi: 10.1016/j.nucengdes.2018.08.010.

A

Additional Simulation Results

A.1. Turbulent Channel Flow

In fig. A.1 and fig. A.2, the input energy spectra near and away from the wall are shown, for two methods of determining the eddy length scale l_e. As can be seen in fig. A.1a and fig. A.2a, near the wall, both methods massively overestimate the eddy wavenumber k_e, which is the wavenumber containing the highest turbulent kinetic energy. This is due to the fact that the input spectrum is based on the assumption that the turbulence is isotropic, whereas the turbulence near the wall is highly anisotropic. This signifies one of the areas in which the AniPFM can be improved. Looking at $y^+ = 300$, where the turbulence is more isotropic, it can be seen that in fig. A.1b, the spectrum is greatly approximated. In fig. A.2b, the eddy wavenumber k_e is overestimated. For this reason, the definition of eq. (5.8) is used for the eddy length scale.

Since k_e does not seem to vary significantly from $y^+ = 10$ to $y^+ = 300$, it would be possible to implement l_e such that it is constant, and equal to the eddy length scale in the bulk of the flow. However, this observation is made with only two datapoints, and only for this particular geometry. It would first have to be investigated if this statement holds along the wall-normal direction, if it holds for higher Reynolds numbers, and if it holds for different geometries as well. For this reason, no such change has been implemented so far. However, this highlights a possible direction to take if one wants to improve the definition of the eddy length scale.

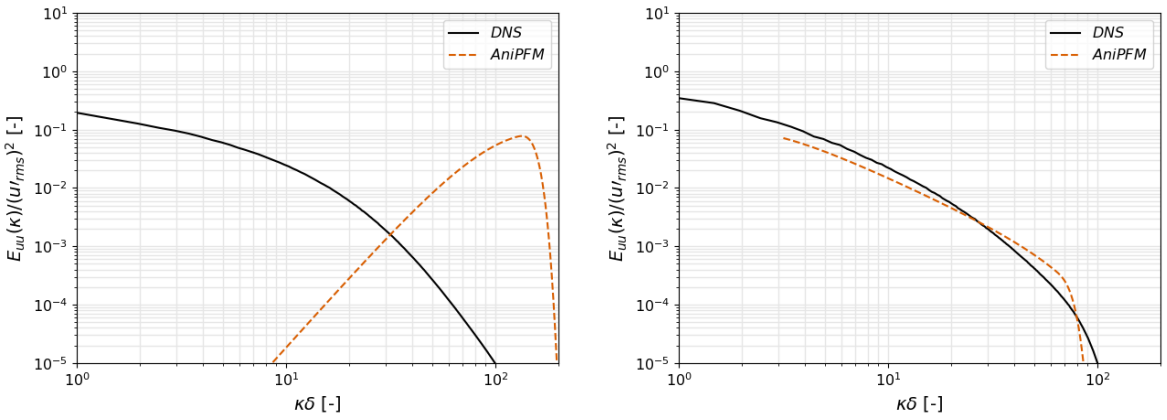

(a) $y^+ = 10$.

(b) $y^+ = 300$.

Figure A.1: The energy wavenumber spectrum with eq. (5.8) defining l_e, at different y^+ positions.

In fig. A.3, the output energy wavenumber spectra for the different options of l_e are shown at $y^+ = 10$. In both methods, the spectrum shows a roughly straight line over the resolved wavenumbers. This is due to the fact that the wavenumber with maximum energy is highly overestimated by both methods, causing a roughly constant energy distributed over the resolved scales. From the DNS results, l_e at the wall does not change significantly from l_e at mid-channel. This shows that both methods for estimating l_e do not work accurately in anisotropic turbulence, and thus it shows a point of improvement for the AniPFM.

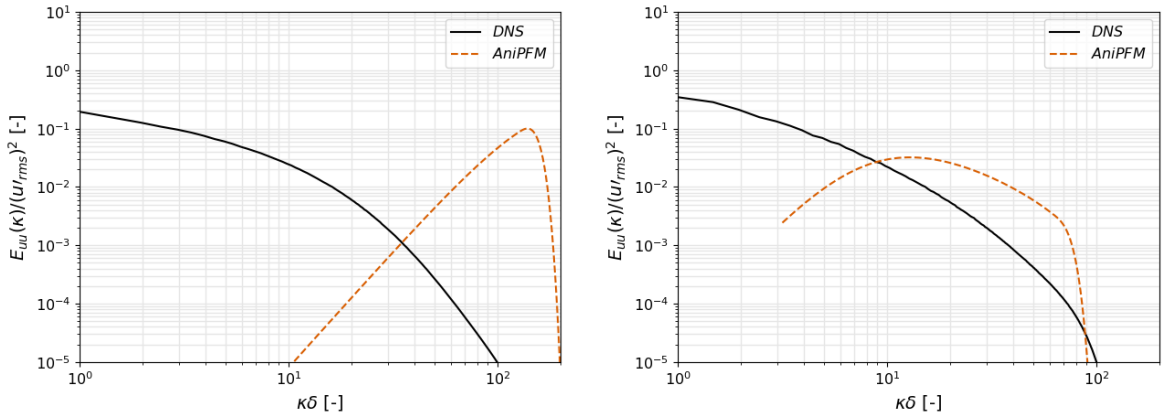

(a) $y^+ = 10$. (b) $y^+ = 300$.

Figure A.2: The energy wavenumber spectrum with eq. (4.41) defining l_e, at different y^+ positions.

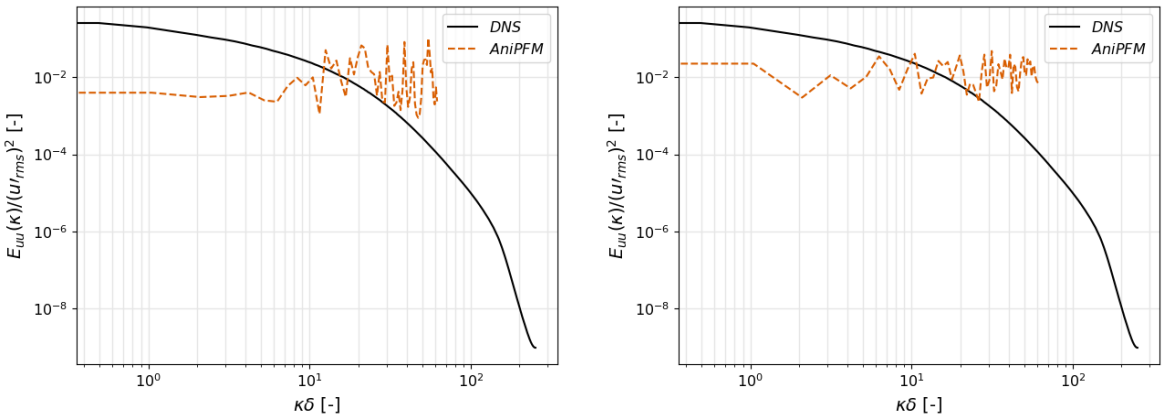

(a) l_e as defined in eq. (5.8) (b) l_e as defined in eq. (4.41).

Figure A.3: The energy wavenumber spectrum with different definitions for l_e, at $y^+ = 10$.

A.2. Flexible Brass Beam in Turbulent Water

In table A.1 through table A.4, the results of the various sensitivity studies are shown for the URANS FSI simulations of the brass beam case. Both the meshes of the structural and fluid domains are investigated, as well as the effect of the timestep. For all studies, it can be seen that the error reduces both in the natural frequency as well as in the damping ratio as the mesh/timestep is refined. Furthermore, for all studies, the second finest simulation is within 0.5% of the finest solution. With these small error margins, the set-up used in section 7.3 can be considered independent of the mesh and timestep.

Table A.1: Mesh study in axial direction for structural domain. Errors are taken w.r.t. the finest mesh

Axial Elements	**Error in f [%]**	**Error in ζ [%]**
50	0.20	0.08
75	0.031	0.11
100	0	0

Table A.2: Cross-sectional Mesh study for structural domain. Errors are taken w.r.t. the finest mesh

Cross-section Elements	**Error in f [%]**	**Error in ζ [%]**
16	-0.69	1.17
25	-0.29	0.43
36	0	0

Table A.3: Mesh study for fluid domain. Errors are taken w.r.t. the finest mesh. WM denotes wall-modelled, WR denotes wall-resolved.

Mesh	**Error in f [%]**	**Error in ζ [%]**
20x40x100 (WM)	0.058	1.33
50x40x400 (WR)	-0.21	0.42
50x40x800 (WR)	0	0

Table A.4: Study on effect of timestep. Errors are taken w.r.t. the finest timestep.

Timestep [s]	**Error in f [%]**	**Error in ζ [%]**
0.002	-1.250	-3.78
0.001	-0.626	-0.216
0.0005	-0.11	-0.437
0.0002	0	0